12-2013

Analysis of Waveguides Filled with Uniaxial Media and Metamaterials for Filter Applications using the Mode Matching Method

Luke Murphy

Abstract

This dissertation will explore the analysis of waveguide discontinuities for the purpose of dielectric filled waveguide filter analysis and design. The filling media studied are uniaxial media and uniaxial media embedded with metamaterial. A literary search provides numerous methods and numerical techniques for analyzing waveguide class problems, but ultimately the Mode Matching Method (MMM) is chosen as the numerical analysis technique for this dissertation.

An overview of waveguide theory and its application to the Mode Matching Method are presented. The Mode Matching Method is then used to analyze simple cases to confirm the numerical accuracy. Once accuracy is confirmed, Mode Matching theory is applied assuming the waveguides are filled with anisotropic medium. This theory is extended to uniaxial media with special orientations of the optic axis, because in practice the coordinate systems of media and waveguide do not always coincide. The Mode Matching Method with rotated optic axis is also extended to include the losses of the dielectric. This thesis also goes on to demonstrate the Mode Matching Method can accurately analyze dielectric waveguides with embedded metamaterial, specifically thin wire metamaterials

Finally two dielectric filled waveguide filters are designed using the Mode Matching Method: one filter with embedded metamaterials and one filter without metamaterials. The filters are then manufactured. The measured results are compared to the Mode Matching results and shown to have excellent agreement.

Analysis of Waveguides Filled with Uniaxial Media and Metamaterials for Filter Application using the Mode Matching Method

By

Luke Edward Murphy

B.S. Rensselaer Polytechnic Institute, 2007

M.S. Syracuse University, 2009

Dissertation

Submitted in partial fulfillment of the requirements for the degree of

Doctor of Philosophy in Electrical and Computer Engineering

Syracuse University

December 2013

Acknowledgments Page

First and Foremost, I would like to thank my advisor Dr. Ercument Arvas. At a time when I felt like I would never finish my PhD he believed in me and always provided the support I needed. He has been a great teacher in the field of microwave engineering, and provided advice regarding my professional career when needed. I hope one day to be the mentor to young scientists and engineers that he was to me. I will be forever indebuted to him.

I would also like to thank Dr. Joseph Mautz for being my co-advisor and reader. He took the time to meet with me every week, and provided valuable input in the revision process. Without Dr. Mautz I doubt my thesis would have been completed with such quality in such a timely fashion. Our weekly discussions constantly taught me how to be a better engineering student.

I would like to thank the members of my defense committee for taking time out of their day and participating. Specifically, Dr. Riyad Aboutaha for being the committee chair, Dr. Jay Lee, Dr. Qi Wang Song, and Dr. Donald Nicholson.

Lastly, I would like to thank my family and friends for always being there for me. They allowed me to vent when needed, and gave me support to continue at rough times. I would specifically like to thank my Mother Sue, Father Matt, Stepmother Mary, and my brother Zach for always standing behind me and providing support. I also want to thank my close friend Mohsen Yazdani who always had time for me to bounce ideas off his head, and let me think out loud in our office.

Contents

Table of Figures

1 Introduction

1.1 Goals of Research

This research is intended to provide analysis of the propagation of waves inside waveguides with an end application of designing waveguide filters that take advantage of filling media properties. The author's hope is that this thesis will provide insight for engineers designing waveguide filters or provide a starting point for a future student's thesis work.

This work investigates various analytical methods to solve waveguide problems, such as mode-matching, various integral methods, finite element methods (FEM), and various hybrid methods. The mode-matching method (MMM) is chosen and analyzed. This research also investigates wave propagation in a waveguide filled with an arbitrarily oriented anisotropic uniaxial media, and how the orientation effects propagation. Once a method is derived for the analysis of wave propagation in media filled waveguides this knowledge will be applied to waveguide filter design, because a high percentage of man-made substrates or media exhibit anisotropic uniaxial characteristics.

The research will be further extended to include analysis of waveguide filters filled with man-made metamaterials, which is an advantage the MMM has over other methods. Discussion of metamaterials will be left out of the prior work section and included in the metamaterial section as it is a relatively new field.

Finally, media filled waveguide filters with and without metamaterials are designed, manufactured, RF tested and results compared with the MMM of this research.

1.2 Prior Work

Volumes of literature provide methods for solving waveguide discontinuities problems, describe wave propagation though anisotropic media, and describe techniques for filter design based on the aforementioned subjects. This section seeks to cover previous work done in the subject area, and highlight areas where there is room for expansion. Specifically, it will expand on media filled waveguide filters with arbitrarily oriented optic axis of the media. As mentioned earlier there is prior work done with metamaterials, but this will be saved for the metamaterial chapter.

1.2.1 Waveguide Analysis Using Mode-Matching Method

Analyses of waveguide discontinuities using the mode-matching method (MMM) have been around for a long time. All things in electromagnetics fundamentally have roots extending back to Maxwell's equations so credit must in some form be given to Maxwell. However, Wexler [1] in 1976 lays the foundation for MMM. He states in modal analysis the amplitudes of normal modes are chosen to satisfy boundary conditions. This method is also useful for multimode propagation cases, and because it conforms closely to physical reality it has the widest applications. This is the main advantage of MMM over other methods. Itoh [2] and Mittra and Lee's [3] texts both provide in depth analysis of formulation of mode-matching problems, as well as detailed derivations for special case discontinuities. Itoh also discusses the importance of numerical convergence, which will be mentioned later. Itoh's formulations and

recommendations are the base for the mode-matching techniques of this research. Safavi-Naini and MacPhie [4] solve waveguide discontinuities by a different method but similar ideology. Safavi-Nanini and MacPhie formulate that power propagating in one waveguide must be continuous across boundaries due to conservation of power. They then go on to derive reflection and transmission coefficients for various circular waveguide discontinuities. Jarry and Beneat [5] expand on MMM with the solution for an arbitrary double step discontinuity and provide results assuming the presence of fundamental mode. Chu *et al* [6] extend the theory of mode-matching to microstrip problems, which is not directly applicable to this research but still useful nonetheless. Patzelt and Arndt [7] apply mode matching theory to double step and cascaded discontinuities with applications for X-band filters. In Papziner and Arndt [8] mode matching is applied to analyze coupling from rectangle to rectangle and rectangle to circular irises for filter applications. Numerical results are then compared with measured results. Hoppe [9] computes reflection and transmission coefficients using MMM for circular, rectangular, and coaxial discontinuities. Wade and MacPhie [10] use MMM to compute circular to rectangular junctions similar to [4], but using mode-matching instead of power technique. Ihmels and Arndt [11] use MMM to solve for cutoff frequencies and s-parameters for the junction of rectangular waveguides by a cross iris. Hajimowlana *et al* [12] solve for reflection and transmission coefficients between the discontinuities of double ridged waveguides.

1.2.2 Alternative Methods for Waveguide Analysis

There are also numerous other techniques for solving waveguide discontinuity problems. Contour-integral and Integral-Equation are two alternate common methods for solving waveguide discontinuity problems in literature [13-14]. Hybrid mode-matching finite element

technique is another common method to solve waveguide discontinuity problems where FEM is used to characterize fields within the arbitrarily shaped discontinuity and a modified MMM is then used to solve for the total fields [15-17]. Rozzi [18] uses Green's function to yield equations for magnetic and electrical fields, and then uses a Fourier Expansion to solve for the admittance. Weisshaar [19] solves for cascaded waveguide discontinuities by determining an equivalent circuit model and treating the discontinuities as coupled transformers, and then compares with MMM. Finding an equivalent network model then solving for propagation constants is another alternate methodology for solving waveguide discontinuity problems [20-21].

1.2.3 Media Filled Waveguides

Some of the early work done on analyzing wave propagation in media filled waveguides was performed by Engineer and Nag [22] in 1965 when they derive y-dependent E-field propagation constants for media filled, and partially filled waveguides in the presence of a transverse magnetic field. In 1967 Davies [23] uses Berk's variational expression to solve for propagation constants when the optic axis is rotated by an arbitrary angle between parallel to the direction of propagation and 90^{o}. Liu *et al* [24] use eigenvalues and eigenvectors to solve for propagation constants in a waveguide filled with uniaxial media. The optic axis of the media is aligned with the direction of wave propagation. Sobrinho and Giarolas [25] solve the problem of a waveguide filled with uniaxial media using a finite-difference method to solve for propagation constants when the optic axis is not aligned with the direction of propagation. Damaskos *et al* [26] solve Maxwell's equations for a biaxial media, and then assume x or y field independence to decouple the field equations and solve for dispersion relations. Sheen [27] takes a biaxial

media filled waveguide, and makes the appropriate assumptions to decouple Maxwell's equations. Sheen then solves for all 6 field components for TE and TM modes. Chen [28] derives propagation constants in biaxial media, for an arbitrary propagation angle, for an arbitrary coordinate system. Pozar [29] derives dispersion relations for TE and TM modes radiating from a patch antenna on uniaxial media into free space. Krowne [30] uses a Method of Moments approach to solve for the 6 field components created by a line current source sandwiched in between biaxial media and a simple media. There is also extensive work done on propagation in dielectric waveguides but this type of waveguide is not applicable to this work. However, Yakovlev *et al* and Jalaleddine's works are mentioned as some of their methodology can be applied to this work [31-32].

1.2.4 Waveguide Filters

Using the cascaded solutions of waveguide discontinuity problems filters are formed and analyzed. One common way to accomplish this is to use MMM to solve for the discontinuity problem, and then cascade the solutions connected by waveguide transmission lines [33—36].

1.3 Waveguide Basics

This work ultimately analyzes and designs waveguide filters. This requires an understanding of the equations that govern waveguides. Pozar, Collin, Kong, and Harrington [37]–[40] all give excellent derivations for waveguides, and the reader is invited to explore these texts further. The waveguide in Figure 1.1 has x dimension of "a", and y dimension of "b". The wave propagates in the z direction, or z is the axis of propagation.

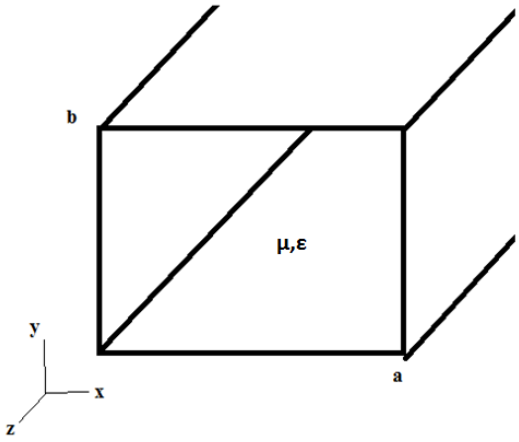

Figure 1.1: Waveguide Cross Section.

Maxwell's Equations are the fundamental starting point for electromagnetic problems and the time-harmonic versions are listed below.

$$\nabla \times \bar{E} = -j\omega\mu\bar{H} \quad (1.1)$$

$$\nabla \times \bar{H} = j\omega\varepsilon\bar{E} \quad (1.2)$$

When $\bar{E}$ and $\bar{H}$ have $e^{-j\beta z}$ dependence, rectangular components of (1.1) and (1.2) are

$$\frac{\partial E_z}{\partial y} + j\beta E_y = -j\omega\mu H_x \quad (1.3)$$

$$-\frac{\partial E_z}{\partial x} - j\beta E_x = -j\omega\mu H_y \quad (1.4)$$

$$\frac{\partial E_y}{\partial x} - \frac{\partial E_x}{\partial y} = -j\omega\mu H_z \quad (1.5)$$

$$\frac{\partial H_z}{\partial y} + j\beta H_y = j\omega\varepsilon E_x \quad (1.6)$$

$$-\frac{\delta H_z}{\delta x} - j\beta H_x = j\omega\varepsilon E_y \quad (1.7)$$

$$\frac{\partial H_y}{\partial x} - \frac{\partial H_x}{\partial y} = j\omega\varepsilon E_z. \quad (1.8)$$

Following similar methods in the recommended text these six equations are solved in terms of H_z and E_z. By solving in terms of H_z and E_z four equations can now fully describe the transverse fields present inside the rectangular waveguide.

$$H_x = \frac{j}{k_c^2}\left(\omega\varepsilon\frac{\partial E_z}{\partial y} - \beta\frac{\partial H_z}{\partial x}\right) \quad 1.9$$

$$H_y = \frac{-j}{k_c^2}\left(\omega\varepsilon\frac{\partial E_z}{\partial x} + \beta\frac{\partial H_z}{\partial y}\right) \quad 1.10$$

$$E_x = \frac{-j}{k_c^2}\left(\omega\mu\frac{\partial H_z}{\partial y} + \beta\frac{\partial E_z}{\partial x}\right) \quad 1.11$$

$$E_y = \frac{j}{k_c^2}\left(\omega\mu\frac{\partial H_z}{\partial x} - \beta\frac{\partial E_z}{\partial y}\right) \quad 1.12$$

where

$$k_c^2 = k^2 - \beta^2 \quad 1.13$$

and

$$k = \omega\sqrt{\varepsilon\mu} \quad 1.14$$

Waveguides can only support TE or TM waves because the single wall of the waveguide does not satisfy conditions necessary for TEM wave propagation. TE waves are transverse electric and imply that $E_z = 0$. TM or transverse magnetic waves imply that $H_z = 0$. The field solutions for TE waves are found by setting $E_z = 0$ in eq. (1.9) – (1.12).

$$H_x = \frac{-j}{k_c^2}\left(\beta\frac{\partial H_z}{\partial x}\right) \quad 1.15$$

$$H_y = \frac{-j}{k_c^2}\left(\beta\frac{\partial H_z}{\partial y}\right) \quad 1.16$$

$$E_x = \frac{-j}{k_c^2}\left(\omega\mu\frac{\partial H_z}{\partial y}\right) \quad 1.17$$

$$E_y = \frac{j}{k_c^2}\left(\omega\mu\frac{\partial H_z}{\partial x}\right) \quad 1.18$$

The solutions for TM waves are similarly found by setting $H_z = 0$ in eq. (1.9) – (1.12).

$$H_x = \frac{j}{k_c^2}\left(\omega\varepsilon\frac{\partial E_z}{\partial y}\right) \quad 1.19$$

$$H_y = \frac{-j}{k_c^2}\left(\omega\varepsilon\frac{\partial E_z}{\partial x}\right) \quad 1.20$$

$$E_x = \frac{-j}{k_c^2}\left(\beta\frac{\partial E_z}{\partial x}\right) \quad 1.21$$

$$E_y = \frac{-j}{k_c^2}\left(\beta \frac{\partial E_z}{\partial y}\right) \quad 1.22$$

Pozar [37] tells us that the solution to H_z and E_z must also be a solution to the Helmholtz equation where H_z is assumed to have the form of $H_z(x,y)e^{-j\beta z}$, and is a solution to Helmholtz equation (1.23).

$$\left(\frac{\partial^2}{\partial x^2} + \frac{\partial^2}{\partial y^2} + \frac{\partial^2}{\partial z^2} + k^2\right) H(or\ E)_z = 0 \quad 1.23$$

From separation of variables it is known that a solution for $H_z(x,y)$ is

$$H_z(x,y) = (A\cos k_x x + B\sin k_x x)\left(C\cos k_y y + D\sin k_y y\right) \quad 1.24$$

Hz cannot be found directly from (1.24) but can be substituted back into (1.15) − (1.18). A similar expression for E_z can be substituted into (1.19)−(1.22). With the restrictions of the boundary conditions imposed, the proper values for the coefficients A,B,C,D are determined, and in turn a solution for (1.24) is realized. For a TE wave, (1.24) is substituted back into (1.17)−(1.18) resulting in

$$E_x = \frac{-j\omega\mu\, k_y}{k_c^2}(A\cos k_x x + B\sin k_x x)\left(-C\sin k_y y + D\cos k_y y\right)e^{-j\beta z} \quad 1.25$$

$$E_y = \frac{j\omega\mu\, k_x}{k_c^2}(-A\sin k_x x + B\cos k_x x)\left(C\cos k_y y + D\sin k_y y\right)e^{-j\beta z} \quad 1.26$$

Imposing the boundary conditions that inside the waveguide Ex = 0 at y=0 and b, and that Ey = 0 at x =0 and a, it is seen that B=D=0, and ($k_x = \frac{m\pi}{a}$, $k_y = \frac{n\pi}{b}$). Making the proper substitutions in (1.24), Hz is now known. With A_{mn} equal to an arbitrary amplitude coefficient,

$$H_z(x,y,z) = A_{mn}\cos\frac{m\pi x}{a}\cos\frac{n\pi y}{b}e^{-j\beta z}. \quad 1.27$$

Now that there is a solution for Hz, all transverse fields for TE waves are known and (1.15)−(1.18) become

$$E_x = \frac{j\omega\mu n\pi}{k_c^2 b} A_{mn} \cos\frac{m\pi x}{a} \sin\frac{n\pi y}{b} e^{-j\beta z} \quad 1.28$$

$$E_y = -\frac{j\omega\mu m\pi}{k_c^2 a} A_{mn} \sin\frac{m\pi x}{a} \cos\frac{n\pi y}{b} e^{-j\beta z} \quad 1.29$$

$$H_x = \frac{j\beta m\pi}{k_c^2 a} A_{mn} \sin\frac{m\pi x}{a} \cos\frac{n\pi y}{b} e^{-j\beta z} \quad 1.30$$

$$H_y = \frac{j\beta n\pi}{k_c^2 b} A_{mn} \cos\frac{m\pi x}{a} \sin\frac{n\pi y}{b} e^{-j\beta z} \quad 1.31$$

Following the same procedures used to solve for TE waves, TM wave solutions are solved for yielding

$$E_z(x, y, z) = B_{mn} \sin\frac{m\pi x}{a} \sin\frac{n\pi y}{b} e^{-j\beta z} \quad 1.32$$

And substituting (1.32) back into (1.19)−(1.22) yields the transverse fields for TM waves, which are

$$E_x = -\frac{j\beta m\pi}{k_c^2 a} B_{mn} \cos\frac{m\pi x}{a} \sin\frac{n\pi y}{b} e^{-j\beta z} \quad 1.33$$

$$E_y = -\frac{j\beta n\pi}{k_c^2 b} B_{mn} \sin\frac{m\pi x}{a} \cos\frac{n\pi y}{b} e^{-j\beta z} \quad 1.34$$

$$H_x = \frac{j\omega\varepsilon n\,\pi}{k_c^2 b} B_{mn} \sin\frac{m\pi x}{a} \cos\frac{n\pi y}{b} e^{-j\beta z} \quad 1.35$$

$$H_y = -\frac{j\omega\varepsilon m\pi}{k_c^2 a} B_{mn} \cos\frac{m\pi x}{a} \sin\frac{n\pi y}{b} e^{-j\beta z} \quad 1.36$$

The last thing to consider is β, because for certain values of β waves will either propagate or not. Assume the E field takes the form $E_o e^{-\gamma z}$, where γ=jβ=jk_z. It is known that $k_x^2 + k_y^2 + k_z^2 = k^2$, and

$$k_z = \sqrt{k^2 - \left(\left(\frac{m\pi}{a}\right)^2 + \left(\frac{n\pi}{b}\right)^2\right)} \quad 1.37$$

Harrington [40] states only when the wave number k is greater than the cutoff wave number defined by eq. (1.13) propagation will occur. Harrington defines this with the following equation, and it is valid for TE and TM cases.

$$\gamma_{mn} = jk_z = \begin{cases} j\beta = j\sqrt{k^2 - \left(\left(\frac{m\pi}{a}\right)^2 + \left(\frac{n\pi}{b}\right)^2\right)}, k > k_c \\ \alpha = \sqrt{-k^2 + \left(\left(\frac{m\pi}{a}\right)^2 + \left(\frac{n\pi}{b}\right)^2\right)}, k < k_c \end{cases}, \quad 1.38$$

and

$$k_c^2 = \left(\frac{m\pi}{a}\right)^2 + \left(\frac{n\pi}{b}\right)^2, \quad 1.39$$

where k_c is the cutoff wave number. Eq. (1.38) states only when k>k_c will propagation happen; all other cases will result in evanescent waves. Harrington then goes on to define the wave impedances as follows

$$(Z_o)_{mn}^{TE} = \frac{E_x}{H_y} = -\frac{E_y}{H_x} = \frac{\omega\mu}{k_z} = \begin{cases} \frac{\omega\mu}{\beta}, f > f_c \\ \frac{j\omega\mu}{\alpha}, f < f_c \end{cases} \quad 1.40$$

$$(Z_o)_{mn}^{TM} = \frac{E_x}{H_y} = -\frac{E_y}{H_x} = \frac{k_z}{\omega\varepsilon} = \begin{cases} \frac{\beta}{\omega\varepsilon}, f > f_c \\ \frac{\alpha}{j\omega\varepsilon}, f < f_c \end{cases} \quad 1.41$$

where f_c is the cutoff frequency and f is the operating frequency. Equations (1.37)−(1.41) are of particular interest because they are used extensively in solving waveguide discontinuities using the mode-matching method presented in the next section.

2 Mode-Matching

As mentioned in the introduction, mode-matching is a well-studied topic, and provides some advantages over other methods [1]. This section will present the theory of Mode-Matching, and discuss some results.

2.1 Simple Step-Discontinuity Problem

As stated by Itoh's text [2], Mode Matching is one of the most frequently used methods to solve waveguide problems. Mode-Matching is especially useful when the problem is a junction of two regions, because the fields in each waveguide region are explicitly expressible in each region. At the junction or discontinuity, boundary conditions are used to solve for the unknown fields. Using Itoh's method the problem illustrated in Figure 2.1 cut along the x-z plane is solved.

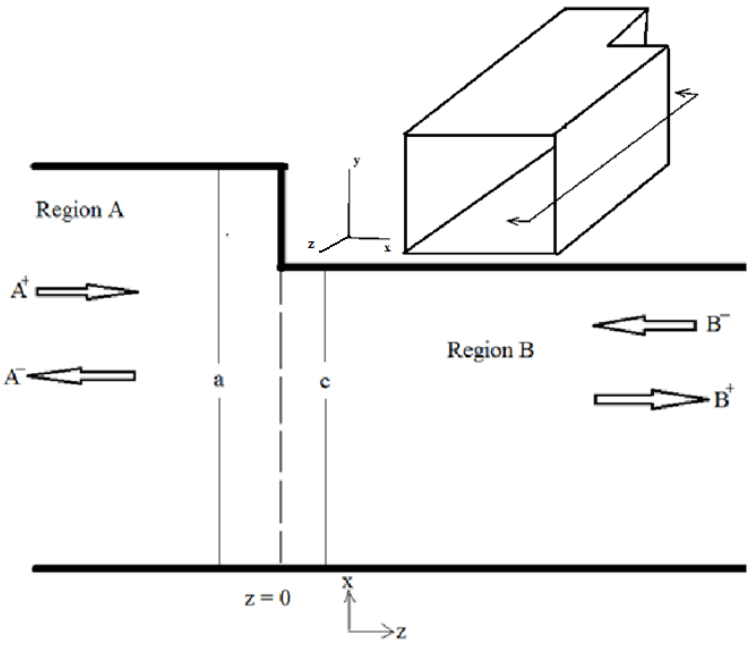

Figure 2.1 Simple Step Discontinuity

This problem consists of the junction of two waveguides; Waveguide 1 of region A and waveguide 2 of region B. Region A has a height of a, and a depth of b out of the page (not shown). Region B has a height of c and the same depth of b out of the page. Region A has wave amplitude of A^+ entering the region and wave amplitude of A^- exiting the region. Similarly, region B has wave amplitude of B^- entering and B^+ exiting. At z=0 the two waveguides are connected at a step discontinuity junction. The problem now is to determine these wave amplitudes.

2.2 Expression of Fields

Assuming for the sake of argument TE modes are the only modes propagating. Referring back to (1.28)−(1.31), the transverse fields are known for a rectangular waveguide. The equations are repeated for convenience below.

$$E_x = \frac{j\omega\mu n\pi}{k_c^2 b} A_{mn} \cos\frac{m\pi x}{a} \sin\frac{n\pi y}{b} e^{-j\beta z} \quad 2.1$$

$$E_y = -\frac{j\omega\mu m\pi}{k_c^2 a} A_{mn} \sin\frac{m\pi x}{a} \cos\frac{n\pi y}{b} e^{-j\beta z} \quad 2.2$$

$$H_x = \frac{j\beta m\pi}{k_c^2 a} A_{mn} \sin\frac{m\pi x}{a} \cos\frac{n\pi y}{b} e^{-j\beta z} \quad 2.3$$

$$H_y = \frac{j\beta n\pi}{k_c^2 b} A_{mn} \cos\frac{m\pi x}{a} \sin\frac{n\pi y}{b} e^{-j\beta z} \quad 2.4$$

In order to express the above equations in line with Harrington's text the substitution of $j\beta = \gamma_{mn}$ is made and all coefficient terms are absorbed into one coefficient of A_{mn}, where

$$\gamma_{mn} = j\sqrt{k^2 - \left(\left(\frac{m\pi}{a}\right)^2 + \left(\frac{n\pi}{b}\right)^2\right)} \quad 2.5$$

and k is the free space wave number, a is the height of the waveguide, and b is the depth of the waveguide. For example, looking at Figure 2.1 in region B, a = c, and b=b. After making the

required substitutions for γ_{mn} and absorbing all terms into a common coefficient (2.1)−(2.4) become

$$E_x = -A_{mn}\frac{na}{mb}\cos\frac{m\pi x}{a}\sin\frac{n\pi y}{b}e^{-\gamma_{mn}z} \quad 2.6$$

$$E_y = A_{mn}\sin\frac{m\pi x}{a}\cos\frac{n\pi y}{b}e^{-\gamma_{mn}z} \quad 2.7$$

$$H_x = A'_{mn}\sin\frac{m\pi x}{a}\cos\frac{n\pi y}{b}e^{-\gamma_{mn}z} \quad 2.8$$

$$H_y = A'_{mn}\frac{na}{mb}\cos\frac{m\pi x}{a}\sin\frac{n\pi y}{b}e^{-\gamma_{mn}z} \quad 2.9$$

As mentioned, it is assumed that only TE modes are propagating in the waveguide. It is now also assumed that only the TE_{M0} mode is present. By making this assumption (2.6)−(2.9) are reduced to

$$E_x = 0 \quad 2.10$$

$$E_y = A_m\sin\frac{m\pi x}{a}e^{-\gamma_m z} \quad 2.11$$

$$H_x = A'_m\sin\frac{m\pi x}{a}e^{-\gamma_m z} \quad 2.12$$

$$H_y = 0 \quad 2.13$$

where A_m is the coefficient of the electric field, and $A_m^{'}$ is the coefficient of the magnetic field. For the purpose of commonality it is desired to write the H-fields in terms of the corresponding E-fields. Again using Harrington's E-field/H-field relations one can determine the relation

$$H_x = \frac{-E_y}{(Z_o)_{mn}^{TE}} = -(Y_o)_{mn}^{TE}E_y \quad 2.14$$

where,

$$(Y_o)_{mn}^{TE} = \frac{\gamma_{mn}}{j\omega\mu} \quad 2.15$$

The correct signs for each field component are determined through the Poynting theorem, where $S = \bar{E} \times \bar{H}$ and S is in the direction of power flow. After using (2.15) and the Poynting Theorem, (2.11)−(2.12) are written in terms of a common coefficient.

$$E_y = A_m \sin\frac{m\pi x}{a} e^{-\gamma_m z} \quad 2.16$$

$$H_x = -Y_m A_m \sin\frac{m\pi x}{a} e^{-\gamma_m z} \quad 2.17$$

Now the total field present in the waveguide is a summation of all the wave amplitudes traveling forward and all wave amplitudes traveling backward.

$$E_{y,Total} = \sum_{m=1}^{M} (A_m^+ \sin\frac{m\pi x}{a} e^{-\gamma_m z} + A_m^- \sin\frac{m\pi x}{a} e^{\gamma_m z}) \quad 2.18$$

$$H_{x,Total} = \sum_{m=1}^{M} (Y_m A_m^- \sin\frac{m\pi x}{a} e^{\gamma_m z} - Y_m A_m^+ \sin\frac{m\pi x}{a} e^{-\gamma_m z}) \quad 2.19$$

Where A_m^+ is the amplitude of the mth mode traveling forward in the waveguide, A_m^- is the amplitude of the mth mode traveling backward in the waveguide, and

$$\gamma_m = j\sqrt{k^2 - \left(\frac{m\pi}{a}\right)^2} \quad 2.20$$

$$Y_m = \frac{\gamma_m}{j\omega\mu} \quad 2.21$$

2.3 Fields of Step-Discontinuity Problem

Looking at Figure 2.1 one can write an expression for the total fields in region A and B using the results of the last section. Using (2.18)−(2.19) and assuming only TE_{m0} modes present, the total fields in region A are

$$E_y^A = \sum_{m=1}^{M} (A_m^+ \sin\frac{m\pi x}{a} e^{-\gamma_{am} z} + A_m^- \sin\frac{m\pi x}{a} e^{\gamma_{am} z}) \quad 2.22$$

$$H_x^A = \sum_{m=1}^{M} (Y_{am} A_m^- \sin\frac{m\pi x}{a} e^{\gamma_{am} z} - Y_{am} A_m^+ \sin\frac{m\pi x}{a} e^{-\gamma_{am} z}) \quad 2.23$$

and in region B

$$E_y^B = \sum_{n=1}^{K}(B_n^+ \sin\frac{n\pi x}{c} e^{-\gamma_{bn} z} + B_n^- \sin\frac{n\pi x}{c} e^{\gamma_{bn} z}) \quad 2.24$$

$$H_x^B = \sum_{n=1}^{K}(Y_{bn} B_n^- \sin\frac{n\pi x}{c} e^{\gamma_{bn} z} - Y_{bn} B_n^+ \sin\frac{n\pi x}{c} e^{-\gamma_{bn} z}) \quad 2.25$$

Where M is the number of modes present in region A, K is the number of modes present in region B, and the propagation constant is

$$\gamma_{ip} = j\sqrt{k^2 - \left(\left(\frac{p\pi}{i'}\right)^2\right)}, i = a \text{ or } b, i' = a \text{ for } i = a \text{ and } i' = c \text{ for } i = b, \quad 2.26$$

and the admittance is

$$Y_{ip} = \frac{\gamma_{ip}}{j\omega\mu}, i = a \text{ or } b, \quad 2.27$$

where a or b corresponds to the region of waveguide. Setting z=0 describes the fields at the discontinuity in Figure 2.1, and reduces (2.22)−(2.25) to

$$E_y^A = \sum_{m=1}^{M}(A_m^+ \sin\frac{m\pi x}{a} + A_m^- \sin\frac{m\pi x}{a}) \quad 2.28$$

$$H_x^A = \sum_{m=1}^{M}(Y_{am} A_m^- \sin\frac{m\pi x}{a} - Y_{am} A_m^+ \sin\frac{m\pi x}{a}) \quad 2.29$$

$$E_y^B = \sum_{n=1}^{K} B_n^+ \sin\frac{n\pi x}{c} + B_n^- \sin\frac{n\pi x}{c} \quad 2.30$$

$$H_x^B = \sum_{n=1}^{K} Y_{bn} B_n^- \sin\frac{n\pi x}{c} - Y_{bn} B_n^+ \sin\frac{n\pi x}{c} \quad 2.31$$

which are the total E and H fields in regions A and B. At the discontinuity, boundary conditions must be preserved. In the case of a source free region the tangential electric and magnetic fields must equal each other, or $E_{t1} = E_{t2}$ *and* $H_{t1} = H_{t2}$. The total electric fields at the discontinuity are defined as

$$E_y^{z=0} = \sum_{m=1}^{M}(A_m^+ \sin\frac{m\pi x}{a} + A_m^- \sin\frac{m\pi x}{a}) = \sum_{n=1}^{K}(B_n^+ \sin\frac{n\pi x}{c} + B_n^- \sin\frac{n\pi x}{c}) \quad 2.32$$

and the total magnetic fields are defined as

$$H_x^{z=0} = \sum_{m=1}^{M}(Y_{am}\,A_m^- \sin\frac{m\pi x}{a} - Y_{am}\,A_m^+ \sin\frac{m\pi x}{a})$$

$$= \sum_{n=1}^{K}(Y_{bn}\,B_n^- \sin\frac{n\pi x}{c} - Y_{bn}\,B_n^+ \sin\frac{n\pi x}{c}) \qquad 2.33$$

It desired to eliminate the x dependence from the left hand side of (2.32). This is accomplished by taking advantage of mode orthogonality as stated by Morse and Feshbach [41] that

$$(E_n^* \cdot E_m) = \int \psi_n(x)\psi_m(x)dx = \begin{cases}\frac{A}{2}, & m = n\\ 0, & m \neq n\end{cases} \qquad 2.34$$

where A is the magnitude of the function squared. By multiplying both sides of (2.32) by $\sin\frac{m\pi x}{a}$, changing both summations indices to p, integrating from x=0 to x=c, using E_y^A=0 for c≤x≤a, and making use of (2.34), (2.32) now becomes

$$(A_m^+ + A_m^-)\frac{a}{2} = \sum_{p=1}^{K}\left(B_p^+ + B_p^-\right)H_{mp} \text{ for } m\text{=1,2,…,}M \qquad 2.35$$

and

$$H_{mp} = \int_0^c \sin\frac{m\pi x}{a}\sin\frac{p\pi x}{c}\,dx = -\frac{ac}{2\pi(cm+ap)}\sin\left(\frac{\pi mc}{a} + \pi p\right) + \frac{ac}{2\pi(cm-ap)}\sin\left(\frac{\pi mc}{a} - \pi p\right). \qquad 2.36$$

A similar procedure is now done to eliminate the x dependence on the right hand side of (2.33). Multiplying (2.33) by $\sin\frac{v\pi x}{c}$ and integrating from x=0 to x=c, only the term for which *n*=*v* on the right hand side of (2.33) survives so that

$$\sum_{m=1}^{M}(A_m^- - A_m^+)Y_{am}\,H_{mv} = (B_v^- - B_v^+)Y_{bv}\,\frac{c}{2} \text{ for } v\text{=1,2,…,}K \qquad 2.37$$

It is now seen there are four unknowns $A^+, A^-, B^+,$ and B^- and two equations. The following sections describe the solutions for the reflected and transmitted wave coefficients in terms of the incident wave coefficients. The two equations are displayed below for ease of viewing.

$$(A_m^+ + A_m^-)\frac{a}{2} = \sum_{p=1}^{K}\left(B_p^+ + B_p^-\right)H_{mp}, \quad \text{for } m\text{=1,2,…,}M \qquad 2.38$$

$$\sum_{m=1}^{M}(A_m^- - A_m^+)Y_{am}\,H_{mv} = (B_v^- - B_v^+)Y_{bv}\,\frac{c}{2}, \quad \text{for } v=1,2,\ldots,K \tag{2.39}$$

2.3.1 Transmission Coefficients in Region B

This section contains the derivations for the transmission coefficients in region B, B^+, when the waveguide junction is excited from region A. First, (2.38) is solved for A^-.

$$A_m^- = \frac{2}{a}\sum_{p=1}^{K}\left(H_{mp}\,B_p^+\right) + \frac{2}{a}\sum_{p=1}^{K}\left(H_{mp}\,B_p^-\right) - A_m^+, \text{ for } m = 1,2,\ldots,M \tag{2.40}$$

Next, it is assumed that region B is perfectly matched so that no reflection of waves occurs. This is accomplished by setting $B_p^- = 0$, for p=1,2,…,K. Equation (2.40) now reduces to

$$A_m^- = \frac{2}{a}\sum_{p=1}^{K}\left(H_{mp}\,B_p^+\right) - A_m^+, \text{ for } m = 1,2,\ldots,M \tag{2.41}$$

(2.41) is now put into (2.39) yielding

$$\sum_{m=1}^{M}\left(\left(\frac{2}{a}\sum_{p=1}^{K}\left(H_{mp}\,B_p^+\right) - A_m^+\right) - A_m^+\right)Y_{am}\,H_{mv} = (B_v^- - B_v^+)Y_{bv}\,\frac{c}{2}, \quad \text{for } v=1,2,\ldots,K \tag{2.42}$$

Interchanging the order of summations and setting $B_v^- = 0$, for v=1,2,…,K,

$$\sum_{p=1}^{K}\left(\sum_{m=1}^{M}\left(\frac{2}{a}Y_{am}\,H_{mv}H_{mp}\,B_p^+\right)\right) + Y_{bv}\,\frac{c}{2}B_v^+ = 2\sum_{m=1}^{M}(Y_{am}\,H_{mv}A_m^+) \text{ for } v=1,2,\ldots,K \tag{2.43}$$

One last assumption is made in order to solve for the transmission coefficient. This is that the waveguide in region A is excited by only a dominant coefficient. This is that the waveguide in region A is excited by only a TE_{10}, which is the dominant mode for waveguides. This is accomplished by enforcing the following requirement.

$$A_m^+ = \begin{cases} 1, for\ m = 1 \\ 0, for\ all\ else \end{cases} \tag{2.44}$$

This reduces (2.43) to

$$\sum_{p=1}^{K}\left[\left(\sum_{m=1}^{M}\left(\frac{2}{a}Y_{am}\,H_{mv}H_{mp}\right)\right) + Y_{bv}\,\frac{c}{2}\delta_{vp}\right]B_p^+ = 2Y_{a1}H_{1v}\ for\ v = 1,2,\ldots,K \tag{2.45}$$

The left hand side is viewed as a product of a K×K matrix with a Kx1 vector, and the right hand side as a K×1 vector. Equation (2.45) has the form

$$\begin{bmatrix} LHS_{11} & \cdots & LHS_{1K} \\ \vdots & \ddots & \vdots \\ LHS_{K1} & \cdots & LHS_{KK} \end{bmatrix} B^{+} = \begin{bmatrix} RHS_1 \\ \vdots \\ RHS_K \end{bmatrix} \qquad 2.46$$

Since all matrix elements except those of B^+ are known, the unknown elements of B^+ are solved with simple matrix inversion. The elements of B^+, which are called transmission coefficients, are now defined.

2.3.2 Reflection Coefficient of Region A

The reflection coefficient in region A, A^-, is the amplitude of the reflected waves in region A when the junction is excited from region A, and region B is assumed to be perfectly matched. First, the transmission coefficients of (2.45) are solved for; call them B_p^+ for p=1,2,…,K. They are then substituted into (2.41) with the same assumption of (2.44).

$$A_m^- = \frac{2}{a}\sum_{p=1}^{K}\left(H_{mp}\, B_p^+\right) - \delta_{m1} \quad \text{for } m = 1,2,\ldots,M \qquad 2.47$$

2.3.3 Reflection Coefficient of Region B

The reflection coefficient of region B, B^+, is the amplitude of the reflected waves when the waveguide junction is excited from region B. It is important to note that B^+ is no longer the transmitted wave when the assumption that the junction is excited from region B is made. First, (2.38) is solved for A_m^-

$$A_m^- = \frac{2}{a}\sum_{p=1}^{K}\left(B_p^+ + B_p^-\right)H_{mp} - A_m^+ \qquad 2.48$$

Equation (2.48) is substituted into eq. (2.39) resulting in

$$\sum_{m=1}^{M}\left(\left(\frac{2}{a}\sum_{p=1}^{K}\left(B_p^+ + B_p^-\right)H_{mp} - A_m^+\right) - A_m^+\right) Y_{am}\, H_{mv} = (B_v^- - B_v^+)Y_{bv}\,\frac{c}{2}, \qquad \text{for } v=1,2,\ldots,K \quad 2.49$$

It is assumed that region A is perfectly matched, which results in no reflected waves or A_m^+=0.

After this assumption and regrouping

$$\sum_{p=1}^{K}\left(\sum_{m=1}^{M}\left(\frac{2}{a}Y_{am}\,H_{mv}H_{mp}\,B_p^+\right)\right)+\frac{c}{2}Y_{bv}B_v^+=\frac{c}{2}Y_{bv}B_v^--\sum_{p=1}^{K}\left(\sum_{m=1}^{M}\left(\frac{2}{a}Y_{am}\,H_{mv}H_{mp}\,B_p^-\right)\right),\ \text{for } v=1,2,\dots,K \qquad 2.50$$

The same assumption that only a single dominant mode excitation is also made when the wave guide is excited from region B:

$$B_m^-=\begin{cases}1, for\ m=1\\0, for\ all\ else\end{cases} \qquad 2.51$$

After enforcing this condition (2.50) becomes

$$\sum_{p=1}^{K}\left(\left[\left(\sum_{m=1}^{M}\left(\frac{2}{a}Y_{am}\,H_{mv}H_{mp}\right)\right)+\delta_{vp}\,\frac{c}{2}Y_{bv}\right]B_p^+\right)=\frac{c}{2}Y_{b1}\delta_{v1}-\sum_{m=1}^{M}\left(\frac{2}{a}Y_{am}\,H_{mv}H_{m1}\right),\ \text{for } v=1,2,\dots,K \qquad 2.52$$

Similar to (2.46), pre-multiplying the right hand side of eq. (2.52) by the inverse of the matrix on the left hand side of eq. (2.52) results in the values of the wave amplitudes of the reflected waves in region B when the waveguide junction is excited from region B and region A is assumed to be perfectly matched.

2.3.4 Transmission Coefficient of Region A

The transmission coefficient of region A, A^-, is the amplitude of transmitted wave amplitudes when the waveguide junction is excited from region B. It is again important to note that A^- is no longer the reflected wave when the assumption that the junction is excited from region B is made. Equation (2.52) provides the amplitudes of the reflected waves of region B when the waveguide junction is excited from region B. These values are, call them B^+ for simplicity, are then put into eq. (2.48) while still maintaining eq. (2.51) and A_m^+=0 for all m.

$$A_m^- = \frac{2}{a}\sum_{p=1}^{K}(B_p^+ H_{mp} + \delta_{p1} H_{m1}), \text{ for } m = 1,2,\ldots,M \quad (2.53)$$

2.4 Normalization of Wave Amplitude Coefficients

The previous section describes the methodology in deriving all transmission and reflection coefficients of TE_{m0} modes assuming a dominant TE_{10} mode excitation. All derived modes must now be normalized to the incident TE_{10} mode. Assume all modes entering the waveguide junction from region A are normalized, and all modes exiting the waveguide junction from region B are normalized. Normalized coefficients are defined as follows

$$\widehat{A_m^+} = \alpha_m A_m^+ \quad (2.54)$$

$$\widehat{B_p^+} = \beta_p B_p^+ \quad (2.55)$$

where $\widehat{A_m^+}$ and $\widehat{B_p^+}$ are the normalized coefficients, and α_m and β_p are scaling coefficients. It is also known that power is proportional to the square of the amplitude so that

$$P_m^{A+} = \omega_m^A |A_m^+|^2 \quad (2.56)$$

$$P_p^{B+} = \omega_p^B \left|B_p^+\right|^2. \quad (2.57)$$

where ω_m^A and ω_p^B are constants that will be found later. Using (2.54)−(2.55) in (2.56)−(2.57) respectively, yields

$$P_m^{A+} = \frac{\omega_m^A}{\alpha_m^2}\left|\widehat{A_m^+}\right|^2 \quad (2.58)$$

$$P_p^{B+} = \frac{\omega_p^B}{\beta_p^2}\left|\widehat{B_p^+}\right|^2 \quad (2.59)$$

Equating powers associated with equal magnitudes of normalized coefficients we obtain

$$\frac{\omega_m^A}{{\alpha_m}^2} = C^2 = \frac{\omega_p^B}{{\beta_p}^2}, \text{ for } m=1,2,\ldots,M \text{ and } p=1,2,\ldots,K \quad (2.60)$$

Now solving for the scaling coefficients in terms of C, where C is an arbitrary constant, provides

$$\alpha_m = \frac{\sqrt{\omega_m^A}}{C} \quad 2.61$$

$$\beta_p = \frac{\sqrt{\omega_p^B}}{C} \quad 2.62$$

Next the power is solved for. The electric and magnetic fields of the mth mode are defined as

$$E^A = A_m^+ \sin\frac{m\pi x}{a} e^{-\gamma_m z}\hat{y} \quad 2.63$$

$$H^A = -A_m^+ Y_{am} \sin\frac{m\pi x}{a} e^{-\gamma_m z}\hat{x} \quad 2.64$$

From basic electromagnetics, power calculation based on eq. (2.63)−(2.64) is defined as

$$P_m^{A+} = Re\left(\int_0^a E^A \times (H^A)^* \cdot \hat{z}dx\right) = |A_m^+|^2 \frac{a}{2} Y_{am} \quad 2.65$$

The same procedure is used to solve for the power in region B

$$P_p^{B+} = Re\left(\int_0^c E^B \times (H^B)^* \cdot \hat{z}dx\right) = \left|B_p^+\right|^2 \frac{c}{2} Y_{bp} \quad 2.66$$

Taking the results of eq. (2.65) and inserting into eq. (2.56), and putting eq. (2.66) into eq. (2.57) results in the following two equations.

$$\omega_m^A = \frac{a}{2} Y_{am} \quad 2.67$$

$$\omega_p^B = \frac{c}{2} Y_{bp} \quad 2.68$$

Equations (2.67)−(2.68) are now put into eq. (2.61)−(2.62) respectively

$$\alpha_m = \frac{\sqrt{\frac{a}{2}Y_{am}}}{C} \quad 2.69$$

$$\beta_p = \frac{\sqrt{\frac{c}{2}Y_{bp}}}{C} \quad 2.70$$

Assuming that α_1=1, (2.69) gives C = $\sqrt{a/2\, Y_{a1}}$ so that (2.69) also gives $\alpha_m = \frac{\sqrt{\frac{a}{2}Y_{am}}}{\sqrt{\frac{a}{2}Y_{a1}}}$ and (2.70) gives

$$\beta_p = \frac{\sqrt{\frac{c}{2}Y_{bp}}}{\sqrt{\frac{a}{2}Y_{a1}}} \qquad 2.71$$

The normalized coefficients with respect to the original coefficients are given upon substitution of the previously found α_m into (2.54) and substitution of (2.71) into (2.55).

$$\widehat{A_m^+} = \frac{\sqrt{\frac{a}{2}Y_{am}}}{\sqrt{\frac{a}{2}Y_{a1}}} A_m^+ \qquad 2.72$$

$$\widehat{B_p^+} = \frac{\sqrt{\frac{c}{2}Y_{bp}}}{\sqrt{\frac{a}{2}Y_{a1}}} B_p^+ \qquad 2.73$$

A similar method is used to define normalized coefficients when the waveguide junction is excited from region B yielding

$$\widehat{A_m^-} = \frac{\sqrt{\frac{a}{2}Y_{am}}}{\sqrt{\frac{c}{2}Y_{b1}}} A_m^- \qquad 2.74$$

$$\widehat{B_p^-} = \frac{\sqrt{\frac{c}{2}Y_{bp}}}{\sqrt{\frac{c}{2}Y_{b1}}} B_p^- \qquad 2.75$$

Equations (2.72)−(2.75) define the normalized coefficients. The ratio of the powers associated with two normalized coefficients is the ratio of the squares of their magnitudes.

2.4.1 S-parameter analogy

Figure 2.2 Definition of waves entering and exiting an arbitrary system

Looking at Figure 2.2, and assuming the wave amplitudes are normalized one can define the scattering parameter relations as follows for use later on.

$$A_n^- = S_{11}A_n^+ + S_{12}B_n^- \quad 2.76$$

$$B_n^+ = S_{21}A_n^+ + S_{22}B_n^- \quad 2.77$$

2.5 Numerical Convergence

To obtain exact results using the mode matching method, we need to extend the number of modes to infinity. Practically, and computationally, this is not feasible. Therefore the limits of *M* and *K* in (2.45), (2.47), (2.52), and (2.53) need to be truncated. Itoh [2, p. 604] states that mode matching presents a problem as two infinite series need to be truncated simultaneously. Depending on the truncated values, selected series can converge to different values. This is called relative convergence and can thankfully be avoided. Itoh [2] postulates that if the ratio

K/M is kept close to the ratio c/a convergence will occur. Shih and Gray [42] arrive at this same conclusion and compare with Marcuvitz's [43] results to within 1%.

2.6 Computed Results

The results in this section are based on the geometries contained in Figure 2.3. The waveguide is filled with a vacuum and walls are considered to be perfect electric conductors.

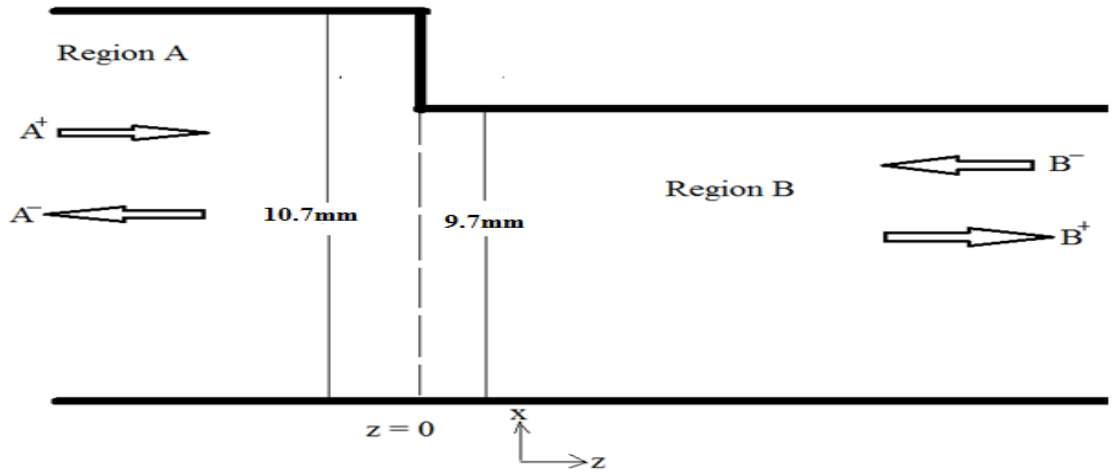

Figure 2.3 Step discontinuity problem with waveguide dimensions

2.6.1 Wave Coefficients

As mentioned earlier, depending on which region of the waveguide junction is excited, $A^+, A^-, B^+,$ and B^- can have different meanings. To avoid confusion the results of the normalized wave amplitudes are plotted in terms of their S-parameter theory described by (2.76)–(2.77).

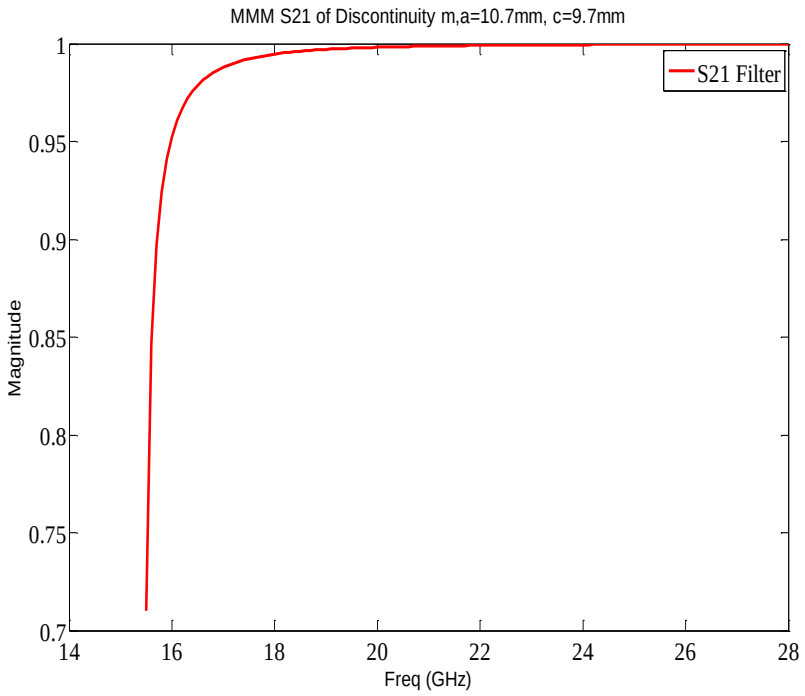

Figure 2.4 Magnitude of Transmission Coefficient (S_{21}) when waveguide discontinuity is excited from region A

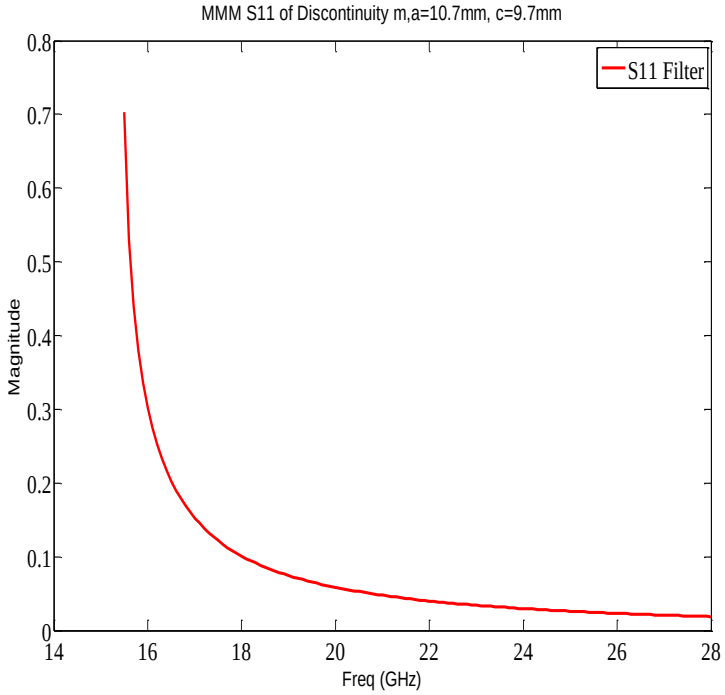

Figure 2.5 Magnitude of Reflection Coefficient (S_{11}) when waveguide discontinuity is excited from region A

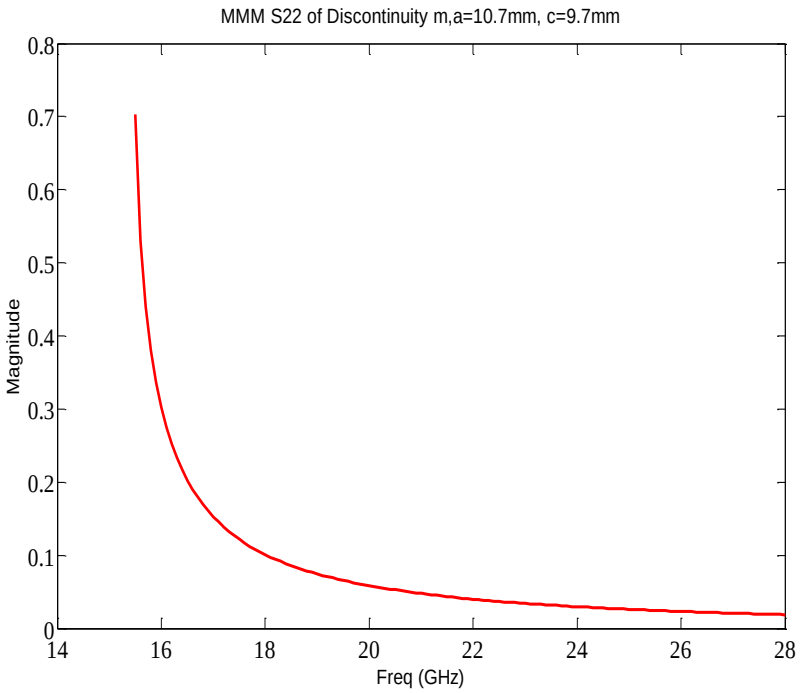

Figure 2.6 Magnitude of Reflection Coefficient (S_{22}) when waveguide discontinuity is excited from region B

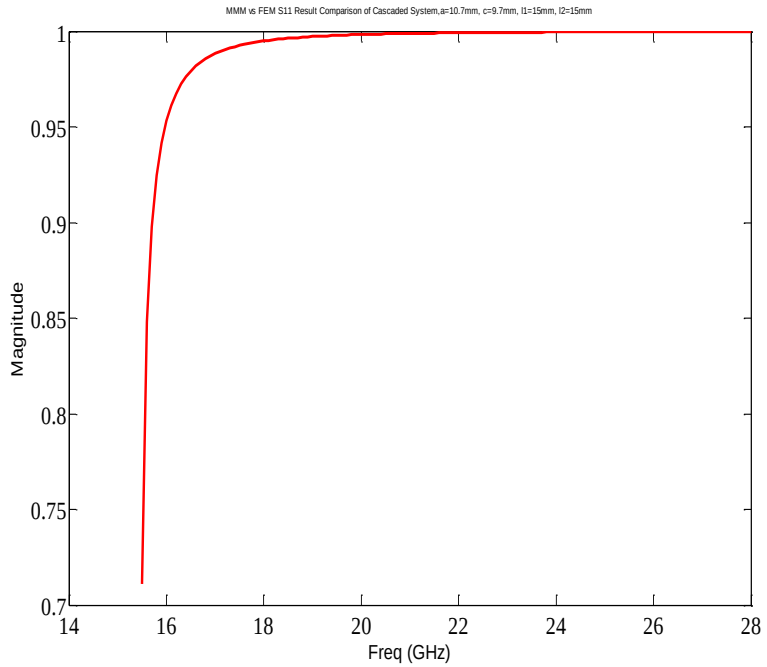

Figure 2.7 Magnitude of Transmission Coefficient (S_{12}) when waveguide discontinuity is excited from region B

As expected, as frequency increases the transmission coefficient approaches unity, while the reflection coefficient approaches zero because the propagating wave is higher, and higher above the cutoff frequency of the waveguide in region B.

2.6.2 Varying Discontinuity Step Size

Looking at Figure 2.8, as x increases one would expect the magnitude of the reflection coefficient in region A to approach zero quicker. Figure 2.9 visually validates this hypothesis.

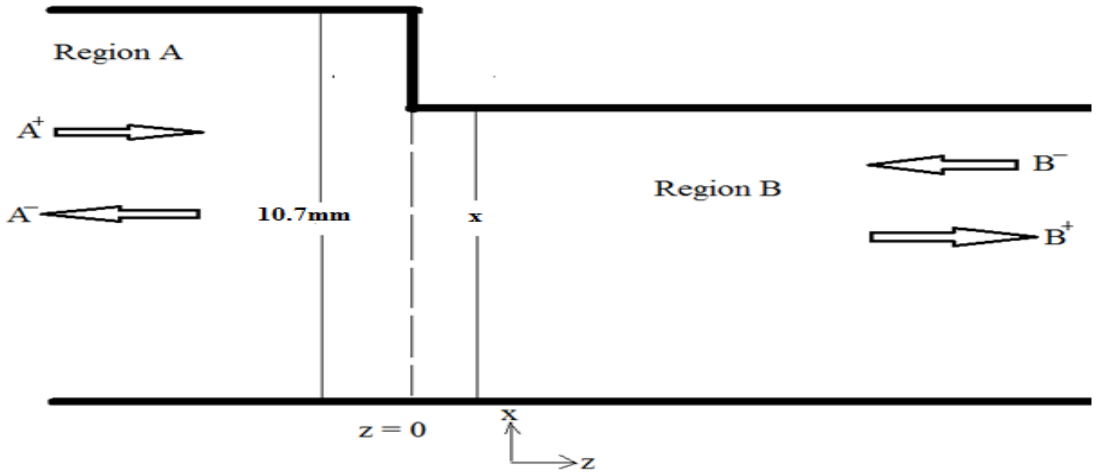

Figure 2.8 Waveguide Discontinuity Junction of varying step x

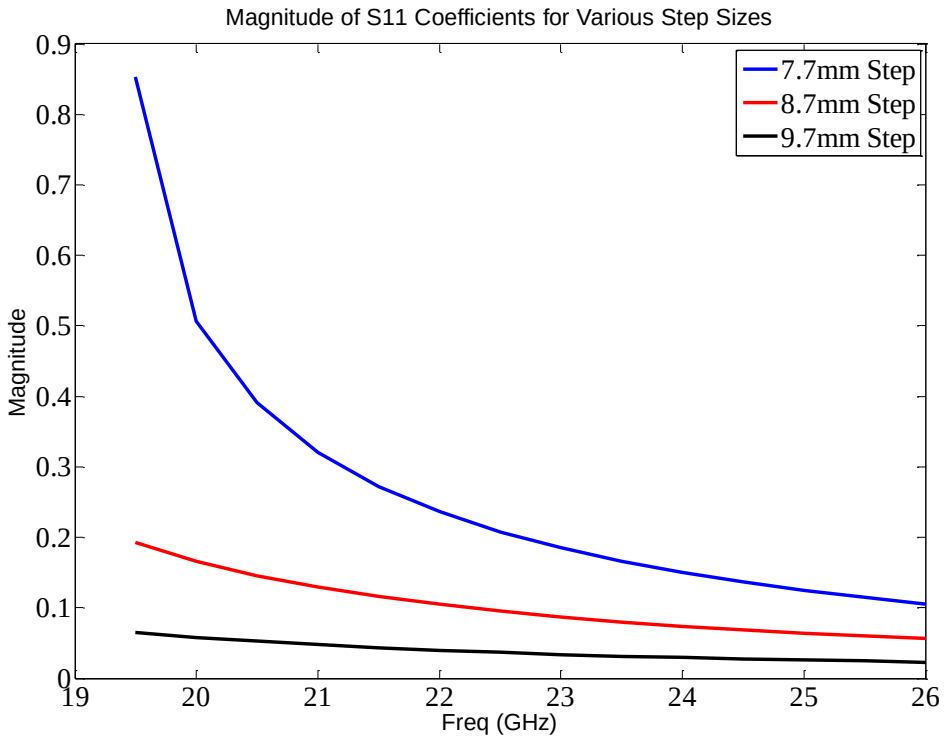

Figure 2.9 Magnitude of Reflection Coefficients in Region A for Varying Step Sizes

2.6.3 Coefficient Symmetry

Looking at Figure 2.3 as a reference at the z=0 plane the S-parameters of this system should be the same as the S-parameters of the same system, but with the dimensions of region A and B reversed as shown in Figure 2.10. In other words, $S_{21}^{A} = S_{12}^{B}\ and\ S_{12}^{A} = S_{21}^{B}$.

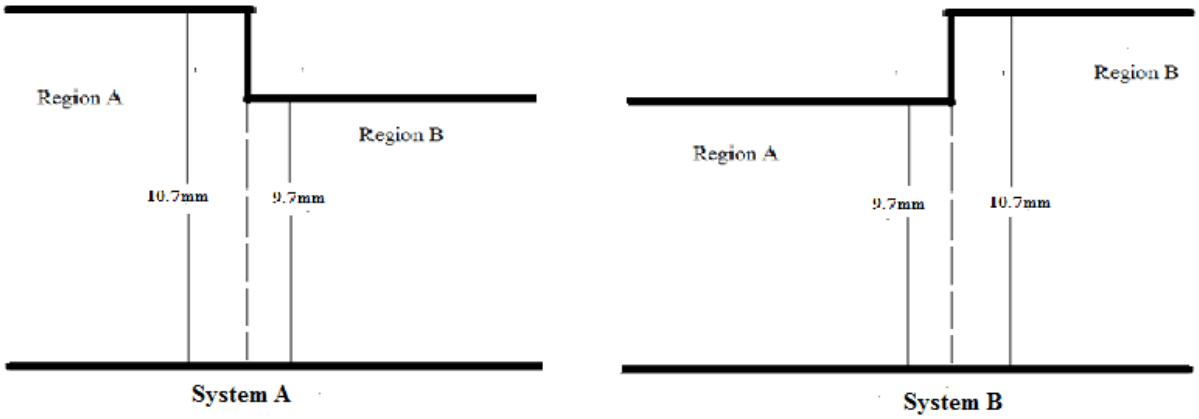

Figure 2.10 Symmetry of System A and System B

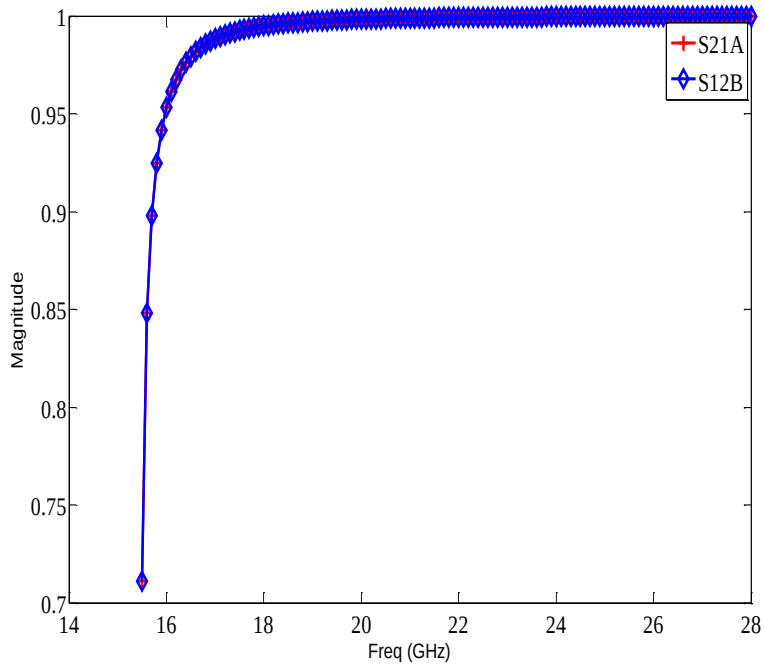

Figure 2.11 Magnitude Comparison of S_{21} from System A vs. S_{12} from System B

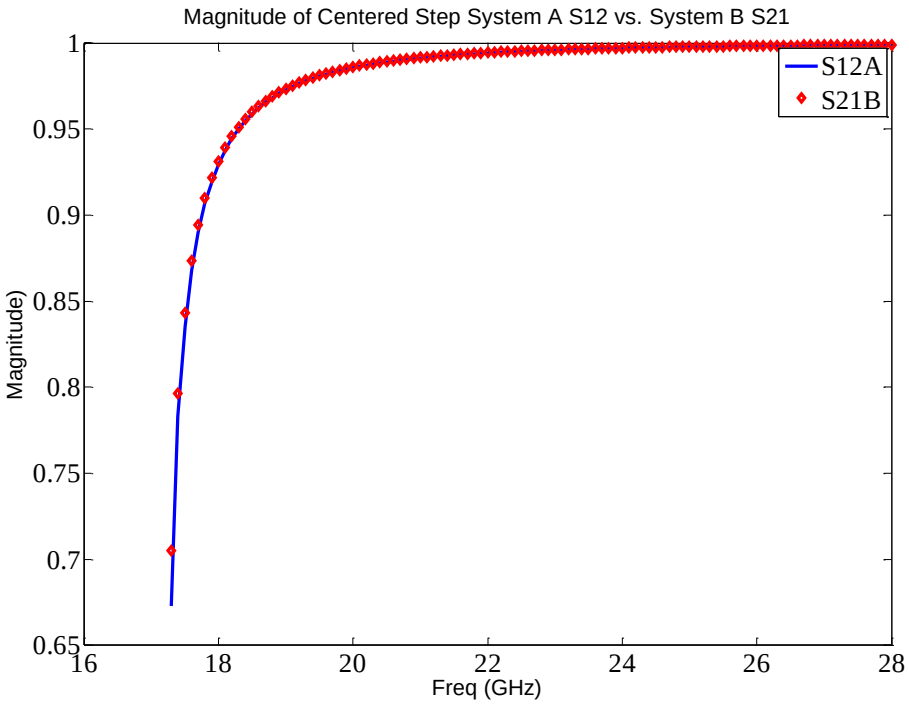

Figure 2.12 Magnitude Comparison of S_{12} from System A vs. S_{21} from System B

2.6.4 Mode-Matching vs. Commercial FEM Results

The previous three sections provide graphical results of numerically computed coefficient magnitudes, and through the use of intuitional tests prove that the numerical results appear to provide results that agree with simple logic. It is desired to see how the numerical results compare with a commercially available Finite Element Solver (FEM) solver such as HFSS [44].

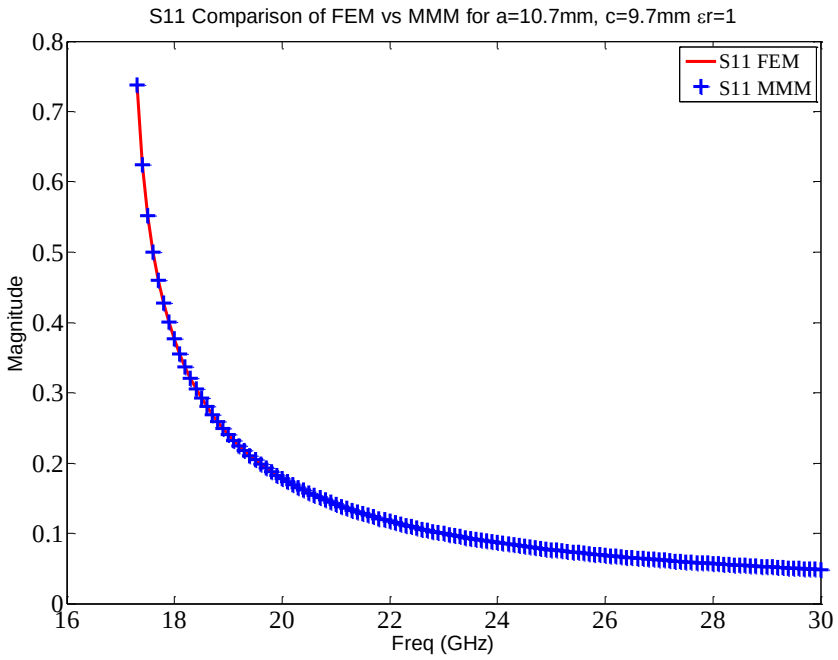

Figure 2.13 Reflection Coefficient Magnitude (S_{11}) of FEM vs. MMM comparison

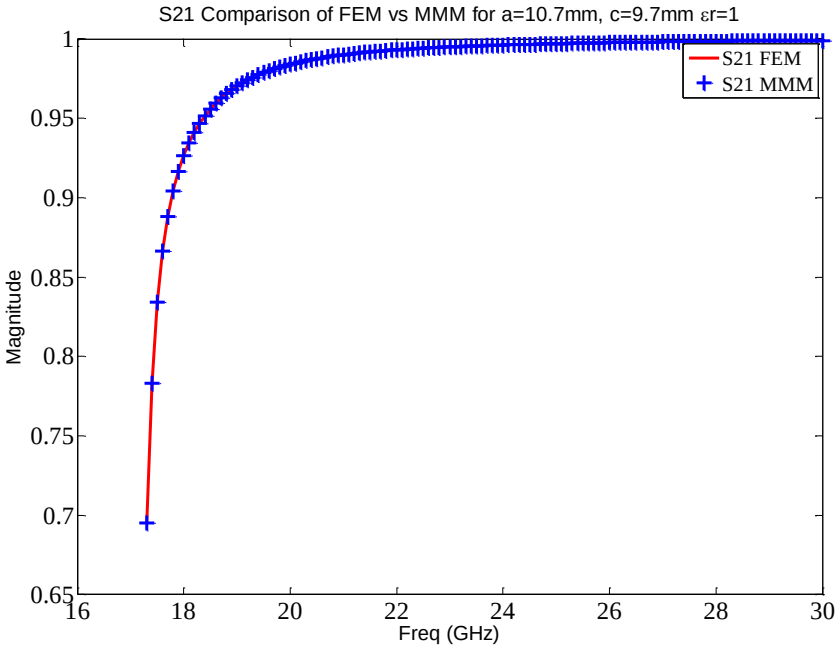

Figure 2.14 Transmission Coefficient Magnitude (S_{21}) of FEM vs. MMM comparison

2.6.5 Phase of Waveguide Junction Discontinuity

The phases of the S21 and S11 coefficients are plotted below. S22 and S12 have been omitted due to symmetry. Based on Figure 2.15 the phase undergoes an abrupt change near cutoff, and then maintains close to 0 degrees of phase change. Theoretically this makes sense, because the wave is traveling over an ideally zero distance, and no phase change is expected over zero distance. Looking at Figure 2.16 the phase also makes sense from simple theory, because the wave travels zero distance into the waveguide and then is reflected that same zero distance back to the output. The phase of S_{11} should sweep linearly from $-\pi$ to π after cutoff. Figure 2.16 shows this trend. There are no phase comparisons with FEM, because FEM results produce errors when trying to solve for exactly zero distance.

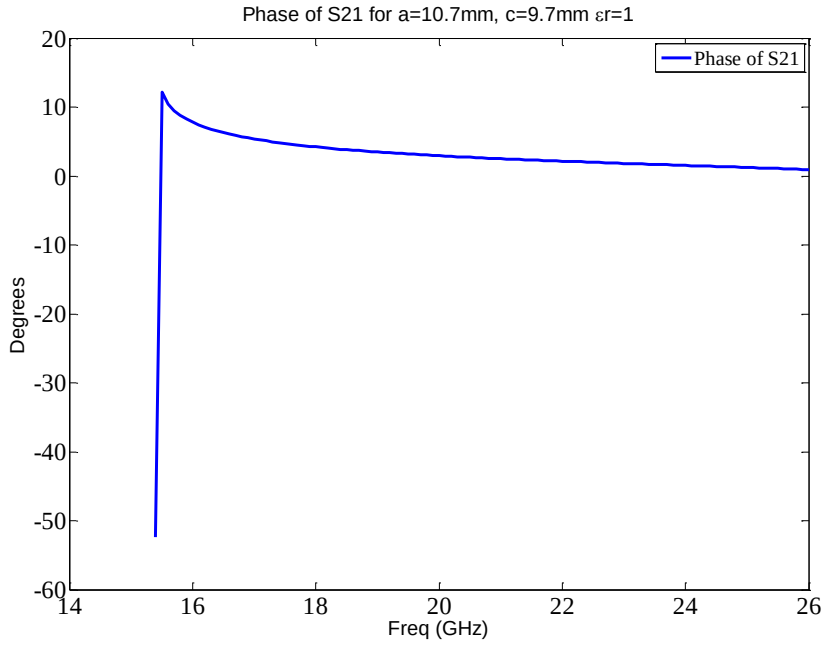

Figure 2.15 Phase of S_{21} Coefficient at z=0

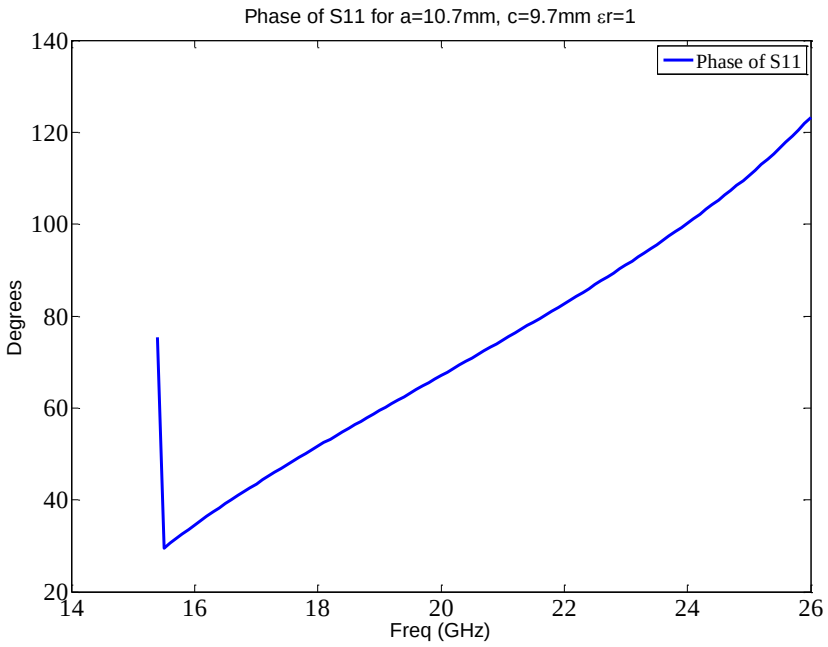

Figure 2.16 Phase of S_{11} Coefficient at z=0

2.7 Double Step Discontinuity

The double step waveguide discontinuity is shown in Figure 2.17. For this scenario the waveguide of region B is now offset from region A's bottom wall by d, and the top of region B is offset from region A's bottom wall by e. Region A's total height is still a, and region B's total height is still c.

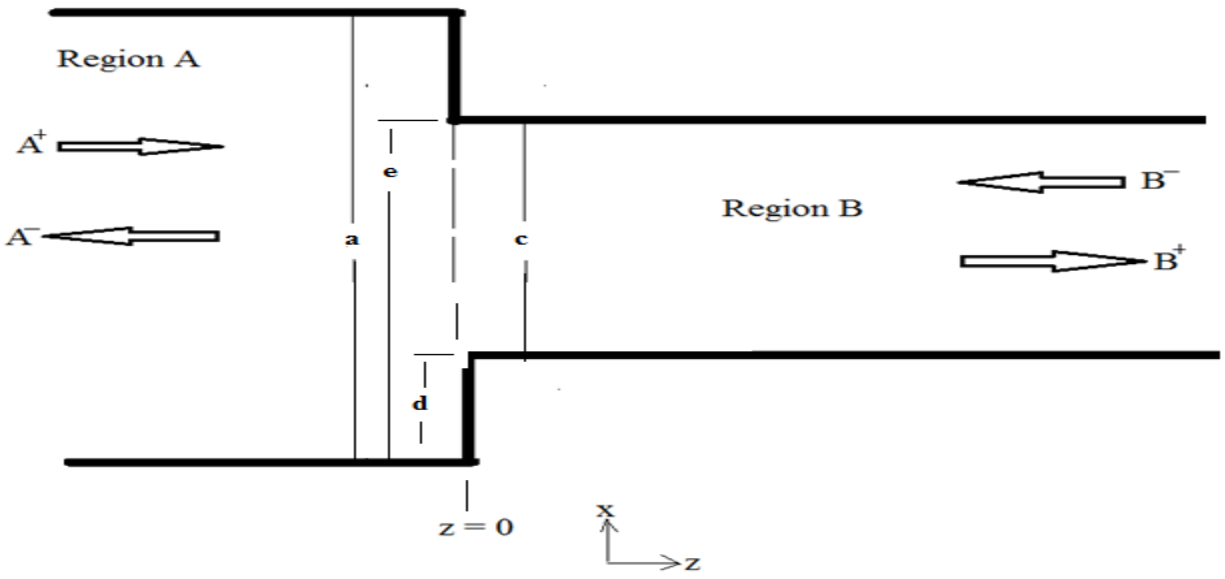

Figure 2.17 Double Step Waveguide Discontinuity

The general form of equations (2.16)−(2.17) still hold, however, the need to enforce the new boundary conditions in region B suggests that fields need to be zero at x=d and x=e. This modifies (2.16)−(2.17) to the new form of

$$E_y^A = A_{am} \sin\frac{m\pi x}{a} e^{\gamma_{am} z} \quad 2.78$$

$$H_x^A = -Y_{am} A_{am} \sin\frac{m\pi x}{a} e^{\gamma_{am} z} \quad 2.79$$

for region A, and for region B to

$$E_y^B = B_{bn} \sin\frac{n\pi (x-d)}{(e-d)} e^{\gamma_{bn} z} \quad 2.80$$

$$H_x^B = -Y_{bn} B_{bn} \sin\frac{n\pi (x-d)}{(e-d)} e^{\gamma_{bn} z} \quad 2.81$$

Equations (2.81)−(2.84) are then used in the exact same manner described in Sections 2.3−2.4, with the exception that H_{mn} now equals

$$H_{mn} = \int_{x=d}^{e} \sin\frac{m\pi x}{a} \sin\frac{n\pi(x-d)}{e-d}\,dx = \frac{a(e-d)\sin\left(\frac{m\pi e}{a}-\frac{n\pi e}{e-d}+\frac{n\pi d}{e-d}\right)}{2\pi(m(e-d)-an)} - \frac{a(e-d)\sin\left(\frac{m\pi e}{a}+\frac{n\pi e}{e-d}-\frac{n\pi d}{e-d}\right)}{2\pi(m(e-d)+an)}$$

$$-\frac{a(e-d)\sin\left(\frac{m\pi d}{a}\right)}{2\pi(m(e-d)-an)} + \frac{a(e-d)\sin\left(\frac{m\pi d}{a}\right)}{2\pi(m(e-d)+an)} \qquad 2.82$$

2.7.1 Numerical Results of Double Step Discontinuity

The results of this section are calculated in the same manner as the previously shown results, except that H_{mn} now is that of (2.82)

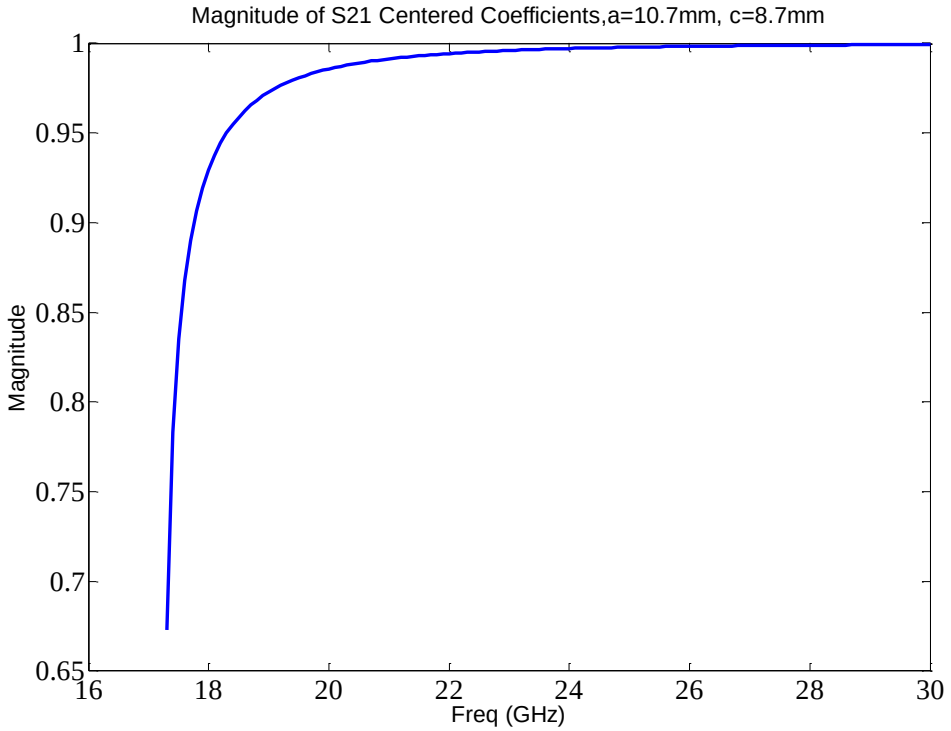

Figure 2.18 Magnitude of Transmission Coefficient (S_{21}) for a Double Step Waveguide Discontinuity Junction with Region A height 10.7mm and Region B height of 8.7mm

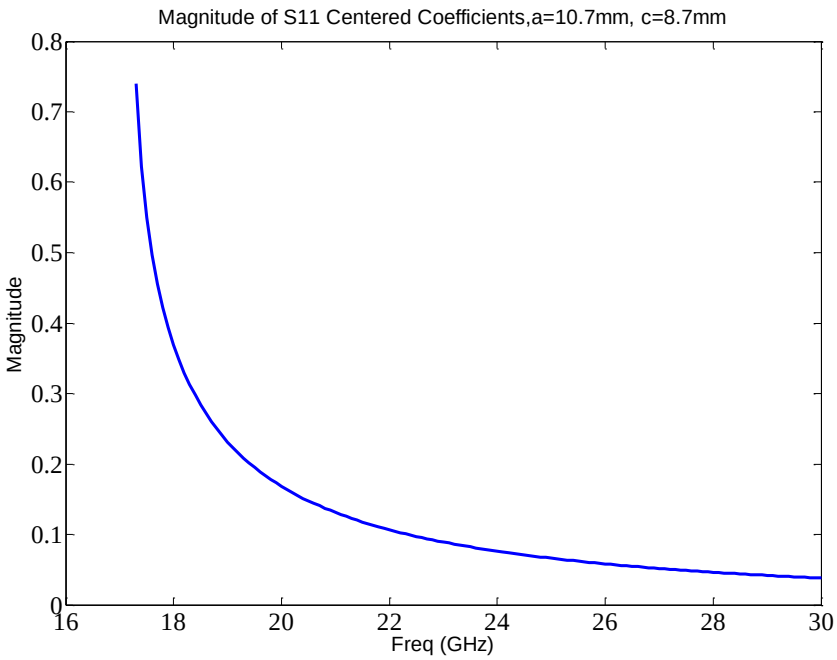

Figure 2.19 Magnitude of Reflection Coefficient (S_{11}) for a Double Step Waveguide Discontinuity Junction with Region A height 10.7mm and Region B height of 8.7mm

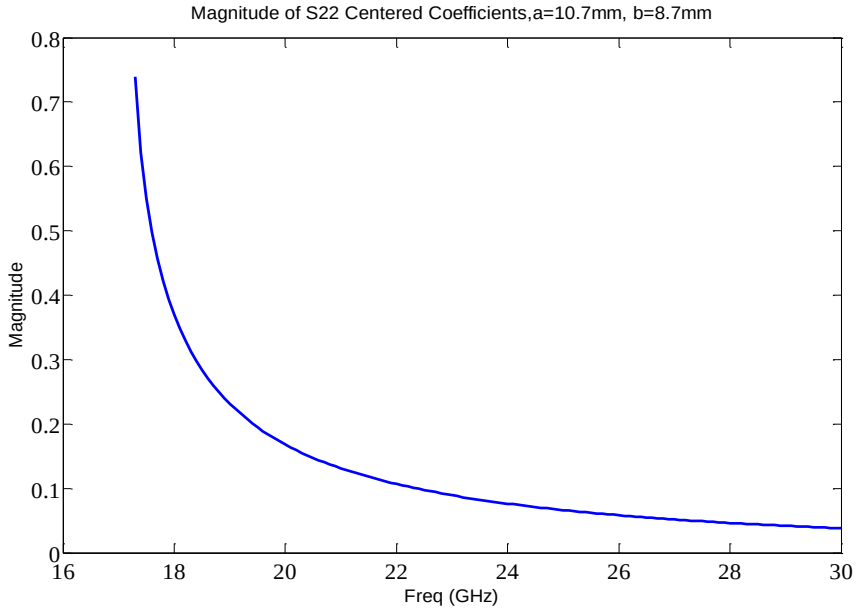

Figure 2.20 Magnitude of Reflection Coefficient (S_{22}) for a Double Step Waveguide Discontinuity Junction with Region A height 10.7mm and Region B height of 8.7mm.

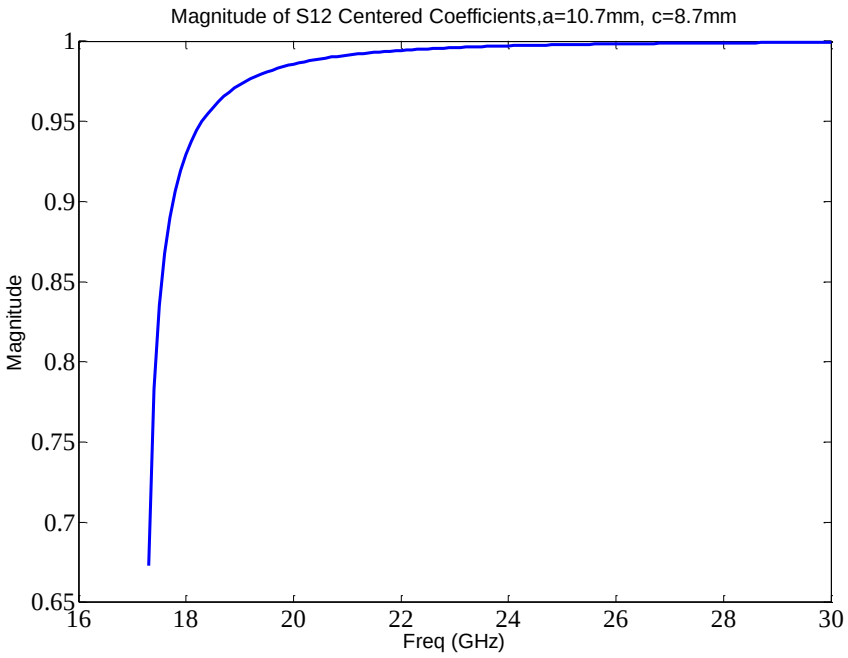

Figure 2.21 Magnitude of Transmission Coefficient (S_{12}) for a Double Step Waveguide Discontinuity Junction with Region A height 10.7mm and Region B height of 8.7mm.

2.7.2 Mode-Matching vs. Commercial FEM Results for Double Step Discontinuity

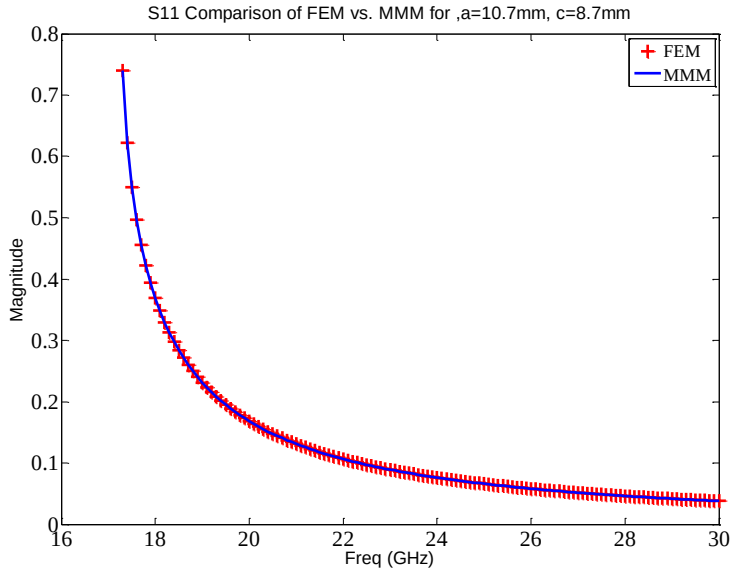

Figure 2.22 Reflection Coefficient (S_{11}) of Centered Double Step Waveguide Discontinuity of FEM vs. MMM Results

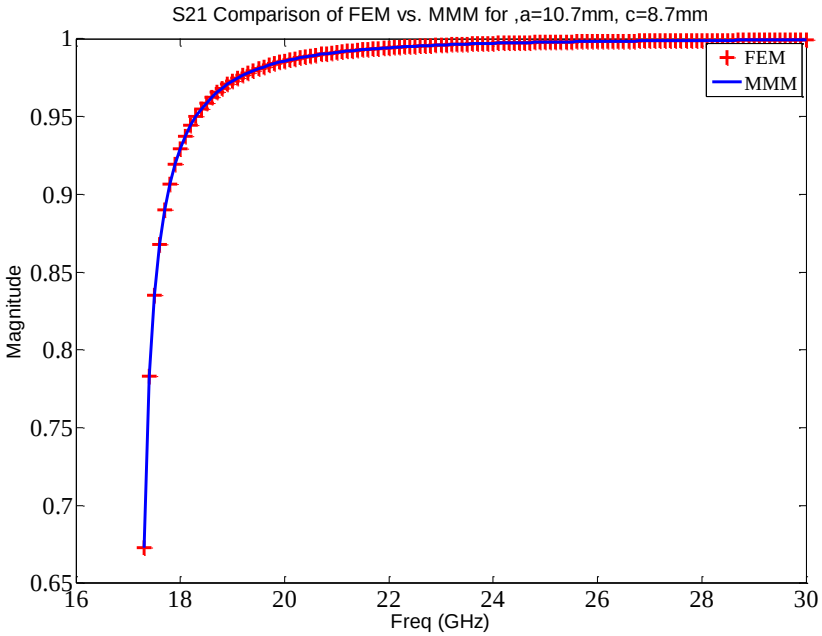

Figure 2.23 Transmission Coefficient (S_{21}) of Centered Double Step Waveguide Discontinuity of FEM vs. MMM Results

One can see a slight difference in the FEM vs. MMM. This undoubtedly results from two reasons. 1) There are slight numerical differences in the computational methods, 2) Commercial software is not capable of fully de-embedding to the plane z=0. This second source of error adds additional phase which distorts the magnitude component.

2.7.3 Phase of Waveguide Double Step Junction Discontinuity

Looking at Figure 2.24 and Figure 2.25 one notices that the phase of S_{21} still converges to zero after cutoff, while the phase of S_{11} varies linearly from $-\pi$ to π after cutoff as is typical in text. Again, there is no FEM vs. MMM comparison because of computational errors in the commercial FEM software in approximating zero thickness.

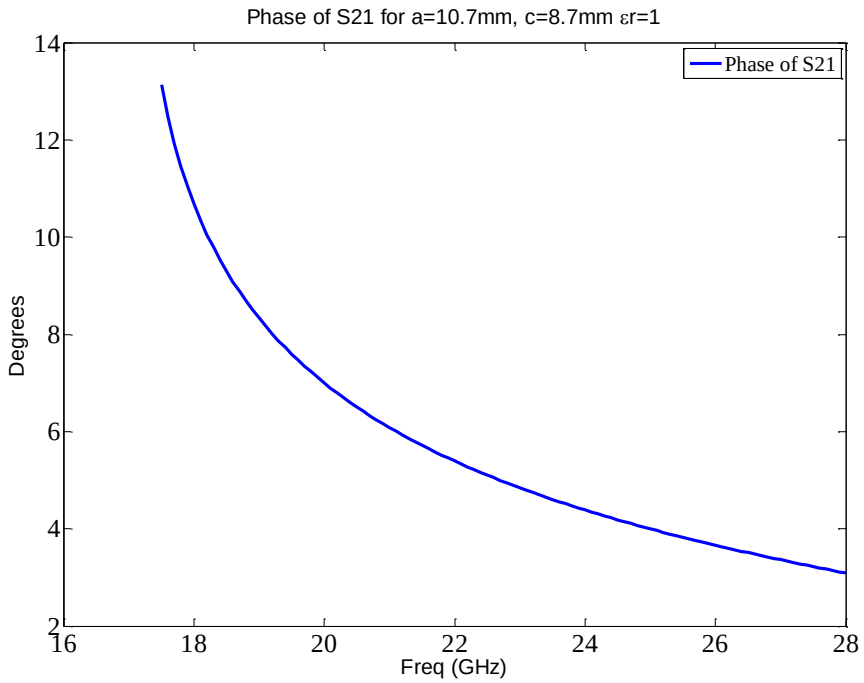

Figure 2.24 Transmission Coefficient Phase (S_{21}) of Centered Double Step Discontinuity

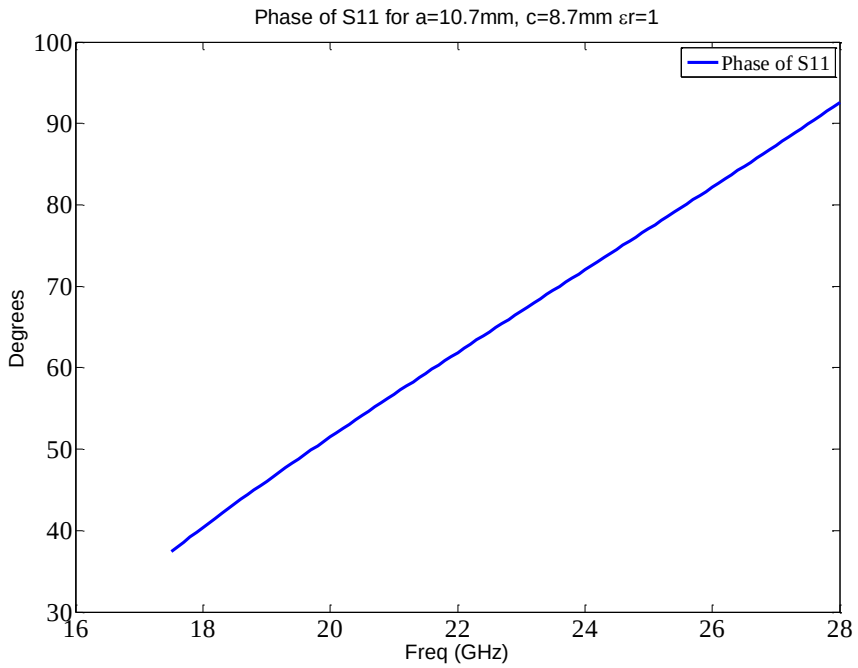

Figure 2.25 Reflection Coefficient Phase (S_{11}) of Centered Double Step Discontinuity

2.7.4 Coefficient Symmetry of Centered Step Discontinuity

Similar to section 2.6.3, the S-parameters of this system should be the same as the S-parameters of the same system, but with the dimensions of region A and B reversed as shown in Figure 2.26. In other words, $S_{21}^{A} = S_{12}^{B}$ and $S_{12}^{A} = S_{21}^{B}$. Figure 2.27 through Figure 2.28 contain the numerically computed results of such systems. The figures show very good agreement.

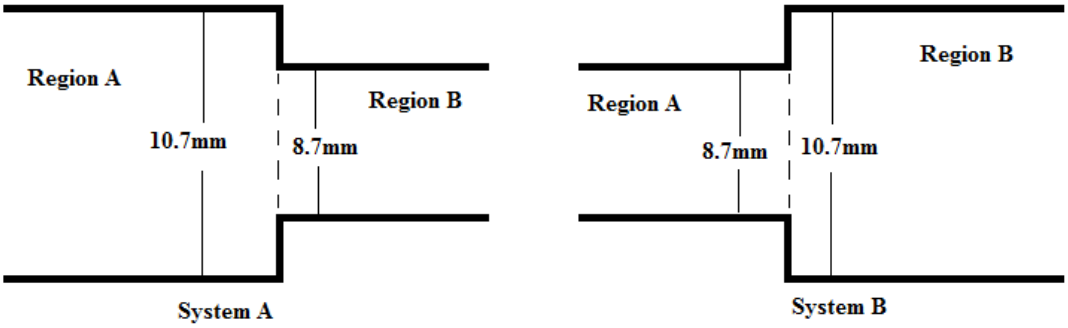

Figure 2.26 Symmetry of Centered Step Discontinuities System A and System B

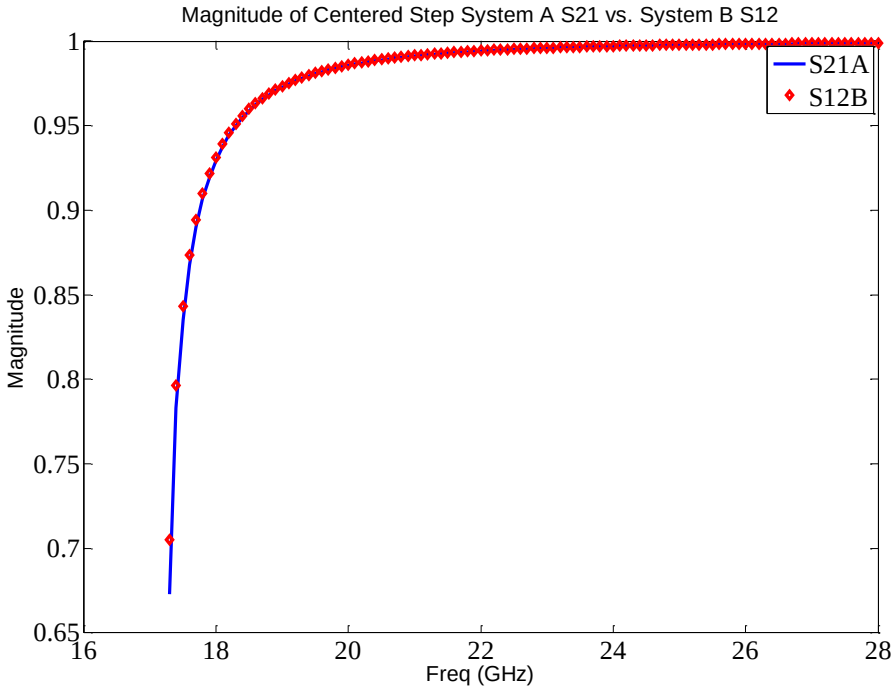

Figure 2.27 Magnitude Comparison of S_{21} from System A vs. S_{12} from System B when Step Discontinuity is Centered

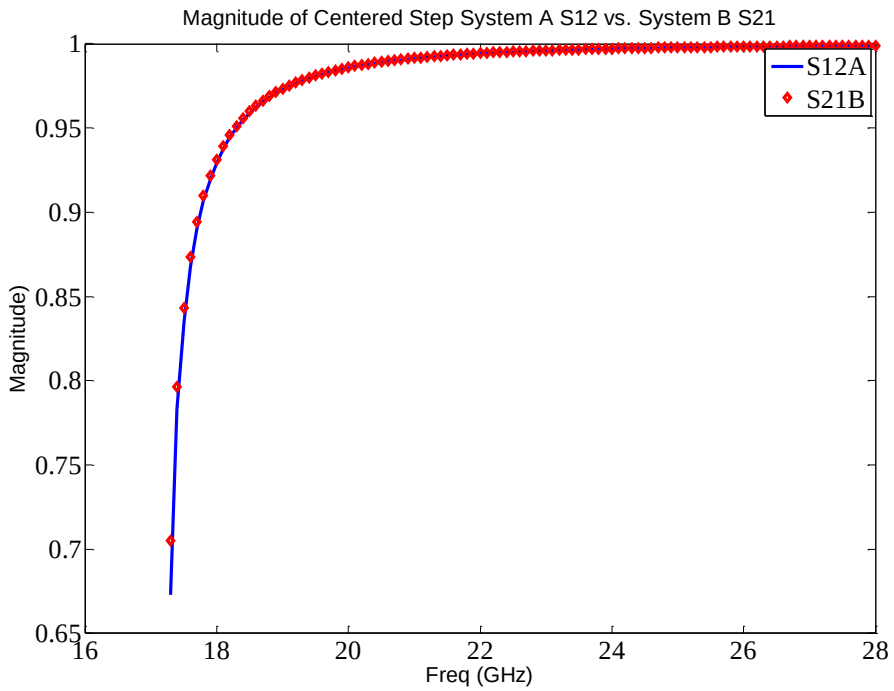

Figure 2.28 Magnitude Comparison of S_{12} from System A vs. S_{21} from System B when Step Discontinuity is Centered

3 Mode-Matching and Cascaded S-Parameter Theory

In [33-36] and in the textbooks [37-38], the theory behind cascading S-parameters from multistep systems is described. This research uses a somewhat simplified methodology to form these systems vs. the methodology of [33-37] by taking advantage of port extension theory. The following section describes this in detail.

3.1 Cascaded System Breakdown

By cascading multiple steps, as shown in Figure 3.1, it is possible to form filters. However, it is possible to decompose this multistep system in order to simplify analysis.

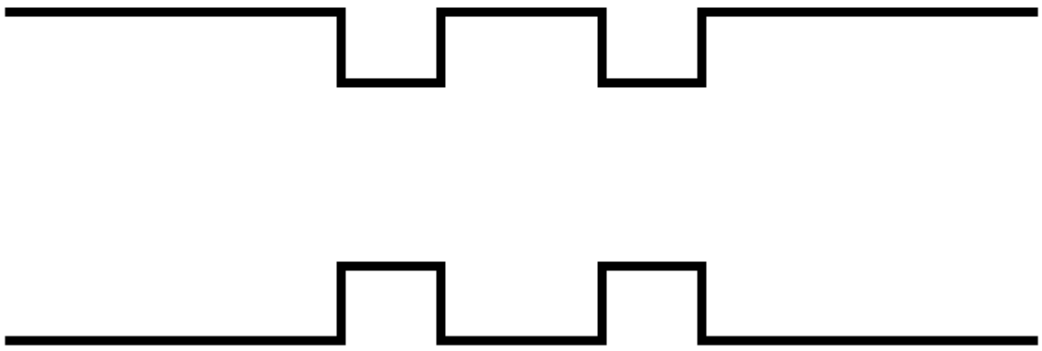

Figure 3.1 Example of Multiple Step System

By decomposing the multistep system into the cascade of step discontinuities and connecting transmission lines depicted in Figure 3.2 one can use mode-matching theory to analyze the step discontinuity to determine the S-parameters of each step. The S-parameters of the step discontinuities are then connected with corresponding transmission lines to form the system in Figure 3.1.

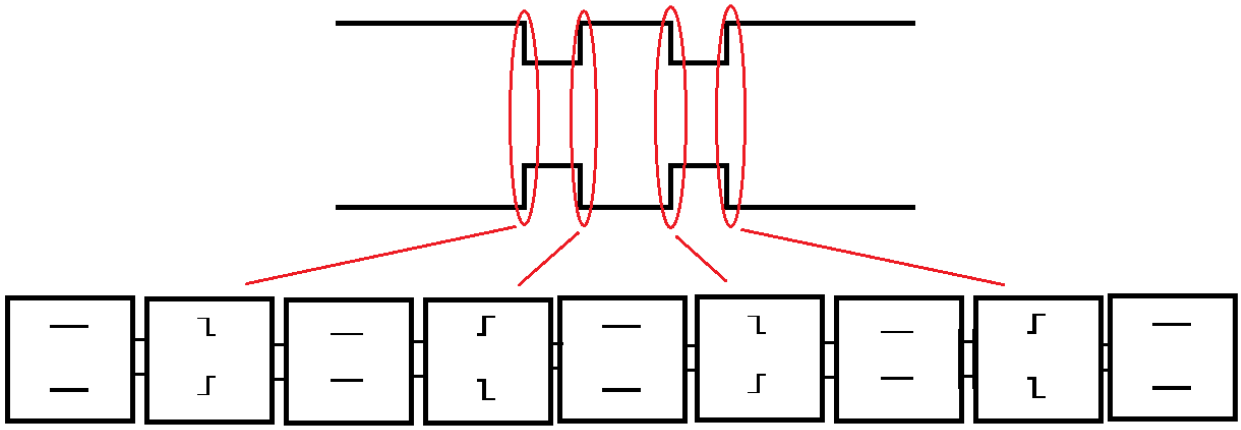

Figure 3.2 Multi-Step System Decomposition

By using the equations of sections 2.3.1−2.3.4, shown again below for convenience, the S-parameters for a given step discontinuity are calculated. With X,Y,Z,W used for avoidance of confusion.

$$X = \sum_{v=1}^{K}\left(\sum_{m=1}^{M}\left(\frac{2}{a}Y_{am}H_{mv}H_{mp}\right) + Y_{bv}\frac{c}{2}\delta_{vp}\right)^{-1}(2Y_{a1}H_{1v}) \text{ for } p = 1,2,\dots,K \quad 3.1$$

$$Y = \frac{2}{a}\sum_{p=1}^{K}\left(H_{mp}X(p)\right) - \delta_{m1} \text{ for } m = 1,2,\dots,M \quad 3.2$$

$$Z = \sum_{v=1}^{K}\left(\sum_{m=1}^{M}\left(\frac{2}{a}Y_{am}H_{mv}H_{mp}\right) + \delta_{vp}\frac{c}{2}Y_{bv}\right)^{-1}\left(\frac{c}{2}Y_{b1}\delta_{v1} - \sum_{m=1}^{M}\left(\frac{2}{a}Y_{am}H_{mv}H_{m1}\right)\right),$$

$$\text{for } p = 1,2,\dots,K \quad 3.3$$

$$W = \frac{2}{a}\sum_{p=1}^{K}\left(Z(p)H_{mp} + \delta_{p1}H_{m1}\right), \text{ for } m = 1,2,\dots,M \quad 3.4$$

In (3.1), $\left(\left(\sum_{m=1}^{M}\left(\frac{2}{a}Y_{am}H_{mv}H_{mp}\right) + Y_{bv}\frac{c}{2}\delta_{vp}\right)^{-1}\right)$ is not meant to be the reciprocal of the quantity enclosed in the parentheses. It is meant to be the $(pv)^{th}$ element of the inverse of the matrix whose $(vp)^{th}$ element is the quantity enclosed in the parentheses. The inverse quantity in (3.3) has a similar meaning. Using (3.1)−(3.4) the analogy of (3.5) is formed where *f* is the frequency for the corresponding S-parameter.

$$[S(f)] = \begin{bmatrix} Y(f) & W(f) \\ X(f) & Z(f) \end{bmatrix} = \begin{bmatrix} S_{11}(f) & S_{12}(f) \\ S_{21}(f) & S_{22}(f) \end{bmatrix} \quad 3.5$$

Similar to [33], transmission lines of length *l* may be added to each side of the waveguide step discontinuity if the S-parameters are premultiplied by a transmission matrix defined by

$$T = \begin{bmatrix} e^{\gamma_m l} & 0 \\ 0 & e^{-\gamma_m l} \end{bmatrix} \quad 3.6$$

where

$$\gamma_m = j\sqrt{k^2 - \left(\left(\frac{m\pi}{t}\right)^2\right)} \quad 3.7$$

and k is the free space wave number, *t* is the height of the connection waveguide, m is the mth mode present in the waveguide, and *l* is the length of the connecting waveguide. Equations (3.1−3.7) now define each decomposed section of Figure 3.2. Since S-parameters are not like ABCD parameters they cannot simply be multiplied to provide the response of the overall system. In order to account for the effects of later discontinuities at the input one must begin with the right-most S-parameters, and then back calculate. For example, in order to account for the effects of the transmission line on the step discontinuity the transmission line S-parameters are first calculated, and then the step discontinuity is added. This is depicted by arrow 1 in Figure 3.3. This process is then repeated from arrow 1 to arrow 8 in order to define the full system.

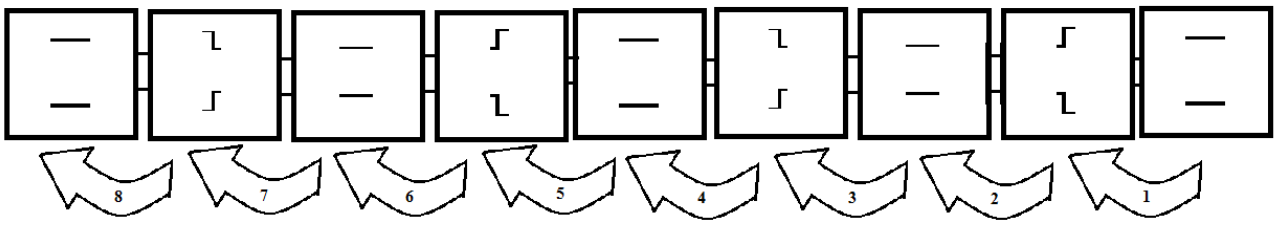

Figure 3.3 Calculation Methodology of Cascaded Decomposed S-parameter Blocks

3.2 Simplified System Decomposition

The methodology of 3.1 and Figure 3.3 provide the correct answer to the original system of Figure 3.1; however, as the number of discontinuities increases this method can become computationally time consuming. In order to reduce some of this computational effort, port extension theory described by Pozar [37] and Collin [38] is used.

3.2.1 Port Extension Theory Background

Say for example it is desired to extend the ports reference plane from z=0 to z=l_N, where l_N is an arbitrary length corresponding to the port of interest as shown in Figure 3.4

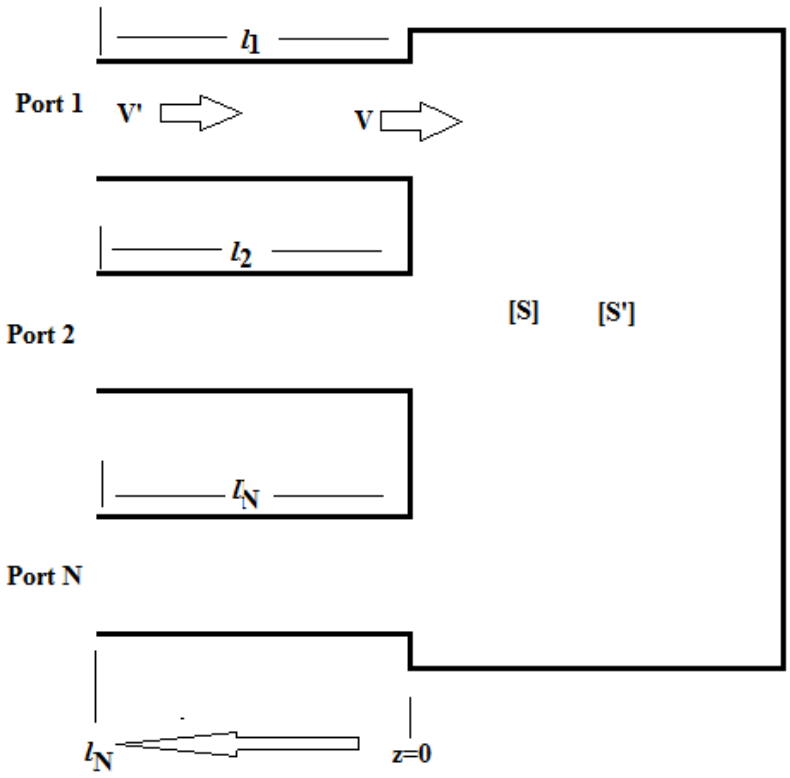

Figure 3.4 Port Extension

Assume V represents the total wave at reference plane z=0 in Figure 3.4. V is composed of a forward traveling voltage wave V^- and a backward traveling wave V^+. V^- travels in the minus z-direction and enters the [S] system at z=0. V^+ travels in the z-direction and exits the [S] system at z=0.Following Pozar's [37, p. 180] method these traveling waves represent the S-parameters of the original system given by eq. (3.8).

$$[V^+] = [S][V^-] \qquad 3.8$$

If the reference plane is now extended by some arbitrary distance l_N, as shown in Figure 3.4, let V' represent the total wave at this new reference plane. V' is composed of a forward traveling voltage wave V'^- and a backward traveling wave V'^+. The S-parameters of this new system are defined as

$$[V'^{+}] = [S'][V'^{-}] \tag{3.9}$$

Where S' is the S-parameters of the new system. The new wave amplitudes are related to the old wave amplitudes with the following relations

$$V_m'^{-} = V_m^{-} e^{\gamma_m l_m} \tag{3.10}$$

$$V_m'^{+} = V_m^{+} e^{-\gamma_m l_m} \tag{3.11}$$

where

$$\gamma_m = j\sqrt{k^2 - \left(\left(\frac{m\pi}{a_m}\right)^2\right)} \tag{3.12}$$

Equation (3.8) is now rewritten as

$$\begin{bmatrix} e^{\gamma_1 l_1} & \cdots & 0 \\ \vdots & \ddots & \vdots \\ 0 & \cdots & e^{\gamma_m l_m} \end{bmatrix} [V_m'^{+}] = [S] \begin{bmatrix} e^{-\gamma_1 l_1} & \cdots & 0 \\ \vdots & \ddots & \vdots \\ 0 & \cdots & e^{-\gamma_m l_m} \end{bmatrix} [V_m'^{-}] \tag{3.13}$$

Equation (3.13) solves for the S-parameters of the system with extended port reference planes in terms of the original system's S-parameters. This solution is $[V_m'^{+}] = [S'][V_m'^{-}]$ where

$$[S'] = \begin{bmatrix} e^{-\gamma_1 l_1} & \cdots & 0 \\ \vdots & \ddots & \vdots \\ 0 & \cdots & e^{-\gamma_m l_m} \end{bmatrix} [S] \begin{bmatrix} e^{-\gamma_1 l_1} & \cdots & 0 \\ \vdots & \ddots & \vdots \\ 0 & \cdots & e^{-\gamma_m l_m} \end{bmatrix} \tag{3.14}$$

3.2.2 Port Extension of a Step Discontinuity

Take, for example, one section of a system of discontinuities as shown in the red box of Figure 3.5. Using equations (3.1)–(3.5) the S-parameters of the discontinuity are calculated. The S-parameters of the discontinuity and the addition of connecting waveguide are easily provided by eq. (3.15), which is eq. (3.14) with the proper values substituted in.

$$[S'] = \begin{bmatrix} e^{\gamma_{am} l_1} & 0 \\ 0 & e^{\gamma_{bm} l_2/2} \end{bmatrix} [S] \begin{bmatrix} e^{\gamma_{am} l_1} & 0 \\ 0 & e^{\gamma_{bm} l_2/2} \end{bmatrix} \tag{3.15}$$

Where γ_{am} is the propagation constant of the mth mode in region A, and γ_{bm} is the propagation constant of the mth mode in region B.

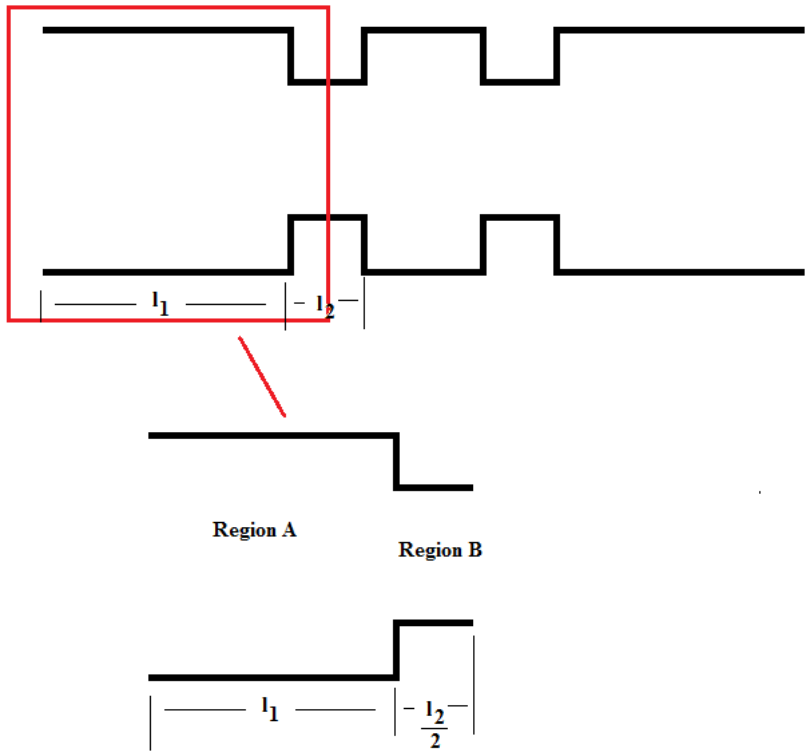

Figure 3.5 Decomposition using Port Extension.

3.2.2.1 Numerical Verification of Port Extension

To verify that the port extension theory works, the Mode-Matching method is used to calculate the S-parameters of the step discontinuity in Figure 3.6, then port extension theory of eq. (3.15) is used, and the results are compared to FEM results. Looking at Figure 3.7 through Figure 3.10 the MMM provides results that agree well with FEM results.

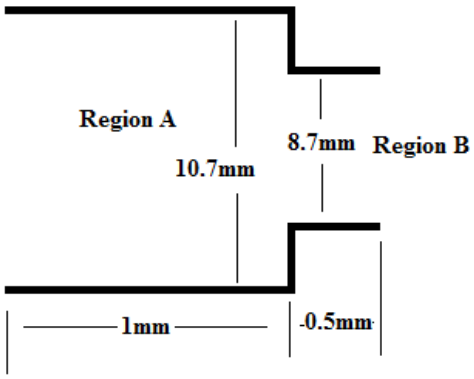

Figure 3.6 Dimensions for Port Extension Example

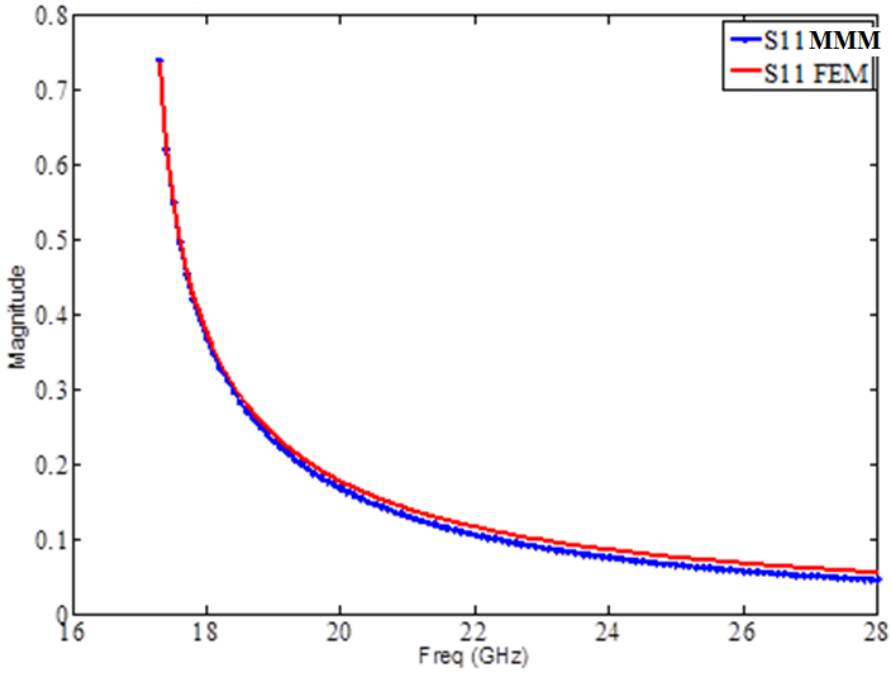

Figure 3.7 Comparison of S_{11} Coefficients of Centered Discontinuity for MMM vs. FEM Results. a=10.7mm, c=8.7mm.

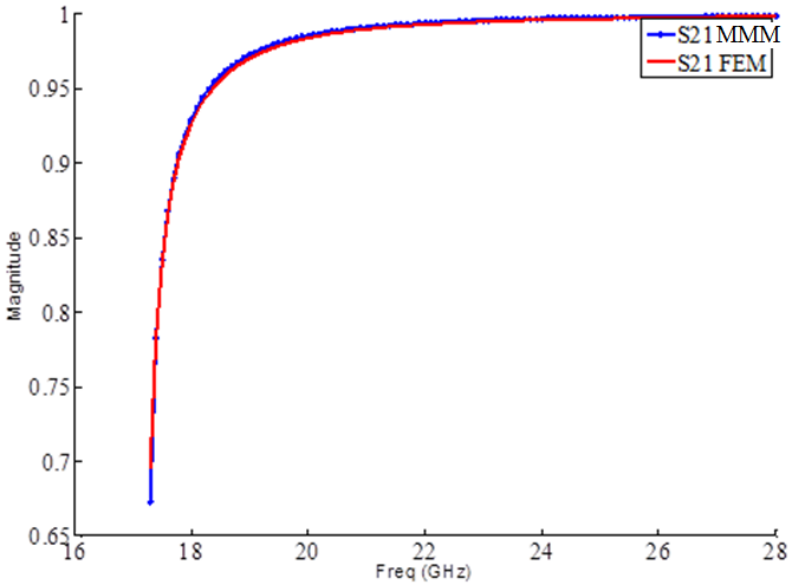

Figure 3.8 Comparison of S_{21} Coefficients of Centered Discontinuity for MMM vs. FEM Results. a=10.7mm, c=8.7mm

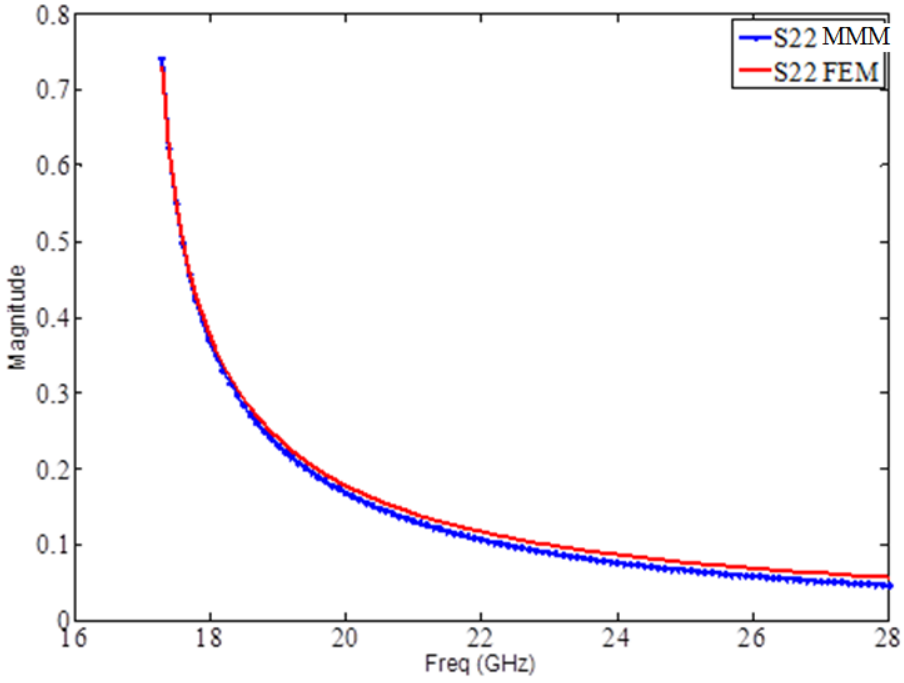

Figure 3.9 Comparison of S_{22} Coefficients of Centered Discontinuity for MMM vs. FEM Results. a=10.7mm, c=8.7mm

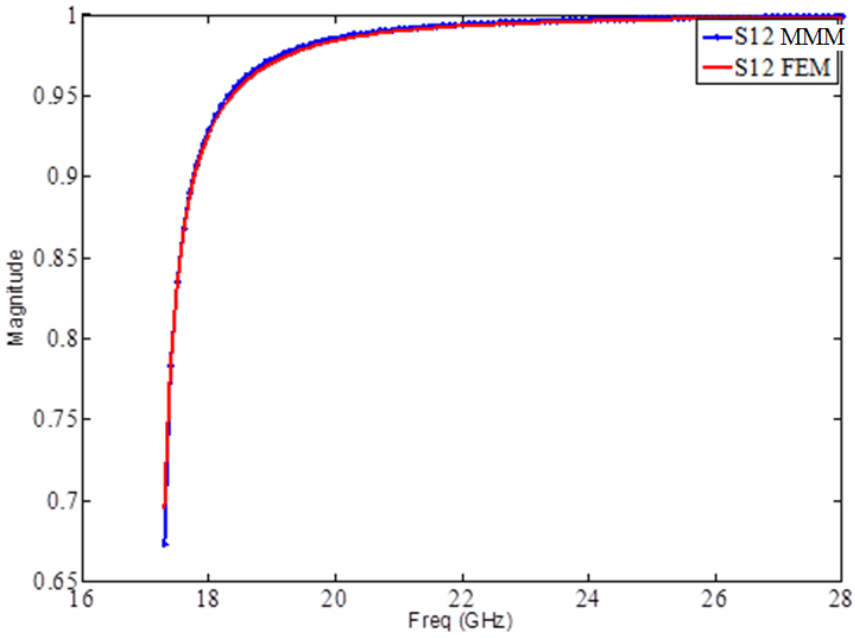

Figure 3.10 Comparison of S_{12} Coefficients of Centered Discontinuity for MMM vs. FEM Results. a=10.7mm, c=8.7mm

3.3 Cascaded System Using S-Parameter Theory

Looking at Figure 3.11, which is a system that consists of two centered step discontinuities and connecting transmission lines, one notices that the system can be decomposed into two sub-systems as depicted by the white arrows. Using the described mode matching methods and port extension theory described earlier one can determine the S-parameters for the step discontinuity and connecting transmission waveguides. The left and right hand side sub-systems have the S-Parameters $[S^A]$ and $[S^B]$ respectively.

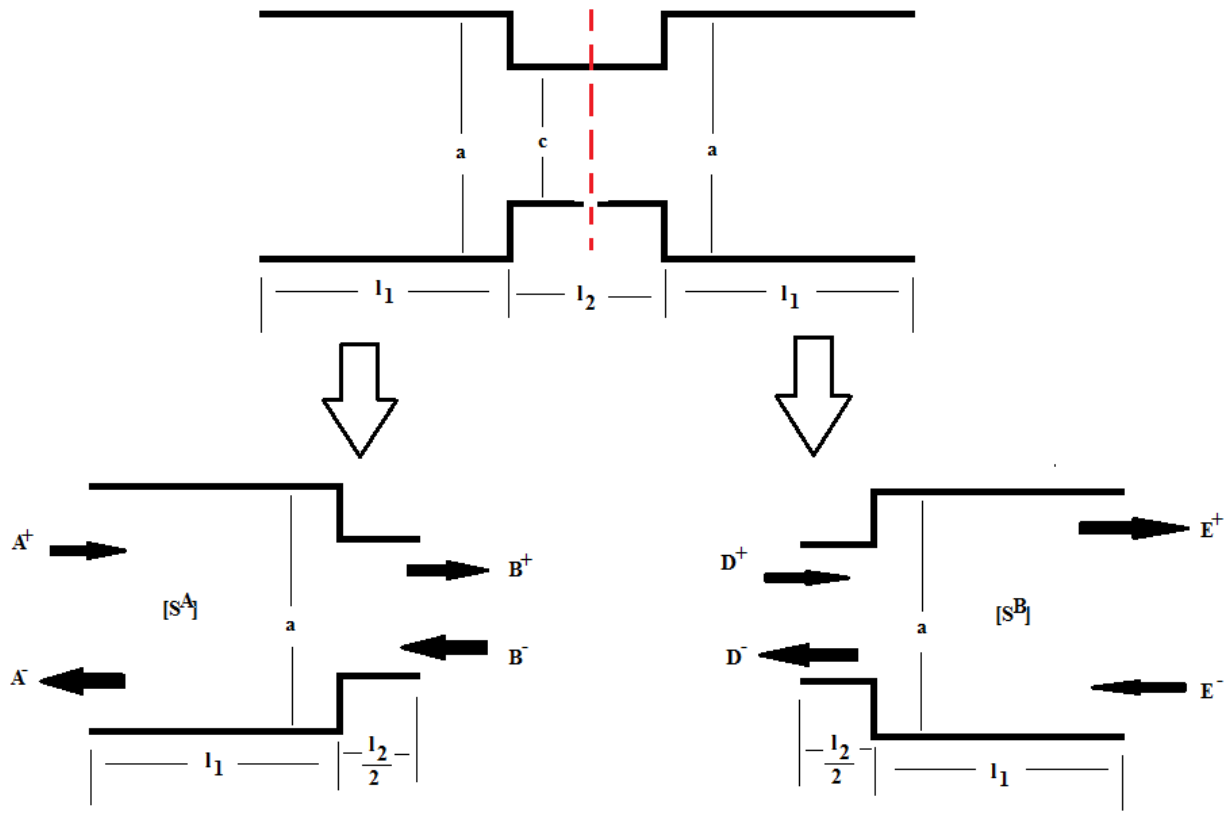

Figure 3.11 Decomposition of System Using Port Extension Theory

3.3.1 Cascading S-Parameter Theory

For each sub-system in Figure 3.11 the individual S-parameters are written in terms of the black arrows

$$[S^A]\begin{bmatrix}A^+\\B^-\end{bmatrix} = \begin{matrix}A^- = A^+S_{11}^A + B^-S_{12}^A\\B^+ = A^+S_{21}^A + B^-S_{22}^A\end{matrix} \quad 3.16$$

$$[S^B]\begin{bmatrix}D^+\\E^-\end{bmatrix} = \begin{matrix}D^- = D^+S_{11}^B + E^-S_{12}^B\\E^+ = D^+S_{21}^B + E^-S_{22}^B\end{matrix} \quad 3.17$$

And the S-parameters of the overall system written in terms of black arrows are

$$[S^T]\begin{bmatrix}A^+\\E^-\end{bmatrix} = \begin{matrix}A^- = A^+S_{11}^T + E^-S_{12}^T\\E^+ = A^+S_{21}^T + E^-S_{22}^T\end{matrix} \quad 3.18$$

Making the substitutions of $D^+ = B^+$ and $B^- = D^-$ allows for (3.16-3.17) to be rewritten as follows

$$A^- = A^+S_{11}^A + D^-S_{12}^A \quad 3.19$$

$$B^+ = A^+S_{21}^A + D^-S_{22}^A \quad 3.20$$

$$D^- = B^+S_{11}^B + E^-S_{12}^B \quad 3.21$$

$$E^+ = B^+S_{21}^B + E^-S_{22}^B \quad 3.22$$

By putting (3.21) into (3.20) yields

$$B^+ = A^+S_{21}^A + (B^+S_{11}^B + E^-S_{12}^B)S_{22}^A \quad 3.23$$

After grouping

$$B^+ = \frac{S_{21}^A A^+}{(1-S_{22}^A S_{11}^B)} + \frac{S_{22}^A S_{12}^B E^-}{(1-S_{22}^A S_{11}^B)} \quad 3.24$$

Replacing B^+ in (3.21) with (3.24) and grouping like terms results in

$$D^- = \left(\frac{S_{11}^B S_{21}^A A^+}{(1-S_{22}^A S_{11}^B)}\right) + E^-\left(S_{12}^B + \frac{S_{11}^B S_{22}^A S_{12}^B}{(1-S_{22}^A S_{11}^B)}\right) \quad 3.25$$

Substituting (3.25) into (3.19) and after regrouping gives the first equation in (3.18)

$$A^- = \left(S_{11}^A + \left(\frac{S_{12}^A S_{11}^B S_{21}^A}{(1-S_{22}^A S_{11}^B)}\right)\right)A^+ + \left(S_{12}^B S_{12}^A + \frac{S_{12}^A S_{11}^B S_{22}^A S_{12}^B}{(1-S_{22}^A S_{11}^B)}\right)E^- \quad 3.26$$

Taking (3.24) and now replacing B^+ in (3.22) gives

$$E^+ = \left(\frac{S_{21}^A A^+}{(1-S_{22}^A S_{11}^B)} + \frac{S_{22}^A S_{12}^B E^-}{(1-S_{22}^A S_{11}^B)}\right)S_{21}^B + E^-S_{22}^B \quad 3.27$$

After regrouping gives (3.28), which is the second equation in (3.18)

$$E^+ = \frac{S_{21}^B S_{21}^A A^+}{(1-S_{22}^A S_{11}^B)} + \left(\frac{S_{21}^B S_{22}^A S_{12}^B}{(1-S_{22}^A S_{11}^B)} + S_{22}^B\right)E^- \quad 3.28$$

The S-parameters of the overall system shown in Figure 3.11 are now defined as follows

$$S_{11}^{T} = S_{11}^{A} + \left(\frac{S_{12}^{A} S_{11}^{B} S_{21}^{A}}{(1 - S_{22}^{A} S_{11}^{B})}\right) \quad 3.29$$

$$S_{21}^{T} = \frac{S_{21}^{B} S_{21}^{A}}{(1 - S_{22}^{A} S_{11}^{B})} \quad 3.30$$

$$S_{12}^{T} = \frac{S_{12}^{B} S_{12}^{A}}{(1 - S_{22}^{A} S_{11}^{B})} \quad 3.31$$

$$S_{22}^{T} = \frac{S_{21}^{B} S_{22}^{A} S_{12}^{B}}{(1 - S_{22}^{A} S_{11}^{B})} + S_{22}^{B} \quad 3.32$$

This method can be used to solve for multiple discontinuities. By using the port extension theory where the elements of the scattering matrix are of the form (3.29)−(3.32), the eight scattering matrices in Figure 3.3, one for each arrow in Figure 3.3, can be reduced to two scattering matrices each of whose elements are of the form (3.29)−(3.32). The first of these two scattering matrices consists of arrows 1 to 4 in Figure 3.3 and the second of these scattering matrices consists of arrows 5 to 8 in Figure 3.3. It is clear the numerical efficiency port extension theory brings.

3.3.2 Numerical Results of Cascaded System

Using Figure 3.11 as a reference, Figure 3.12-Figure 3.15 compare MMM results with FEM results for a=10.7mm, c=9.7mm, l_1=15mm, and l_2=15mm. It is shown that the results agree.

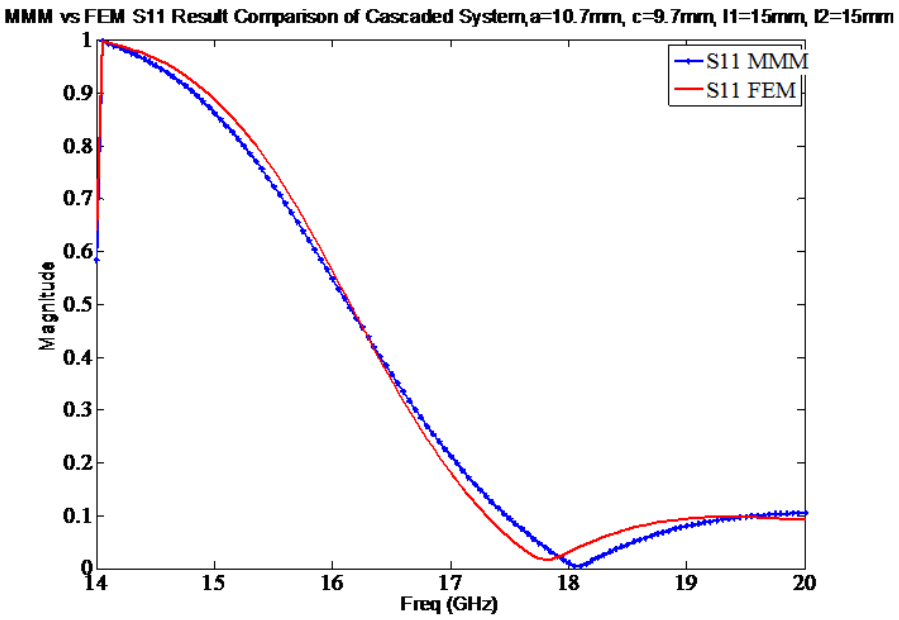

Figure 3.12 MMM vs. FEM S_{11} for Cascaded System, a=10.7mm,c=9.7mm,l_1=15mm,l_2=15mm

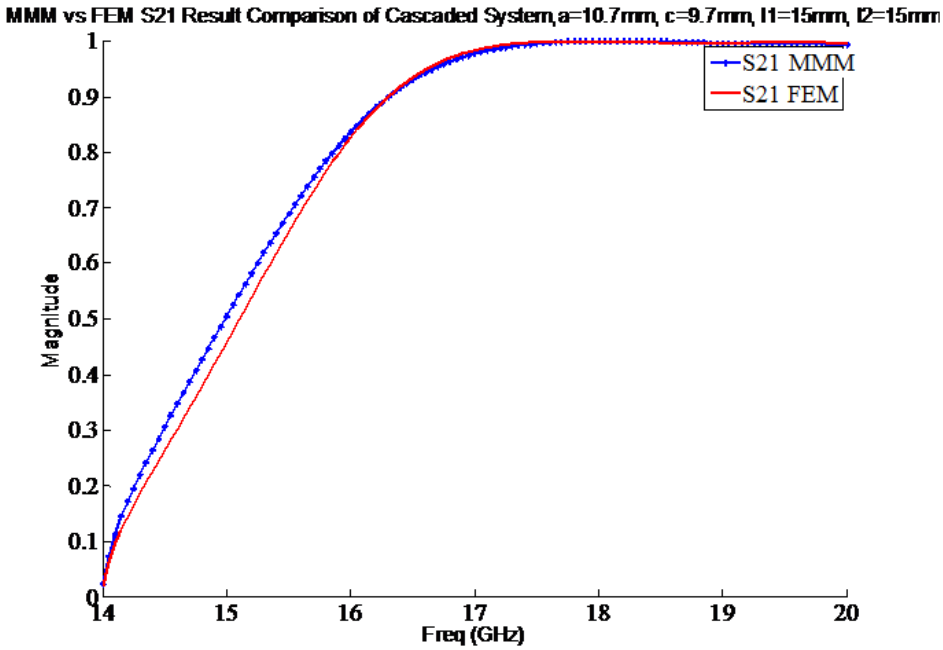

Figure 3.13 MMM vs. FEM S_{21} for Cascaded System, a=10.7mm,c=9.7mm,l_1=15mm,l_2=15mm

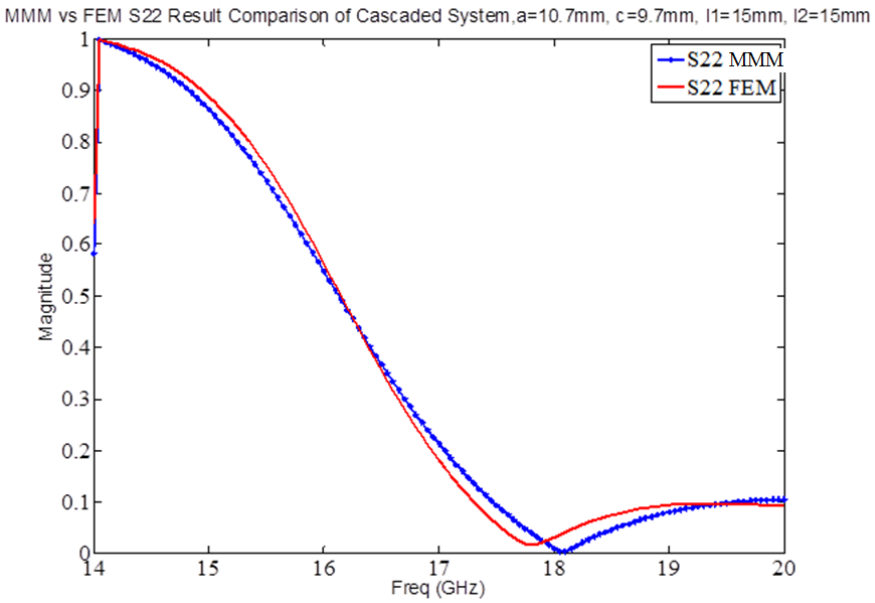

Figure 3.14 MMM vs. FEM S_{22} for Cascaded System, a=10.7mm,c=9.7mm,l_1=15mm,l_2=15mm

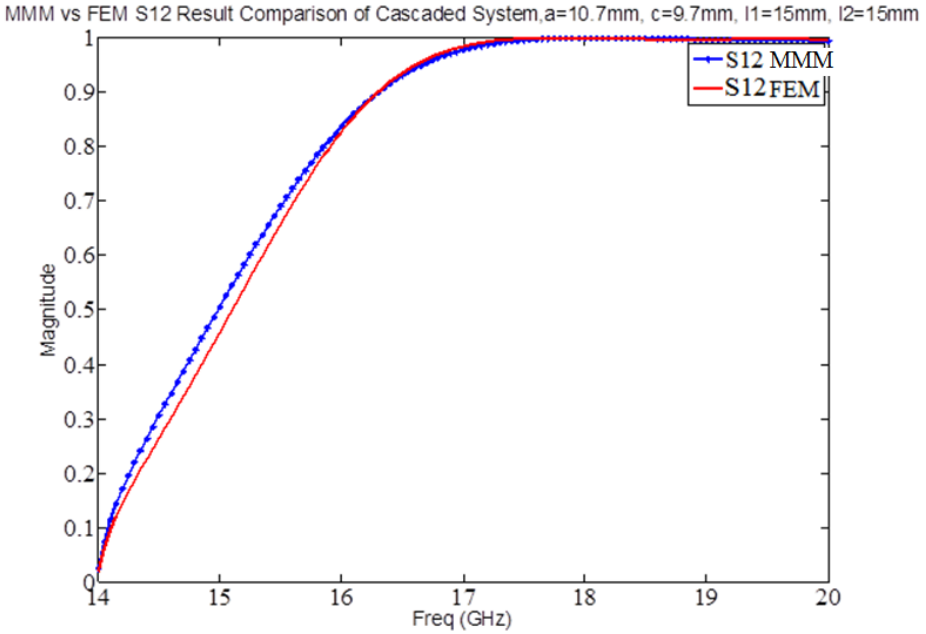

Figure 3.15 MMM vs. FEM S_{12} for Cascaded System, a=10.7mm,c=9.7mm,l_1=15mm,l_2=15mm

4 Step Discontinuities Filled with Uniaxial Media

As mentioned, in Section 1.2, there is work regarding media filled waveguides with and without optic axis rotation [22]−[25]. However, to the best of our knowledge this is the first research that uses the Mode-Matching Method (MMM) to solve for reflection and transmission coefficients of various waveguide step discontinuities filled with uniaxial media.

4.1 Rotation Matrices

Before dispersion relations in uniaxial media are derived mathematical formulation of rotation matrices is explained. Rotation of the optic axis is important because looking at Figure 4.1 one can see that the coordinate system of the media does not necessarily coincide with the analysis coordinate system of the waveguide.

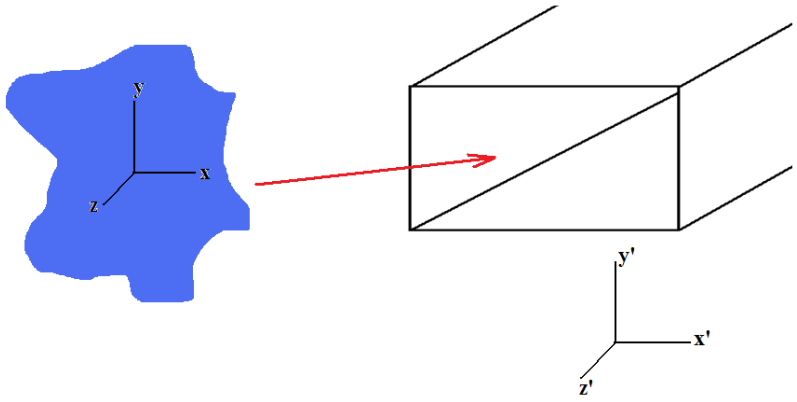

Figure 4.1 Uniaxial and waveguide coordinate systems

The theory used here is the same as that in [45]−[46], but expanded on. This theory allows the optic axis to be arbitrarily rotated with respect to the z-axis of the laboratory coordinate

system. Assume for generality the displacement vector D for a Cartesian coordinate system is given by

$$\begin{bmatrix} D\cdot\hat{x}''' \\ D\cdot\hat{y}''' \\ D\cdot\hat{z}''' \end{bmatrix} = \varepsilon_0 \begin{bmatrix} \varepsilon_x & 0 & 0 \\ 0 & \varepsilon_y & 0 \\ 0 & 0 & \varepsilon_z \end{bmatrix} \begin{bmatrix} E\cdot\hat{x}''' \\ E\cdot\hat{y}''' \\ E\cdot\hat{z}''' \end{bmatrix} \quad 4.1$$

where $\hat{x}'''$, $\hat{y}'''$, $\hat{z}'''$ are respectively the unit vectors in the x’’’, y’’’, and z’’’ directions of what is called the experimental coordinate system. Through a series of three rotations we wish to express the experimental coordinate system in terms of the laboratory system. First, assume an observer is looking in the minus z-direction of the (x’’’,y’’’,z’’’) coordinate system and wishes to rotate the system by a counterclockwise rotation of α about the z’’’-axis of the original (x’’’,y’’’,z’’’) coordinate system as shown in Figure 4.2. This forms a new coordinate system (x’’,y’’,z’’).

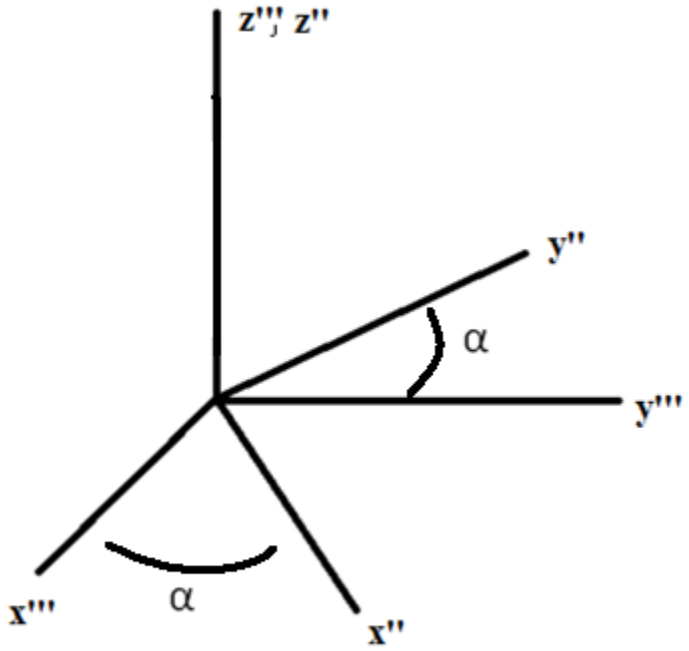

Figure 4.2 Rotation about the z’’’-axis by angle α

The unit vectors in the (x'',y'',z'') system depend on the unit vectors in the original (x''', y''', z''') system through the relation

$$\begin{bmatrix}\hat{x}''\\ \hat{y}''\\ \hat{z}''\end{bmatrix}=\begin{bmatrix}\cos\alpha & \sin\alpha & 0\\ -\sin\alpha & \cos\alpha & 0\\ 0 & 0 & 1\end{bmatrix}\begin{bmatrix}\hat{x}'''\\ \hat{y}'''\\ \hat{z}'''\end{bmatrix} \quad 4.2$$

where $(\hat{x}'', \hat{y}'', \hat{z}'')$ are the unit vectors in the (x'',y'',z'') system and $(\hat{x}''', \hat{y}''', \hat{z}''')$ are the unit vectors in the (x''',y''',z''') coordinate system. Premultiplying (4.2) by the inverse of the rotation matrix gives

$$\begin{bmatrix}\hat{x}'''\\ \hat{y}'''\\ \hat{z}'''\end{bmatrix}=\begin{bmatrix}\cos\alpha & -\sin\alpha & 0\\ \sin\alpha & \cos\alpha & 0\\ 0 & 0 & 1\end{bmatrix}\begin{bmatrix}\hat{x}''\\ \hat{y}''\\ \hat{z}''\end{bmatrix}. \quad 4.3$$

Substituting (4.3) into (4.1),

$$\begin{bmatrix}\cos\alpha & -\sin\alpha & 0\\ \sin\alpha & \cos\alpha & 0\\ 0 & 0 & 1\end{bmatrix}\begin{bmatrix}\hat{x}''\\ \hat{y}''\\ \hat{z}''\end{bmatrix}\cdot D=\varepsilon_0\begin{bmatrix}\varepsilon_x & 0 & 0\\ 0 & \varepsilon_y & 0\\ 0 & 0 & \varepsilon_z\end{bmatrix}\begin{bmatrix}\cos\alpha & -\sin\alpha & 0\\ \sin\alpha & \cos\alpha & 0\\ 0 & 0 & 1\end{bmatrix}\begin{bmatrix}\hat{x}''\\ \hat{y}''\\ \hat{z}''\end{bmatrix}\cdot E, \quad 4.4$$

where for $\bar{C}$=$\overline{D}$ or $\bar{C}$=$\bar{E}$

$$\begin{bmatrix}\hat{x}''\\ \hat{y}''\\ \hat{z}''\end{bmatrix}\cdot\bar{C}=\begin{bmatrix}C\cdot\hat{x}''\\ C\cdot\hat{y}''\\ C\cdot\hat{z}''\end{bmatrix}. \quad 4.5$$

Premultiplying both sides of (4.4) with the rotation matrix in (4.2) gives

$$\begin{bmatrix}\hat{x}''\\ \hat{y}''\\ \hat{z}''\end{bmatrix}\cdot\overline{D}=\varepsilon_0\begin{bmatrix}\cos\alpha & \sin\alpha & 0\\ -\sin\alpha & \cos\alpha & 0\\ 0 & 0 & 1\end{bmatrix}\begin{bmatrix}\varepsilon_x & 0 & 0\\ 0 & \varepsilon_y & 0\\ 0 & 0 & \varepsilon_z\end{bmatrix}\begin{bmatrix}\cos\alpha & -\sin\alpha & 0\\ \sin\alpha & \cos\alpha & 0\\ 0 & 0 & 1\end{bmatrix}\begin{bmatrix}\hat{x}''\\ \hat{y}''\\ \hat{z}''\end{bmatrix}\cdot\bar{E}, \quad 4.6$$

and after multiplication gives

$$\begin{bmatrix}\hat{x}''\\ \hat{y}''\\ \hat{z}''\end{bmatrix}\cdot\overline{D}=\varepsilon_0\begin{bmatrix}\varepsilon_y\sin^2\alpha+\varepsilon_x\cos^2\alpha & (\varepsilon_y-\varepsilon_x)\sin\alpha\cos\alpha & 0\\ (\varepsilon_y-\varepsilon_x)\sin\alpha\cos\alpha & \varepsilon_x\sin^2\alpha+\varepsilon_y\cos^2\alpha & 0\\ 0 & 0 & \varepsilon_z\end{bmatrix}\begin{bmatrix}\hat{x}''\\ \hat{y}''\\ \hat{z}''\end{bmatrix}\cdot\bar{E}. \quad 4.7$$

Condensing (4.7) we get

$$\begin{bmatrix} \hat{x}'' \\ \hat{y}'' \\ \hat{z}'' \end{bmatrix} \cdot \bar{D} = \varepsilon_0 \begin{bmatrix} \varepsilon_{11}' & \varepsilon_{12}' & 0 \\ \varepsilon_{12}' & \varepsilon_{22}' & 0 \\ 0 & 0 & \varepsilon_{33}' \end{bmatrix} \begin{bmatrix} \hat{x}'' \\ \hat{y}'' \\ \hat{z}'' \end{bmatrix} \cdot \bar{E} \quad 4.8$$

where

$$\varepsilon_{11}' = \varepsilon_y \sin^2\alpha + \varepsilon_x \cos^2\alpha \quad 4.9$$

$$\varepsilon_{12}' = (\varepsilon_y - \varepsilon_x) \sin\alpha \cos\alpha \quad 4.10$$

$$\varepsilon_{22}' = \varepsilon_x \sin^2\alpha + \varepsilon_y \cos^2\alpha \quad 4.11$$

$$\varepsilon_{33}' = \varepsilon_z \quad 4.12$$

Now assume an observer is looking in the minus x''-direction of the new (x'',y'',z'') system, and wishes to rotate the coordinate system about the x''-axis clockwise by an angle of β forming a 2nd new coordinate system (x',y',z') as shown in Figure 4.3.

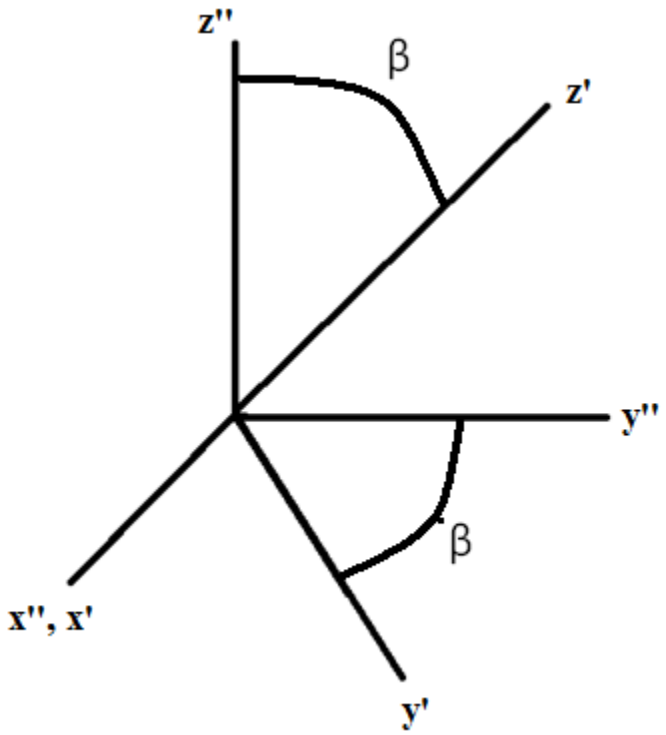

Figure 4.3 Rotation about the x''-axis by angle β

In the 2nd coordinate system the relation between the (x'',y'',z'') system and the (x',y',z') system is given by

$$\begin{bmatrix}\hat{x}'\\ \hat{y}'\\ \hat{z}'\end{bmatrix}=\begin{bmatrix}1 & 0 & 0\\ 0 & \cos\beta & -\sin\beta\\ 0 & \sin\beta & \cos\beta\end{bmatrix}\begin{bmatrix}\hat{x}''\\ \hat{y}''\\ \hat{z}''\end{bmatrix} \tag{4.13}$$

where $(\hat{x}', \hat{y}', \hat{z}')$ are the unit vectors of the (x',y',z') system, and $(\hat{x}'', \hat{y}'', \hat{z}'')$ are the unit vectors in the (x'',y'',z'') system. Premultiplying (4.13) by the inverse of the rotation matrix in (4.13) gives

$$\begin{bmatrix}\hat{x}''\\ \hat{y}''\\ \hat{z}''\end{bmatrix}=\begin{bmatrix}1 & 0 & 0\\ 0 & \cos\beta & \sin\beta\\ 0 & -\sin\beta & \cos\beta\end{bmatrix}\begin{bmatrix}\hat{x}'\\ \hat{y}'\\ \hat{z}'\end{bmatrix}, \tag{4.14}$$

and substituting (4.14) into (4.8) yields

$$\begin{bmatrix}1 & 0 & 0\\ 0 & \cos\beta & \sin\beta\\ 0 & -\sin\beta & \cos\beta\end{bmatrix}\begin{bmatrix}\hat{x}'\\ \hat{y}'\\ \hat{z}'\end{bmatrix}\cdot\bar{D}=\varepsilon_0\begin{bmatrix}\varepsilon_{11}' & \varepsilon_{12}' & 0\\ \varepsilon_{12}' & \varepsilon_{22}' & 0\\ 0 & 0 & \varepsilon_{33}'\end{bmatrix}\begin{bmatrix}1 & 0 & 0\\ 0 & \cos\beta & \sin\beta\\ 0 & -\sin\beta & \cos\beta\end{bmatrix}\begin{bmatrix}\hat{x}'\\ \hat{y}'\\ \hat{z}'\end{bmatrix}\cdot\bar{E}. \tag{4.15}$$

Premultiplication of both sides of (4.15) with the rotation matrix in (4.13) gives

$$\begin{bmatrix}\hat{x}'\\ \hat{y}'\\ \hat{z}'\end{bmatrix}\cdot\bar{D}=\varepsilon_0\begin{bmatrix}1 & 0 & 0\\ 0 & \cos\beta & -\sin\beta\\ 0 & \sin\beta & \cos\beta\end{bmatrix}\begin{bmatrix}\varepsilon_{11}' & \varepsilon_{12}' & 0\\ \varepsilon_{12}' & \varepsilon_{22}' & 0\\ 0 & 0 & \varepsilon_{33}'\end{bmatrix}\begin{bmatrix}1 & 0 & 0\\ 0 & \cos\beta & \sin\beta\\ 0 & -\sin\beta & \cos\beta\end{bmatrix}\begin{bmatrix}\hat{x}'\\ \hat{y}'\\ \hat{z}'\end{bmatrix}\cdot\bar{E}, \tag{4.16}$$

which after multiplication provides

$$\begin{bmatrix}\hat{x}'\\ \hat{y}'\\ \hat{z}'\end{bmatrix}\cdot\bar{D}=\varepsilon_0\begin{bmatrix}\varepsilon_{11}'' & \varepsilon_{12}'' & \varepsilon_{13}''\\ \varepsilon_{12}'' & \varepsilon_{22}'' & \varepsilon_{23}''\\ \varepsilon_{13}'' & \varepsilon_{23}'' & \varepsilon_{33}''\end{bmatrix}\begin{bmatrix}\hat{x}'\\ \hat{y}'\\ \hat{z}'\end{bmatrix}\cdot\bar{E}, \tag{4.17}$$

where

$$\varepsilon_{11}''=\varepsilon_y\sin^2\alpha+\varepsilon_x\cos^2\alpha \tag{4.18}$$

$$\varepsilon_{12}''=\left(\varepsilon_y-\varepsilon_x\right)\sin\alpha\cos\alpha\cos\beta \tag{4.19}$$

$$\varepsilon_{13}''=\left(\varepsilon_y-\varepsilon_x\right)\sin\alpha\cos\alpha\sin\beta \tag{4.20}$$

$$\varepsilon_{22}''=\varepsilon_z\sin^2\beta+\cos^2\beta\left(\varepsilon_x\sin^2\alpha+\varepsilon_y\cos^2\alpha\right) \tag{4.21}$$

$$\varepsilon_{23}^{''} = \cos\beta \sin\beta \left(\varepsilon_x \sin^2\alpha + \varepsilon_y \cos^2\alpha\right) - \varepsilon_z \sin\beta \cos\beta \quad 4.22$$

$$\varepsilon_{33}^{''} = \varepsilon_z \cos^2\beta + \sin^2\beta\left(\varepsilon_x \sin^2\alpha + \varepsilon_y \cos^2\alpha\right). \quad 4.23$$

Finally, looking at Figure 4.4 (similar to Figure 4.2) assume an observer is looking in the negative direction of the z' axis and wishes to rotate the (x',y',z') coordinate system about the z' axis counterclockwise, but this time by an angle of ψ forming the laboratory coordinate system (x, y, z).

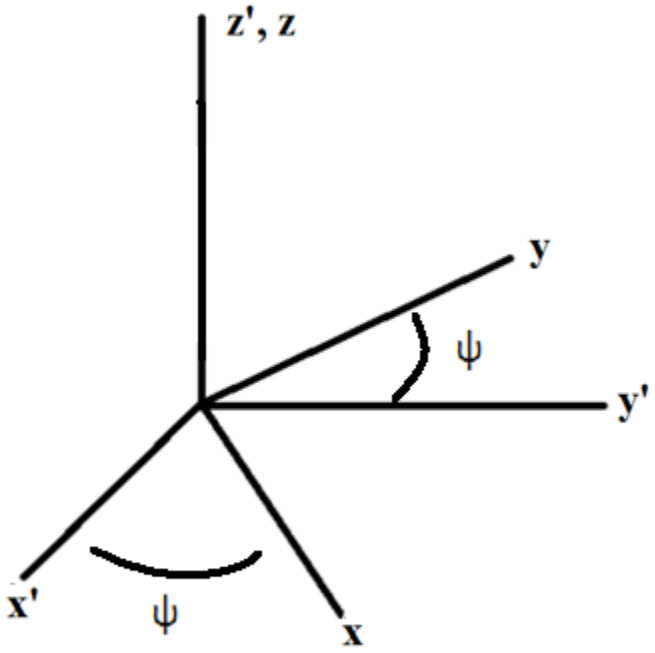

Figure 4.4 Rotation of the z' axis counterclockwise by an angle of ψ.

Therefore, the rotations in Figures 4.1−4.3 have transformed the experimental coordinate system into the laboratory coordinate system. The equation that expresses the (x,y,z) system in terms of the (x',y',z') coordinate system is

$$\begin{bmatrix}\hat{x}\\ \hat{y}\\ \hat{z}\end{bmatrix}=\begin{bmatrix}\cos\psi & \sin\psi & 0\\ -\sin\psi & \cos\psi & 0\\ 0 & 0 & 1\end{bmatrix}\begin{bmatrix}\hat{x}'\\ \hat{y}'\\ \hat{z}'\end{bmatrix} \tag{4.24}$$

Premultiplying both sides of (4.24) by the inverse of the rotation matrix in (4.24) yields

$$\begin{bmatrix}\hat{x}'\\ \hat{y}'\\ \hat{z}'\end{bmatrix}=\begin{bmatrix}\cos\psi & -\sin\psi & 0\\ \sin\psi & \cos\psi & 0\\ 0 & 0 & 1\end{bmatrix}\begin{bmatrix}\hat{x}\\ \hat{y}\\ \hat{z}\end{bmatrix}. \tag{4.25}$$

Substituting (4.25) into (4.17),

$$\begin{bmatrix}\cos\psi & -\sin\psi & 0\\ \sin\psi & \cos\psi & 0\\ 0 & 0 & 1\end{bmatrix}\begin{bmatrix}\hat{x}\\ \hat{y}\\ \hat{z}\end{bmatrix}\cdot\bar{D}=\varepsilon_0\begin{bmatrix}\varepsilon_{11}'' & \varepsilon_{12}'' & \varepsilon_{13}''\\ \varepsilon_{12}'' & \varepsilon_{22}'' & \varepsilon_{23}''\\ \varepsilon_{13}'' & \varepsilon_{23}'' & \varepsilon_{33}''\end{bmatrix}\begin{bmatrix}\cos\psi & -\sin\psi & 0\\ \sin\psi & \cos\psi & 0\\ 0 & 0 & 1\end{bmatrix}\begin{bmatrix}\hat{x}\\ \hat{y}\\ \hat{z}\end{bmatrix}\cdot\bar{E}, \tag{4.26}$$

and premultiplying (4.26) with the rotation matrix in (4.24) gives

$$\begin{bmatrix}\hat{x}\\ \hat{y}\\ \hat{z}\end{bmatrix}\cdot\bar{D}=\varepsilon_0\begin{bmatrix}\cos\psi & \sin\psi & 0\\ -\sin\psi & \cos\psi & 0\\ 0 & 0 & 1\end{bmatrix}\begin{bmatrix}\varepsilon_{11}'' & \varepsilon_{12}'' & \varepsilon_{13}''\\ \varepsilon_{12}'' & \varepsilon_{22}'' & \varepsilon_{23}''\\ \varepsilon_{13}'' & \varepsilon_{23}'' & \varepsilon_{33}''\end{bmatrix}\begin{bmatrix}\cos\psi & -\sin\psi & 0\\ \sin\psi & \cos\psi & 0\\ 0 & 0 & 1\end{bmatrix}\begin{bmatrix}\hat{x}\\ \hat{y}\\ \hat{z}\end{bmatrix}\cdot\bar{E}. \tag{4.27}$$

After multiplication, (4.27) gives

$$\begin{bmatrix}\hat{x}\\ \hat{y}\\ \hat{z}\end{bmatrix}\cdot\bar{D}=\varepsilon_0\begin{bmatrix}\varepsilon_{11} & \varepsilon_{12} & \varepsilon_{13}\\ \varepsilon_{12} & \varepsilon_{22} & \varepsilon_{23}\\ \varepsilon_{13} & \varepsilon_{23} & \varepsilon_{33}\end{bmatrix}\begin{bmatrix}\hat{x}\\ \hat{y}\\ \hat{z}\end{bmatrix}\cdot\bar{E} \tag{4.28}$$

where

$$\varepsilon_{11}=\cos^2\psi\left(\varepsilon_x\cos^2\alpha+\varepsilon_y\sin^2\alpha\right)+2\left(\varepsilon_y-\varepsilon_x\right)\cos\alpha\sin\alpha\cos\beta\sin\psi\cos\psi$$
$$+\sin^2\psi\left[\cos^2\beta\left(\varepsilon_y\cos^2\alpha+\varepsilon_x\sin^2\alpha\right)+\varepsilon_z\sin^2\beta\right] \tag{4.29}$$

$$\varepsilon_{12}=-\sin\psi\cos\psi\left(\varepsilon_x\cos^2\alpha+\varepsilon_y\sin^2\alpha\right)+\left(\varepsilon_y-\varepsilon_x\right)\cos\alpha\sin\alpha\cos\beta\cos^2\psi-\sin^2\psi\left(\varepsilon_y-\varepsilon_x\right)\cos\alpha\sin\alpha\cos\beta$$
$$+\sin\psi\cos\psi\left[\cos^2\beta\left(\varepsilon_y\cos^2\alpha+\varepsilon_x\sin^2\alpha\right)+\varepsilon_z\sin^2\beta\right] \tag{4.30}$$

$$\varepsilon_{13}=\left(\varepsilon_y-\varepsilon_x\right)\cos\alpha\sin\alpha\sin\beta\cos\psi+\cos\beta\sin\beta\sin\psi\left(\varepsilon_y\cos^2\alpha+\varepsilon_x\sin^2\alpha\right)-\varepsilon_z\cos\beta\sin\beta\sin\psi \tag{4.31}$$

$$\varepsilon_{22}=\sin^2\psi\left(\varepsilon_x\cos^2\alpha+\varepsilon_y\sin^2\alpha\right)-2\left(\varepsilon_y-\varepsilon_x\right)\cos\alpha\sin\alpha\cos\beta\cos\psi\sin\psi$$
$$+\cos^2\psi\left[\cos^2\beta\left(\varepsilon_y\cos^2\alpha+\varepsilon_x\sin^2\alpha\right)+\varepsilon_z\sin^2\beta\right] \tag{4.32}$$

$$\varepsilon_{23}=-\sin\psi\left(\varepsilon_y-\varepsilon_x\right)\cos\alpha\sin\alpha\sin\beta+\cos\psi\cos\beta\sin\beta\left(\varepsilon_y\cos^2\alpha+\varepsilon_x\sin^2\alpha\right)-\varepsilon_z\cos\beta\sin\beta\cos\psi \tag{4.33}$$

$$\varepsilon_{33}=\varepsilon_z\cos^2\beta+\left(\varepsilon_y\cos^2\alpha+\varepsilon_x\sin^2\alpha\right)\sin^2\beta. \tag{4.34}$$

The equations in (4.29) —(4.34) define a diagonal dielectric tensor in the experimental coordinate system transformed through a series of three rotations to the laboratory system.

Taking the uniaxial case where $\varepsilon_x = \varepsilon_y = \varepsilon$, (4.29)—(4.34) reduce to

$$\varepsilon_{11} = \varepsilon(\cos^2\psi + \cos^2\beta\sin^2\psi) + \varepsilon_z\sin^2\beta\sin^2\psi \quad 4.35$$

$$\varepsilon_{12} = (\varepsilon_z - \varepsilon)\sin^2\beta\,\sin\psi\cos\psi \quad 4.36$$

$$\varepsilon_{13} = (\varepsilon - \varepsilon_z)\sin\beta\cos\beta\sin\psi \quad 4.37$$

$$\varepsilon_{22} = \varepsilon(\sin^2\psi + \cos^2\beta\cos^2\psi) + \varepsilon_z\sin^2\beta\cos^2\psi \quad 4.38$$

$$\varepsilon_{23} = (\varepsilon - \varepsilon_z)\sin\beta\cos\beta\cos\psi \quad 4.39$$

$$\varepsilon_{33} = \varepsilon\sin^2\beta + \varepsilon_z\cos^2\beta, \quad 4.40$$

and now using (4.35) — (4.40) for uniaxial media one finally has the displacement vector D for a diagonal permittivity tensor in the experimental coordinate system represented in the laboratory coordinate system. This can be thought of as analogous to an arbitrary rotation of the optic axis. The components of the displacement vector D are given by

$$\begin{bmatrix} D_x \\ D_y \\ D_z \end{bmatrix} = \varepsilon_0 \begin{bmatrix} \varepsilon_{11} & \varepsilon_{12} & \varepsilon_{13} \\ \varepsilon_{12} & \varepsilon_{22} & \varepsilon_{23} \\ \varepsilon_{13} & \varepsilon_{23} & \varepsilon_{33} \end{bmatrix} \begin{bmatrix} E_x \\ E_y \\ E_z \end{bmatrix} \quad 4.41$$

4.2 Propagation Constant Derivation

From waveguide theory, TE_{mn} modes are solved for in terms of H_z. Therefore, the solution of H_z provides the solution for TE modes and the propagation constant. Using the rotated permittivity matrix derived in the last section, dispersion relations are now solved for.

Maxwell's Equations are now

$$\nabla\times \bar{E} = -j\omega\mu_o\bar{H} \quad 4.42$$

$$\nabla \times \bar{H} = j\omega\varepsilon_o\bar{\bar{\varepsilon}}_r\bar{E} \quad 4.43$$

where

$$\overline{\overline{\varepsilon_r}} = \begin{bmatrix} \varepsilon_{11} & \varepsilon_{12} & \varepsilon_{13} \\ \varepsilon_{12} & \varepsilon_{22} & \varepsilon_{23} \\ \varepsilon_{13} & \varepsilon_{23} & \varepsilon_{33} \end{bmatrix} \quad 4.44$$

and the matrix elements of (4.44) are given from (4.35) — (4.40) . Rearranging (4.43) yields

$$(\overline{\overline{\varepsilon_r}})^{-1} \cdot (\nabla \times \bar{H}) = j\omega\varepsilon_o \bar{E} \quad 4.45$$

Taking the curl of both sides yields

$$\nabla \times \left((\overline{\overline{\varepsilon_r}})^{-1} \cdot (\nabla \times \bar{H})\right) = j\omega\varepsilon_o (\nabla \times \bar{E}) \quad 4.46$$

Equation (4.42) is substituted into the RHS of eq. (4.46) resulting in

$$\nabla \times \left((\overline{\overline{\varepsilon_r}})^{-1} \cdot (\nabla \times \bar{H})\right) = j\omega\varepsilon_o (-j\omega\mu_o \bar{H}) \quad 4.47$$

Grouping the constants provides

$$\nabla \times \left((\overline{\overline{\varepsilon_r}})^{-1} \cdot (\nabla \times \bar{H})\right) = \omega^2 \varepsilon_o \mu_o (\bar{H}) = k_o^2 (\bar{H}) \quad 4.48$$

For substitution simplicity assume $\overline{\overline{\alpha_r}} = (\overline{\overline{\varepsilon_r}})^{-1}$. Now expanding $(\overline{\overline{\varepsilon_r}})^{-1} \cdot (\nabla \times \bar{H})$

$$\overline{\overline{\alpha_r}} \cdot (\nabla \times \bar{H}) = \begin{bmatrix} \alpha_{11} & \alpha_{12} & \alpha_{13} \\ \alpha_{12} & \alpha_{22} & \alpha_{23} \\ \alpha_{13} & \alpha_{23} & \alpha_{33} \end{bmatrix} \cdot \begin{bmatrix} \frac{\partial}{\partial y} H_z - \frac{\partial}{\partial z} H_y \\ \frac{\partial}{\partial z} H_x - \frac{\partial}{\partial x} H_z \\ \frac{\partial}{\partial x} H_y - \frac{\partial}{\partial y} H_x \end{bmatrix} = \begin{bmatrix} \alpha_{11} & \alpha_{12} & \alpha_{13} \\ \alpha_{12} & \alpha_{22} & \alpha_{23} \\ \alpha_{13} & \alpha_{23} & \alpha_{33} \end{bmatrix} \cdot \begin{bmatrix} G_x \\ G_y \\ G_z \end{bmatrix} = \begin{bmatrix} \alpha_{11} G_x + \alpha_{12} G_y + \alpha_{13} G_z \\ \alpha_{12} G_x + \alpha_{22} G_y + \alpha_{23} G_z \\ \alpha_{13} G_x + \alpha_{23} G_y + \alpha_{33} G_z \end{bmatrix} \quad 4.49$$

where

$$G_x = \frac{\partial}{\partial y} H_z - \frac{\partial}{\partial z} H_y$$

$$G_y = \frac{\partial}{\partial z} H_x - \frac{\partial}{\partial x} H_z$$

$$G_z = \frac{\partial}{\partial x} H_y - \frac{\partial}{\partial y} H_x \quad 4.50$$

and now

$$\nabla \times \begin{bmatrix} \alpha_{11}G_x + \alpha_{12}G_y + \alpha_{13}G_z \\ \alpha_{12}G_x + \alpha_{22}G_y + \alpha_{23}G_z \\ \alpha_{13}G_x + \alpha_{23}G_y + \alpha_{33}G_z \end{bmatrix} = \nabla \times \begin{bmatrix} G_x' \\ G_y' \\ G_z' \end{bmatrix} = \hat{x}\left(\frac{\partial}{\partial y}G_z' - \frac{\partial}{\partial z}G_y'\right) + \hat{y}\left(\frac{\partial}{\partial z}G_x' - \frac{\partial}{\partial x}G_z'\right) + \hat{z}\left(\frac{\partial}{\partial x}G_y' - \frac{\partial}{\partial y}G_x'\right) \quad 4.51$$

where

$$G_x' = \alpha_{11}G_x + \alpha_{12}G_y + \alpha_{13}G_z$$

$$G_y' = \alpha_{12}G_x + \alpha_{22}G_y + \alpha_{23}G_z$$

$$G_z' = \alpha_{13}G_x + \alpha_{23}G_y + \alpha_{33}G_z \quad 4.52$$

Looking at the z-component of (4.51),

$$\left(\frac{\partial}{\partial x}G_y' - \frac{\partial}{\partial y}G_x'\right) = \left(\frac{\partial}{\partial x}\left(\alpha_{12}G_x + \alpha_{22}G_y + \alpha_{23}G_z\right) - \frac{\partial}{\partial y}\left(\alpha_{11}G_x + \alpha_{12}G_y + \alpha_{13}G_z\right)\right)$$

$$= \alpha_{12}\frac{\partial}{\partial x}\left(\frac{\partial}{\partial y}H_z - \frac{\partial}{\partial z}H_y\right) + \alpha_{22}\frac{\partial}{\partial x}\left(\frac{\partial}{\partial z}H_x - \frac{\partial}{\partial x}H_z\right) + \alpha_{23}\frac{\partial}{\partial x}\left(\frac{\partial}{\partial x}H_y - \frac{\partial}{\partial y}H_x\right)$$

$$-\alpha_{11}\frac{\partial}{\partial y}\left(\frac{\partial}{\partial y}H_z - \frac{\partial}{\partial z}H_y\right) \quad - \alpha_{12}\frac{\partial}{\partial y}\left(\frac{\partial}{\partial z}H_x - \frac{\partial}{\partial x}H_z\right) - \alpha_{13}\frac{\partial}{\partial y}\left(\frac{\partial}{\partial x}H_y - \frac{\partial}{\partial y}H_x\right) \quad 4.53$$

after distributing each outside derivative

$$= \alpha_{12}\frac{\partial^2}{\partial x\partial y}H_z - \alpha_{12}\frac{\partial^2}{\partial x\partial z}H_y + \alpha_{22}\frac{\partial^2}{\partial x\partial z}H_x - \alpha_{22}\frac{\partial^2}{\partial x^2}H_z + \alpha_{23}\frac{\partial^2}{\partial x^2}H_y - \alpha_{23}\frac{\partial^2}{\partial x\partial y}H_x - \alpha_{11}\frac{\partial^2}{\partial y^2}H_z$$

$$+\alpha_{11}\frac{\partial^2}{\partial y\partial z}H_y - \alpha_{12}\frac{\partial^2}{\partial y\partial z}H_x + \alpha_{12}\frac{\partial^2}{\partial x\partial y}H_z - \alpha_{13}\frac{\partial^2}{\partial x\partial y}H_y + \alpha_{13}\frac{\partial^2}{\partial y^2}H_x \quad 4.54$$

Grouping like terms and equating to the z-component of the right-hand side of eq. (4.48)

$$\left(\alpha_{22}\frac{\partial^2}{\partial x\partial z} - \alpha_{23}\frac{\partial^2}{\partial x\partial y} - \alpha_{12}\frac{\partial^2}{\partial y\partial z} + \alpha_{13}\frac{\partial^2}{\partial y^2}\right)H_x + \left(-\alpha_{12}\frac{\partial^2}{\partial x\partial z} + \alpha_{23}\frac{\partial^2}{\partial x^2} + \alpha_{11}\frac{\partial^2}{\partial y\partial z} - \alpha_{13}\frac{\partial^2}{\partial x\partial y}\right)H_y$$

$$+\left(\alpha_{12}\frac{\partial^2}{\partial x\partial y} - \alpha_{22}\frac{\partial^2}{\partial x^2} - \alpha_{11}\frac{\partial^2}{\partial y^2} + \alpha_{12}\frac{\partial^2}{\partial x\partial y}\right)H_z = k_o^2 H_z \quad 4.55$$

Assuming H_z is in the form $\cos(k_x x)\cos(k_y y)\, e^{-j k_z z}$ one can see that determining the propagation constant is difficult. Due to the coupling of H-field components the waveguide equations no longer hold. However, in a rectangular waveguide system assuming only TE_{m0} modes propagate, and limiting the rotation to three cases most commonly found in dielectrics, knowing $H_y = E_x = k_y = 0$, and from $\nabla \cdot \bar{H} = 0$ eq. (4.55) reduces to

$$\left(-\alpha_{22}\frac{\partial^2}{\partial z^2}H_z\right) + \left(-\alpha_{22}\frac{\partial^2}{\partial x^2}\right)H_z = k_o^2 H_z \qquad 4.56$$

The three special cases of angles α, β, and ψ in (4.35)–(4.40) represent the most common alignments of optic axis in microwave substrates.

4.2.1 Case 1 α=β=ψ=0

This case corresponds to the optic axis being parallel to the z-axis, and solving (4.56) for k_z with H_z given by the previously assumed form with $k_y=0$, we obtain

$$k_z = -j\sqrt{k_x^2 - \varepsilon_{22}k_o^2}, \quad \varepsilon_{22} = \varepsilon \qquad 4.57$$

where ε_{22} is given from (4.38), and α, β, and ψ are defined by the Subsection title.

4.2.2 Case 2 α=0, β=π/2, ψ=0

Assuming that the optic axis is the z axis in the experimental coordinate system, this case corresponds to the optic axis being parallel to the y-axis, and solving (4.56) for k_z with H_z given by the previously assumed form we obtain

$$k_z = -j\sqrt{k_x^2 - \varepsilon_{22}k_o^2}, \quad \varepsilon_{22} = \varepsilon_z \qquad 4.58$$

where ε_{22} is given from (4.38), and α, β, and ψ are defined by the Subsection title.

4.2.3 Case 3 α=0, β=π/2, ψ= π/2

Assuming that the optic axis is the z axis in the experimental coordinate system, this case corresponds to the optic axis being parallel to the x-axis. Again solving (4.56) for k_z with H_z given by the previously assumed form we obtain

$$k_z = -j\sqrt{k_x^2 - \varepsilon_{22}k_o^2}, \quad \varepsilon_{22} = \varepsilon \tag{4.59}$$

where ε_{22} is given from (4.38), and α, β, and ψ are defined by the Subsection title.

4.2.4 Application of Mode-Matching Method in Uniaxial Media

The theory of mode-matching is covered in detail in Section 2, so it will only be briefly reiterated here as the numerical computation is essentially the same, but the wave admittance now equals

$$Y_{im} = \frac{\gamma_{im}}{j\omega\mu}, i = a \; or \; b \tag{4.60}$$

with γ_{im} equal to that in one of the 3 cases in Sections 4.2. Numerical calculation is then carried out in the same manner as in Section 2.

4.3 Analysis of Simple Step Discontinuities in Waveguides Filled with Rotated Anisotropic Uniaxial Media

Step discontinuities are solved for with a rotated medium present. A rotated anisotropic uniaxial medium is one whose optic axis is not the z-axis. It is still assumed that only TE_{m0} modes for {m=1,2,…,M} are present. Using the method of the previous section numerical

results follow. All analyses in the proceeding sections are based on Figure 4.5. It is assumed in the following section the dielectric tensor is of the form (4.1) in the experimental coordinate system (i.e. diagonal), but is uniaxial with $\varepsilon_x = \varepsilon_y = 2$ and $\varepsilon_z = 3$ being the optic axis. For given angles of rotation, (4.35)−(4.40) provide the resulting dielectric tensor in the laboratory coordinate system. In Appendix A, it is easily shown that the same waveguide equations similar to those of Section 1.3 hold for the three special cases of rotation in Section 4.2.1, 4.2.2, and 4.2.3.

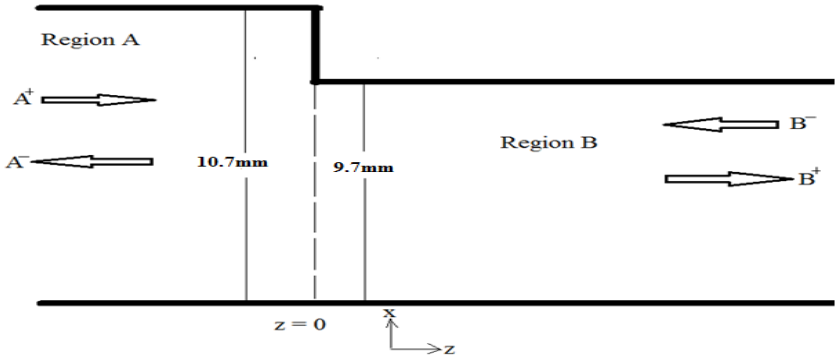

Figure 4.5 Simple Step Discontinuity filled with Rotated Media

4.3.1 Rotated Media for Case 1 where there is no rotation (α=0, β=0, ψ=0)

Looking at Figure 4.6 the rotation angles of α=0, β=0, ψ=0 with a wave propagating in the z direction correspond to $\epsilon_{11} = \epsilon_{22} = \varepsilon = 2$, and $\epsilon_{33} = 3$. Compared to an isotropic case the response should match that of $\varepsilon = 2$, which looking at Figure 4.7 it does.

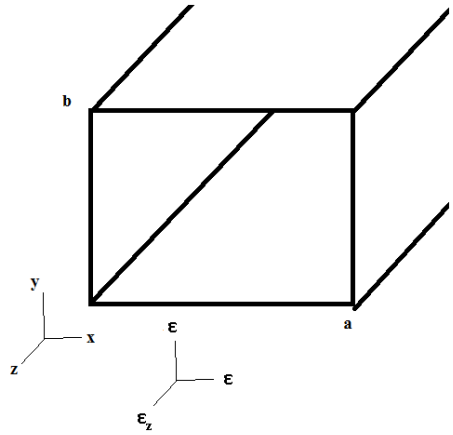

Figure 4.6 Rotated medium with α=0, β=0, ψ=0 ($\boldsymbol{\epsilon_{11} = 2, \epsilon_{22} = 2, \epsilon_{33} = 3}$)

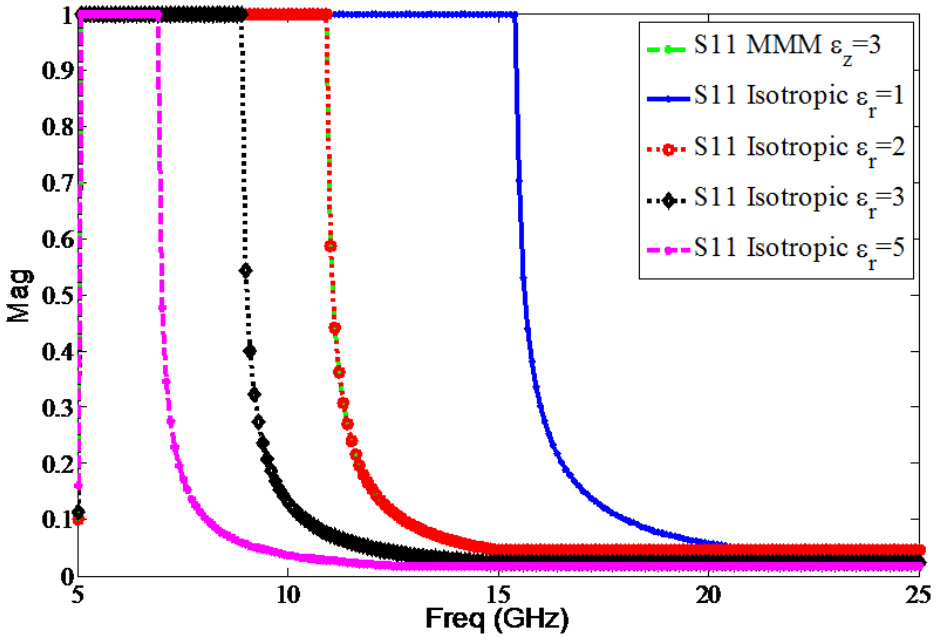

Figure 4.7 Magnitude of S_{11} coefficients of rotated medium with α=0, β=0, ψ=0 ($\boldsymbol{\epsilon_{11} = 2, \epsilon_{22} = 2, \epsilon_{33} = 3}$)

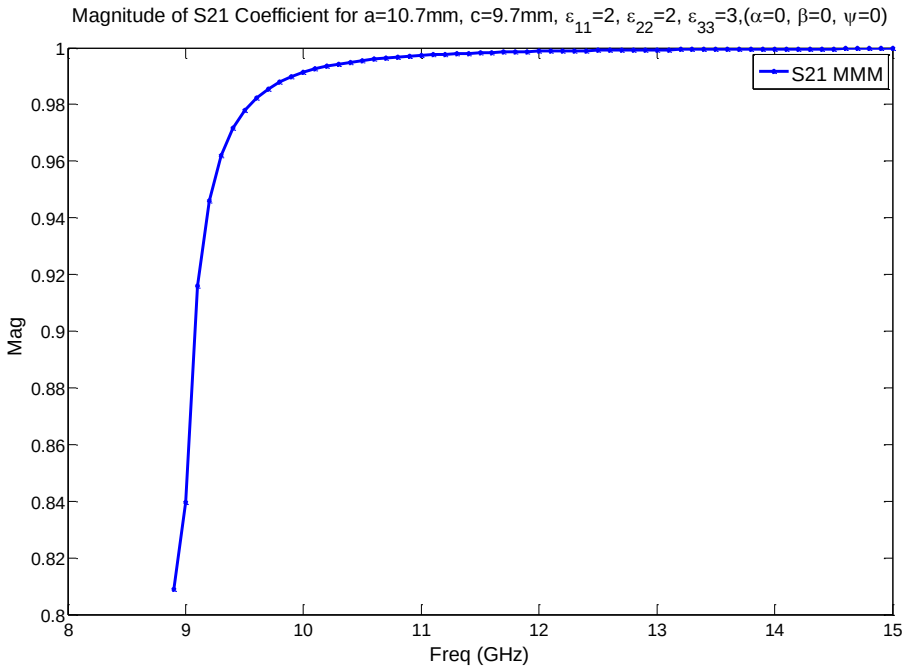

Figure 4.8 Magnitude of S_{21} coefficients of rotated medium with α=0, β=0, ψ=0 ($\boldsymbol{\epsilon_{11} = 2, \epsilon_{22} = 2, \epsilon_{33} = 3}$)

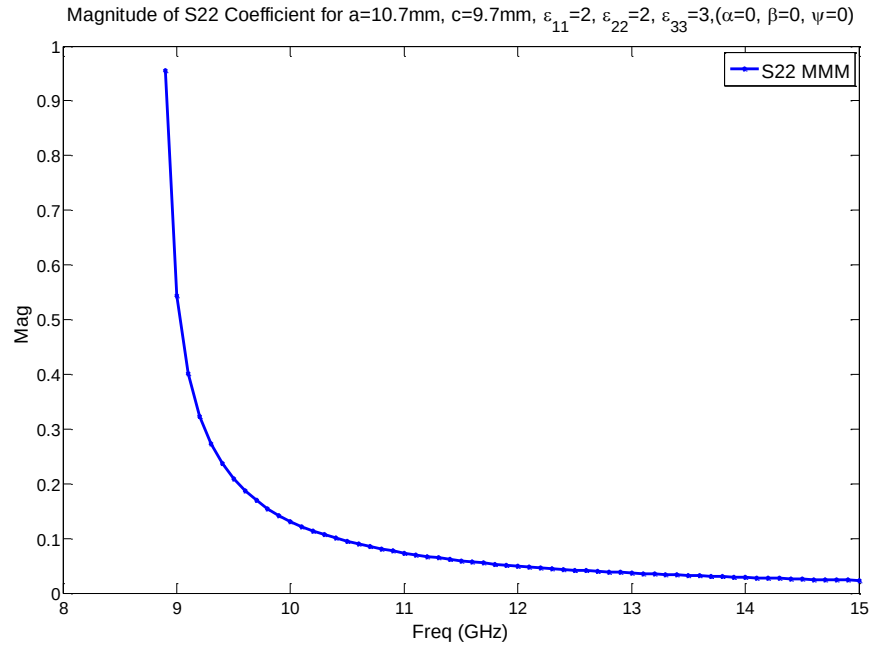

Figure 4.9 Magnitude of S_{22} coefficients of rotated medium with α=0, β=0, ψ=0 ($\boldsymbol{\epsilon_{11} = 2, \epsilon_{22} = 2, \epsilon_{33} = 3}$)

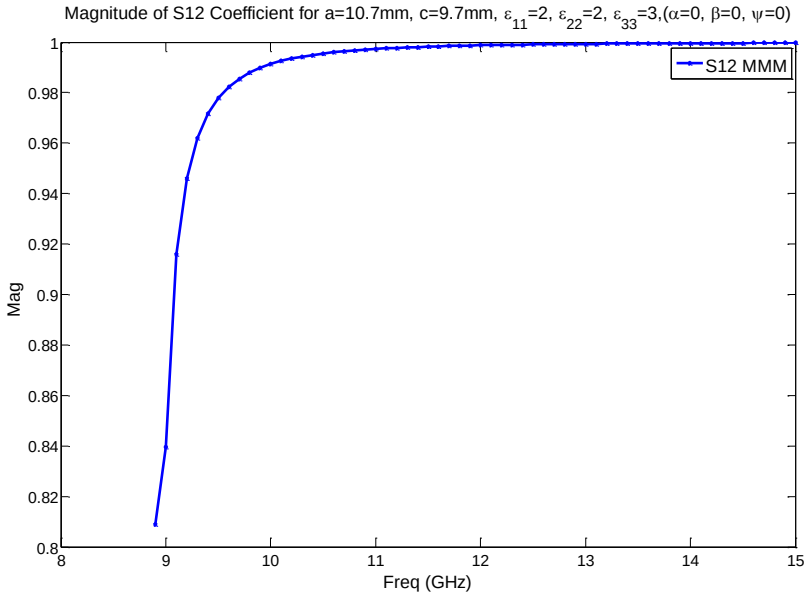

Figure 4.10 Magnitude of S_{12} coefficients of rotated medium with α=0, β=0, ψ=0 ($\boldsymbol{\epsilon_{11} = 2, \epsilon_{22} = 2, \epsilon_{33} = 3}$)

4.3.1.1 Comparison of MMM vs. FEM Results for α=0, β=0, ψ=0

Figure 4.11 through Figure 4.14 display the numerically computed results of MMM vs. the FEM results.

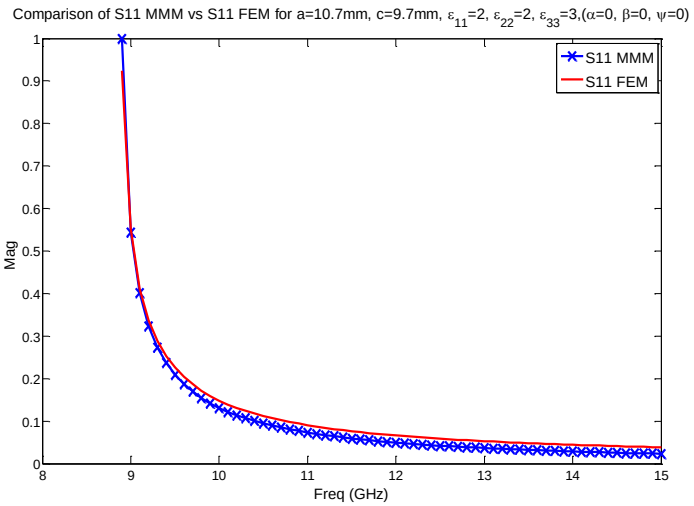

Figure 4.11 Magnitude of MMM vs. FEM S_{11} coefficients of rotated medium with α=0, β=0, ψ=0 ($\boldsymbol{\epsilon_{11} = 2, \epsilon_{22} = 2, \epsilon_{33} = 3}$)

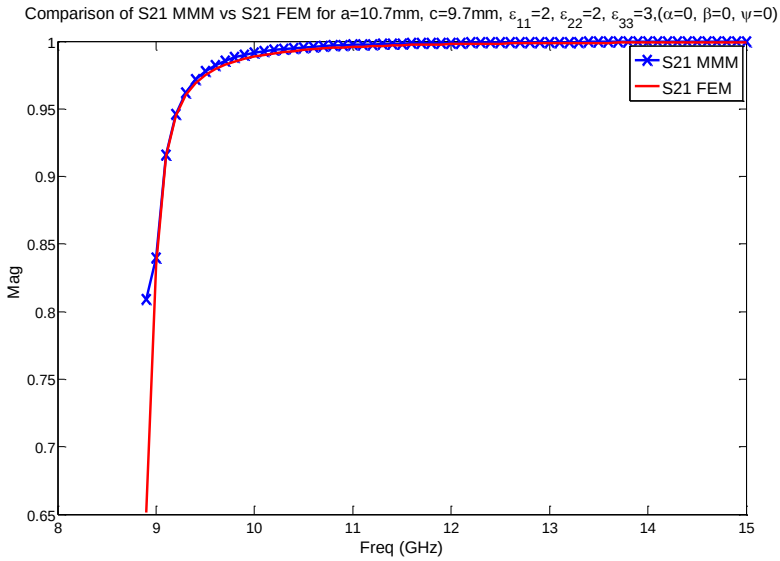

Figure 4.12 Magnitude of MMM vs. FEM S_{21} coefficients of rotated medium with α=0, β=0, ψ=0 ($\boldsymbol{\epsilon_{11} = 2, \epsilon_{22} = 2, \epsilon_{33} = 3}$)

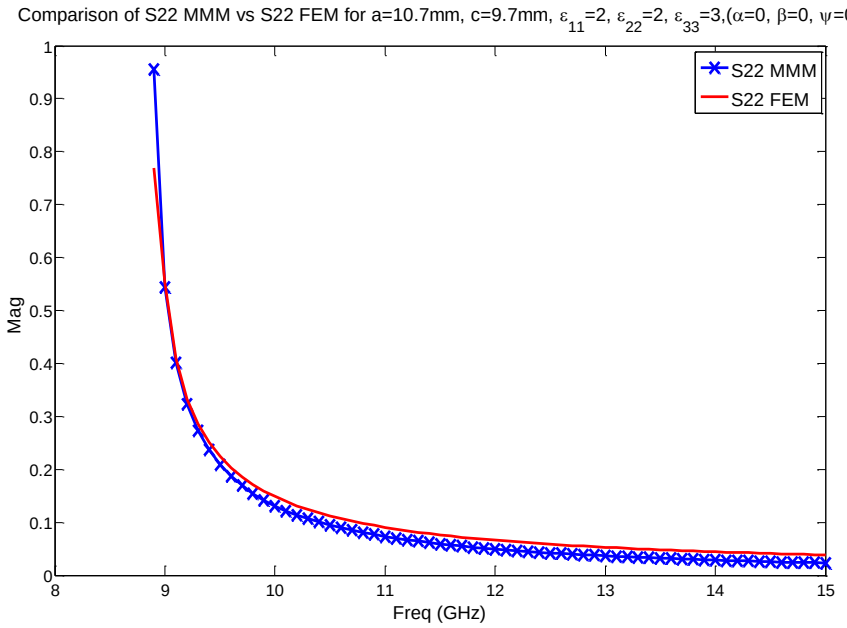

Figure 4.13 Magnitude of MMM vs. FEM S_{22} Coefficients of Rotated medium with α=0, β=0, ψ=0 ($\boldsymbol{\epsilon_{11} = 2, \epsilon_{22} = 2, \epsilon_{33} = 3}$)

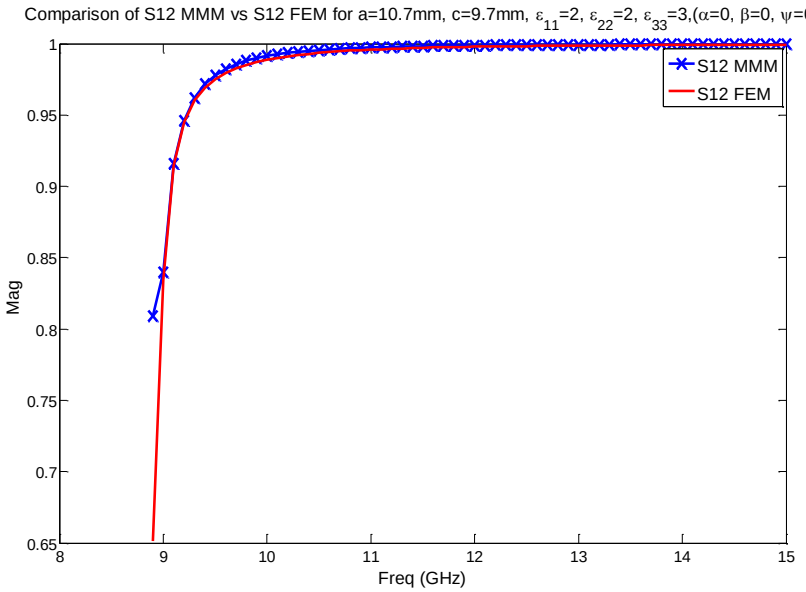

Figure 4.14 Magnitude of MMM vs. FEM S_{12} coefficients of rotated medium with α=0, β=0, ψ=0 ($\boldsymbol{\epsilon_{11} = 2, \epsilon_{22} = 2, \epsilon_{33} = 3}$)

4.3.2 Rotated Media for Case 2 (α=0, β=90, ψ=0)

Looking at Figure 4.15 the rotation α=0, β=90, ψ=0 with a wave propagating in the z direction corresponds to $\epsilon_{11} = 2$, $\epsilon_{22} = 3$, and $\epsilon_{33} = 2$. Compared to an isotropic case the response should match that of $\varepsilon = 3$, which looking at Figure 4.16 it does.

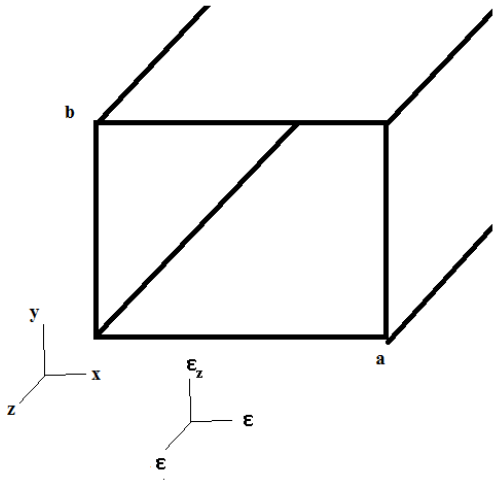

Figure 4.15 Rotated medium with α=0, β=90, ψ=0 ($\boldsymbol{\epsilon_{11} = 2, \epsilon_{22} = 3, \epsilon_{33} = 2}$)

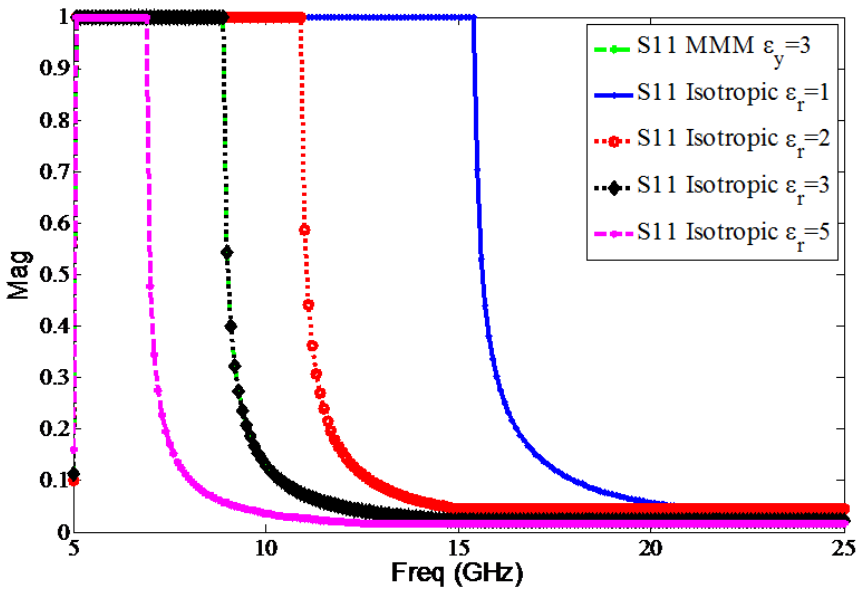

Figure 4.16 Magnitude of S_{11} coefficients of rotated medium with α=0, β=90, ψ=0 ($\boldsymbol{\epsilon_{11} = 2, \epsilon_{22} = 3, \epsilon_{33} = 2}$)

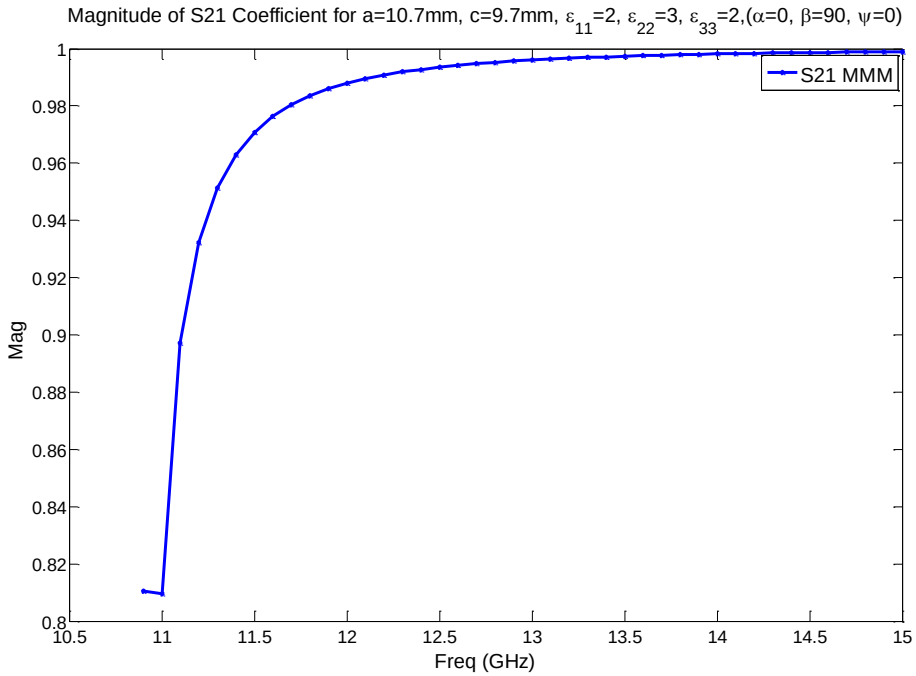

Figure 4.17 Magnitude of S_{21} coefficients of rotated medium with α=0, β=90, ψ=0 ($\boldsymbol{\epsilon_{11} = 2, \epsilon_{22} = 3, \epsilon_{33} = 2}$)

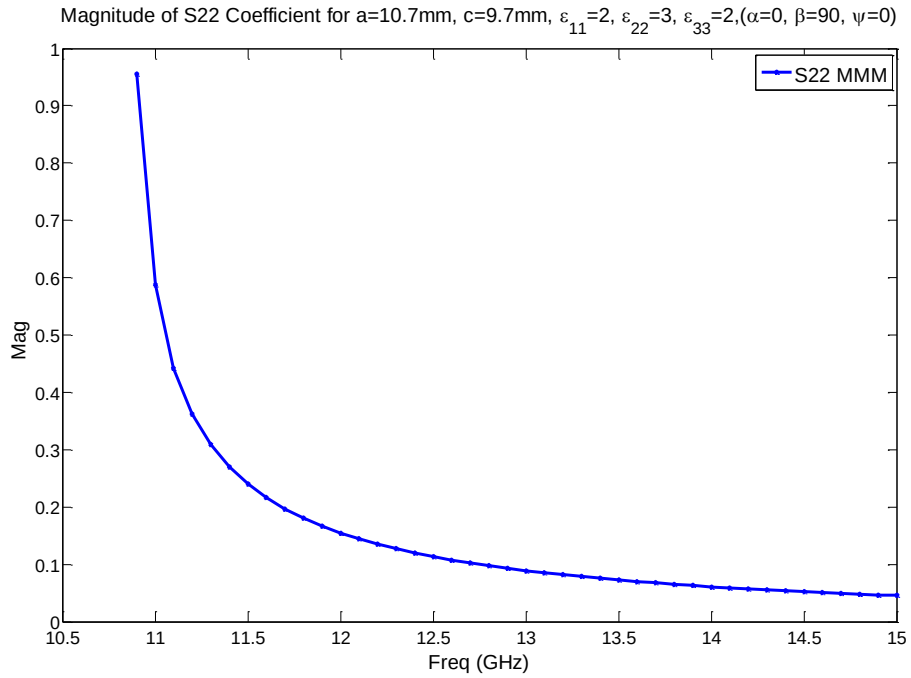

Figure 4.18 Magnitude of S_{22} coefficients of rotated medium with α=0, β=90, ψ=0 ($\boldsymbol{\epsilon_{11} = 2, \epsilon_{22} = 3, \epsilon_{33} = 2}$)

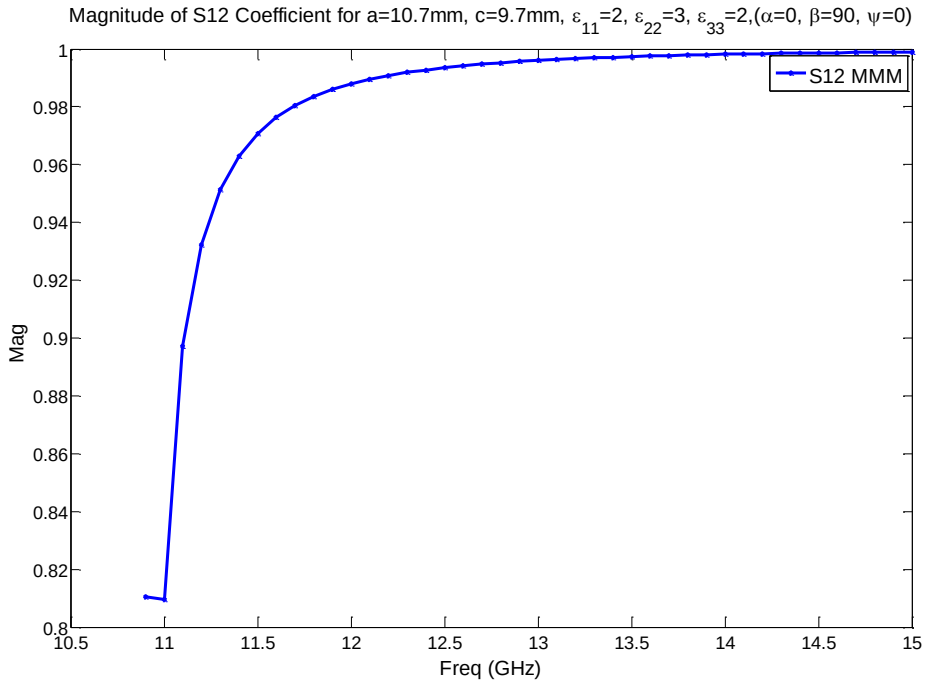

Figure 4.19 Magnitude of S_{12} coefficients of rotated medium with α=0, β=90, ψ=0 ($\boldsymbol{\epsilon_{11} = 2, \epsilon_{22} = 3, \epsilon_{33} = 2}$)

4.3.2.1 Comparison of MMM vs. FEM Results for α=0, β=90, ψ=0

Figure 4.20 through Figure 4.23 display the numerically computed results of MMM vs. the FEM results.

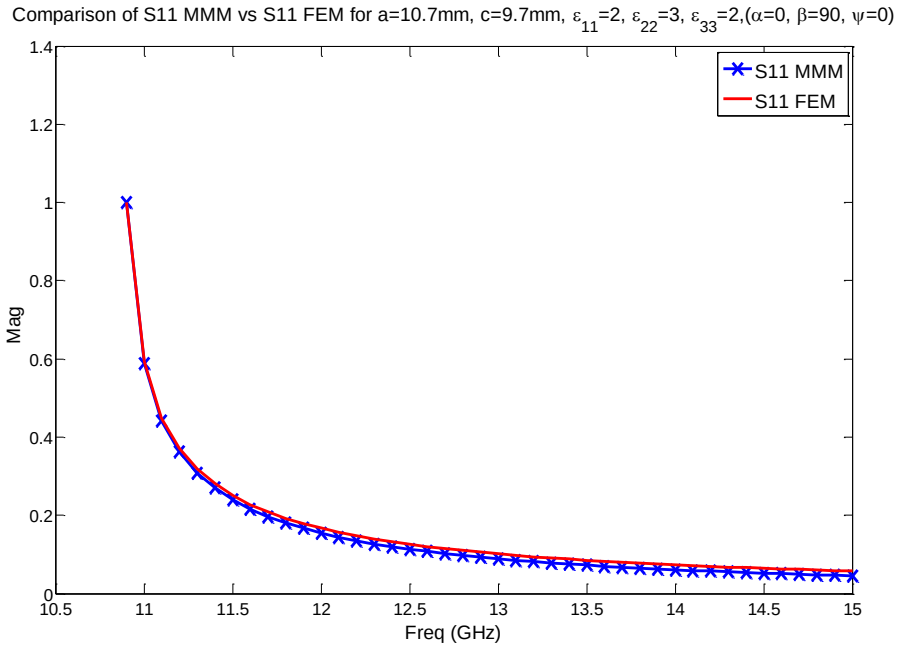

Figure 4.20 Magnitude of MMM vs. FEM S_{11} coefficients of rotated medium with α=0, β=90, ψ=0 ($\boldsymbol{\epsilon_{11}=2, \epsilon_{22}=3, \epsilon_{33}=2}$)

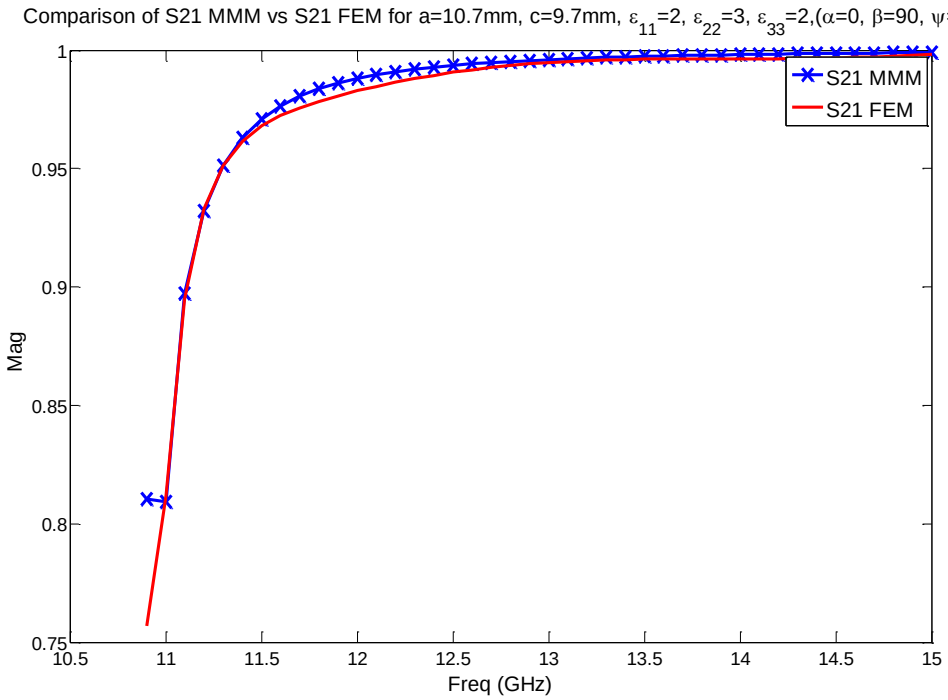

Figure 4.21 Magnitude of MMM vs. FEM S_{21} coefficients of rotated medium with α=0, β=90, ψ=0 ($\boldsymbol{\epsilon_{11} = 2, \epsilon_{22} = 3, \epsilon_{33} = 2}$)

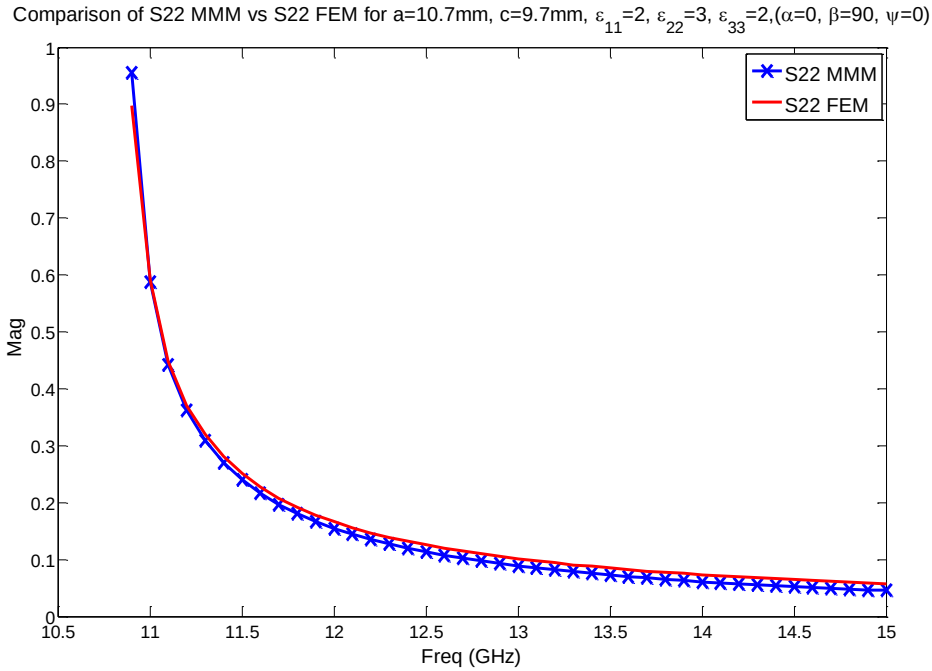

Figure 4.22 Magnitude of MMM vs. FEM S_{22} coefficients of rotated medium with α=0, β=90, ψ=0 ($\boldsymbol{\epsilon_{11} = 2, \epsilon_{22} = 3, \epsilon_{33} = 2}$)

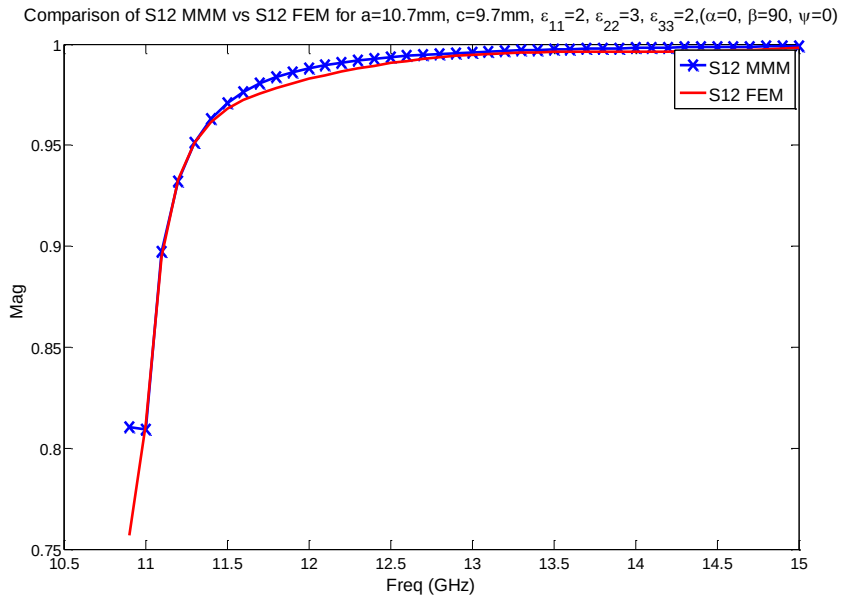

Figure 4.23 Magnitude of MMM vs. FEM S_{12} coefficients of rotated medium with α=0, β=90, ψ=0 ($\boldsymbol{\epsilon_{11} = 2, \epsilon_{22} = 3, \epsilon_{33} = 2}$)

4.3.3 Rotated Media for Case 3 (α=0, β=90, ψ=90)

Looking at Figure 4.24 the rotation α=0, β=90, ψ=90 with a wave propagating in the z direction corresponds to the alignment of $\epsilon_{11} = 3$, $\epsilon_{22} = 2$, and $\epsilon_{33} = 2$. Compared to an isotropic case the response should match that of $\varepsilon = 2$, which looking at Figure 4.25 it does.

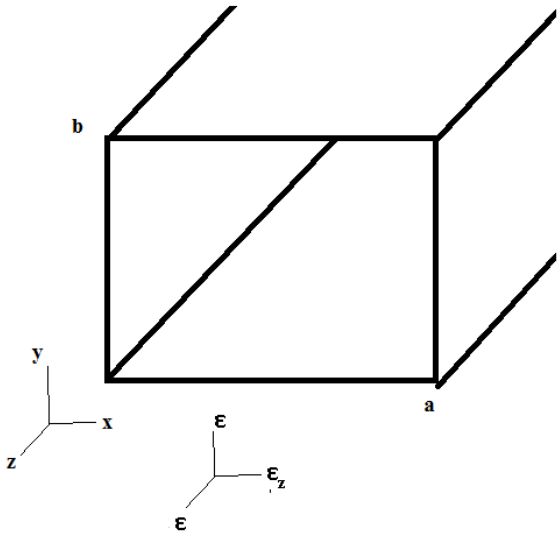

Figure 4.24 Rotated medium with α=0, β=90, ψ=90

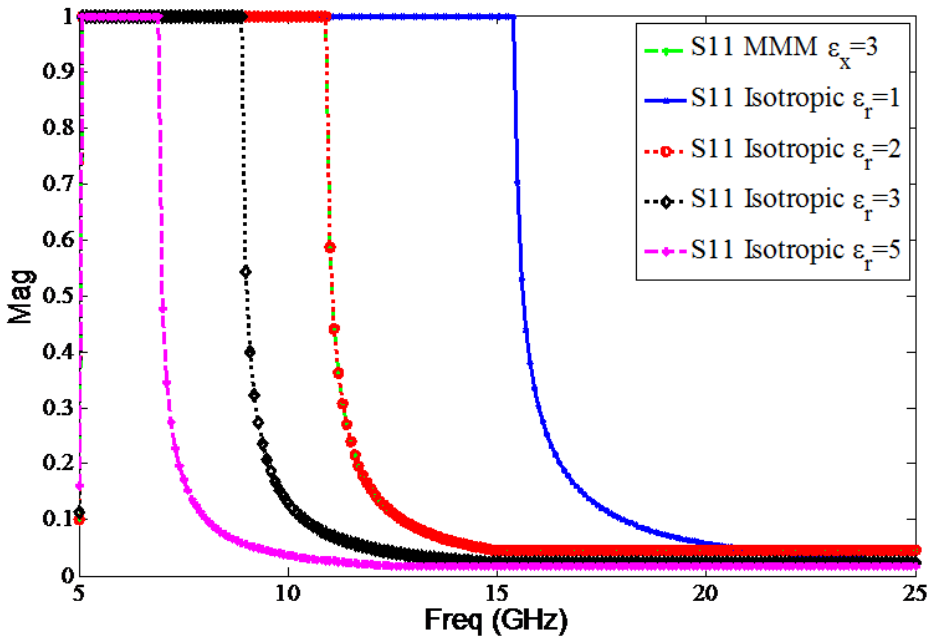

Figure 4.25 Magnitude of S_{11} coefficients of rotated medium with α=0, β=90, ψ=90 ($\boldsymbol{\epsilon_{11} = 3, \epsilon_{22} = 2, \epsilon_{33} = 2}$)

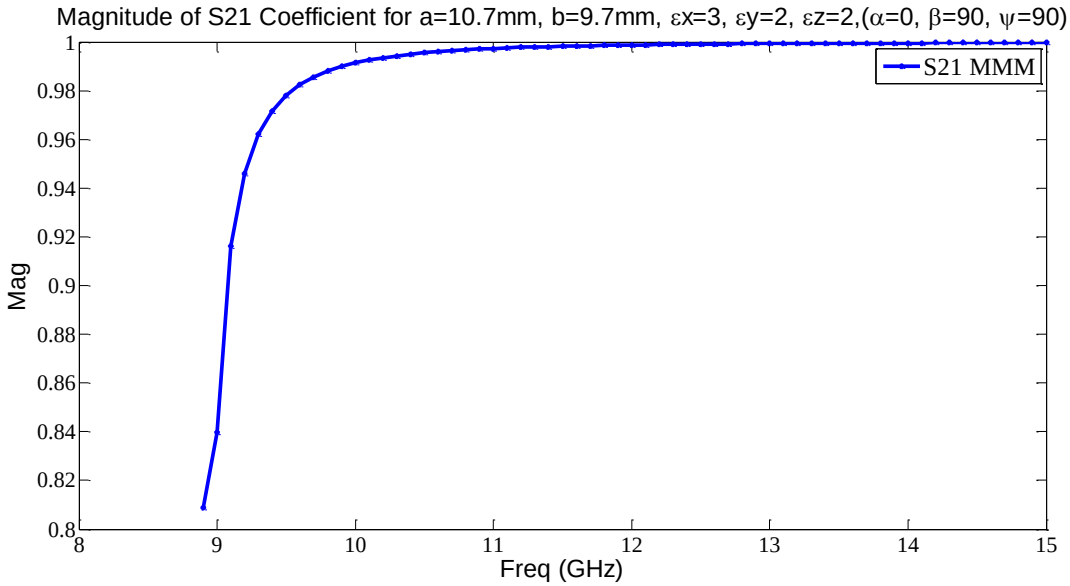

Figure 4.26 Magnitude of S_{21} coefficients of rotated medium with α=0, β=90, ψ=90 ($\boldsymbol{\epsilon_{11} = 3, \epsilon_{22} = 2, \epsilon_{33} = 2}$)

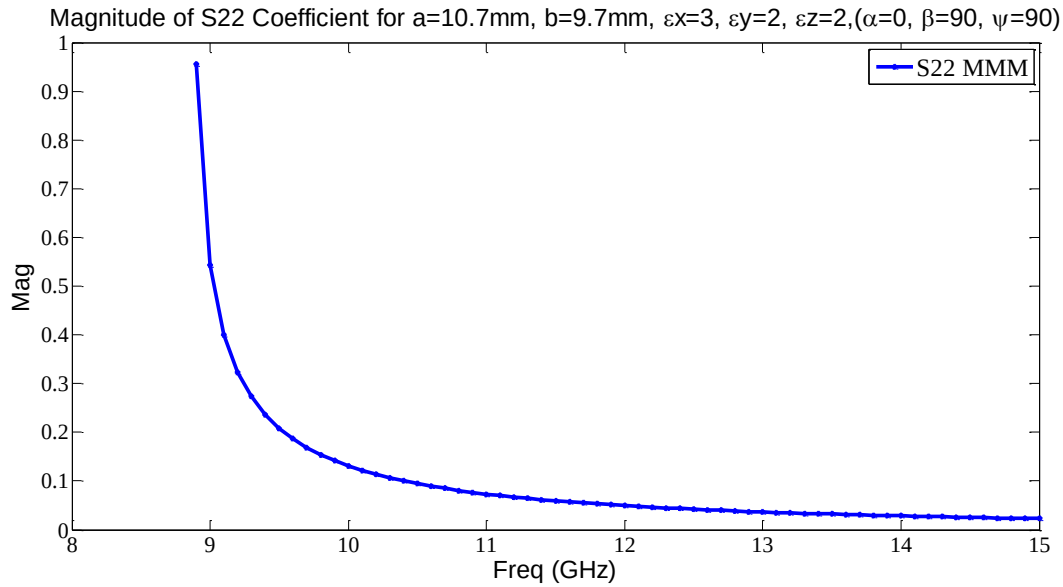

Figure 4.27 Magnitude of S_{22} coefficients of rotated medium with α=0, β=90, ψ=90 ($\boldsymbol{\epsilon_{11} = 3, \epsilon_{22} = 2, \epsilon_{33} = 2}$)

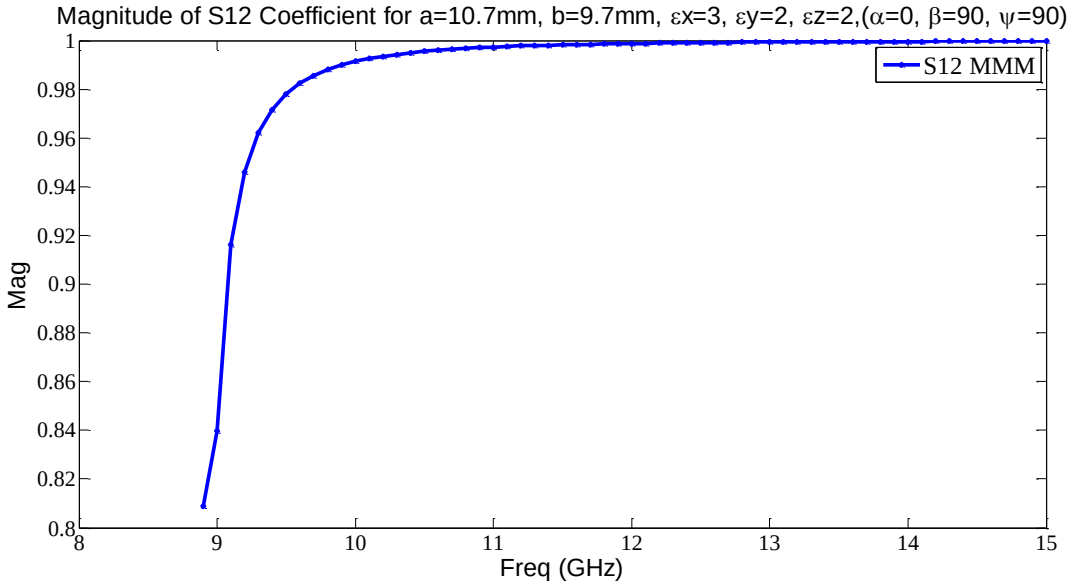

Figure 4.28 Magnitude of S_{12} coefficients of rotated medium with α=0, β=90, ψ=90 ($\boldsymbol{\epsilon_{11} = 3, \epsilon_{22} = 2, \epsilon_{33} = 2}$)

4.3.3.1 Comparison of MMM vs. FEM Results for α=0, β=90, ψ=90

Figure 4.29 through Figure 4.32 contain the comparison of MMM vs. FEM results for α=0, β=90, ψ=90

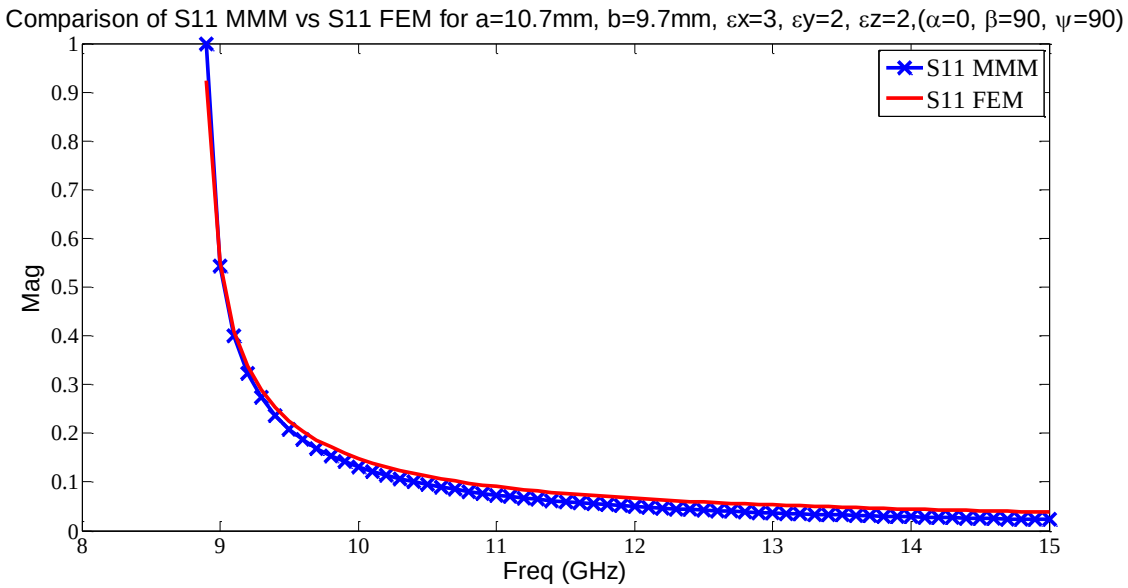

Figure 4.29 Magnitude of MMM vs FEM S_{11} coefficients of rotated medium with α=0, β=90, ψ=90 ($\boldsymbol{\epsilon_{11}=3,\epsilon_{22}=2,\epsilon_{33}=2}$)

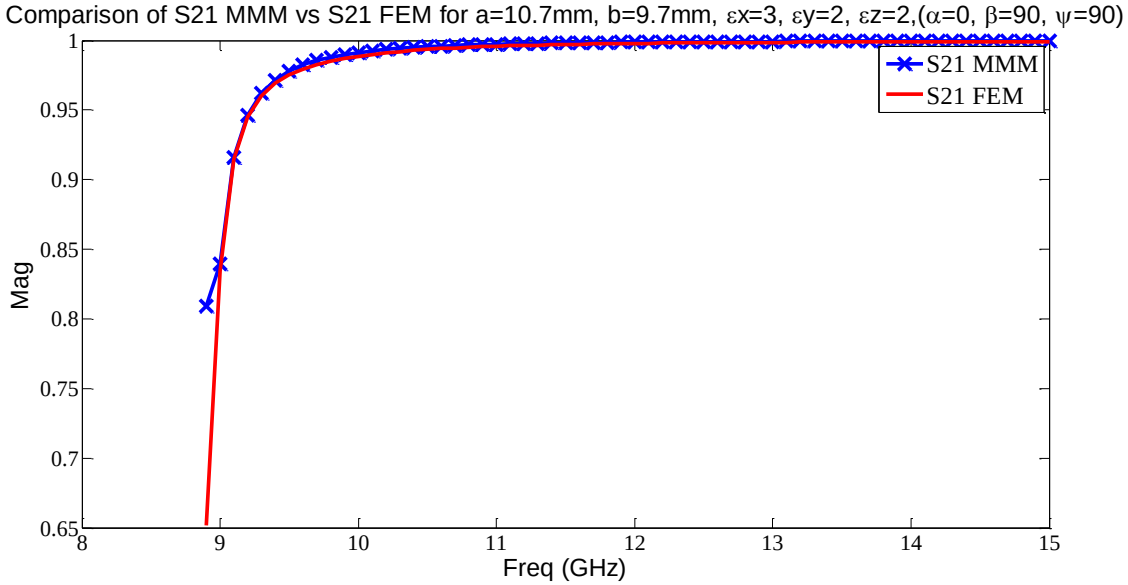

Figure 4.30 Magnitude of MMM vs. FEM S_{21} coefficients of rotated medium with α=0, β=90, ψ=90 ($\boldsymbol{\epsilon_{11}=3,\epsilon_{22}=2,\epsilon_{33}=2}$)

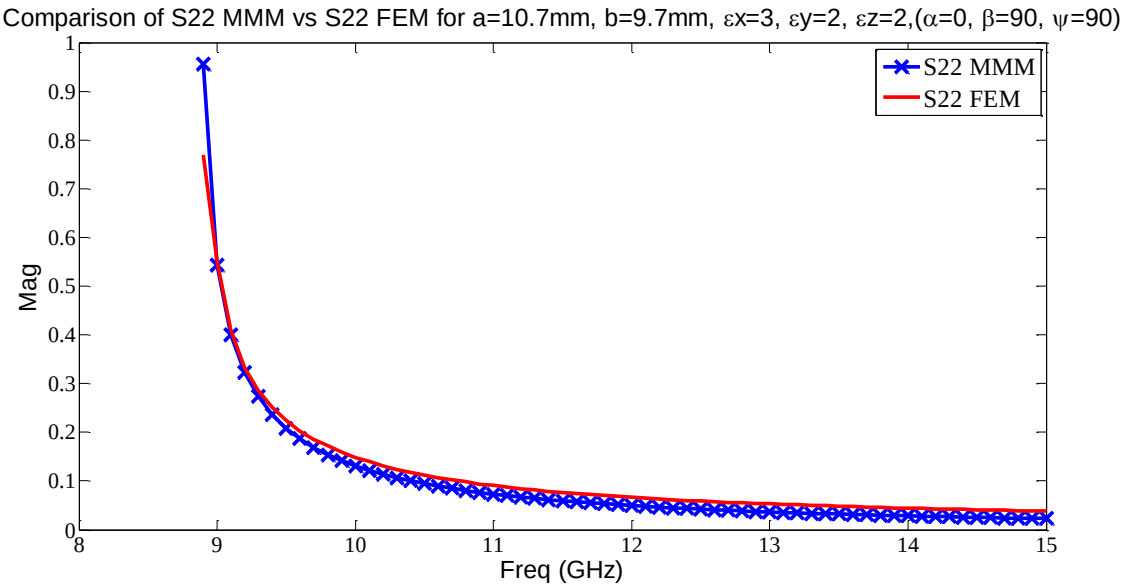

Figure 4.31 Magnitude of MMM vs. FEM S_{22} coefficients of rotated medium with α=0, β=90, ψ=90 ($\boldsymbol{\epsilon_{11} = 3, \epsilon_{22} = 2, \epsilon_{33} = 2}$)

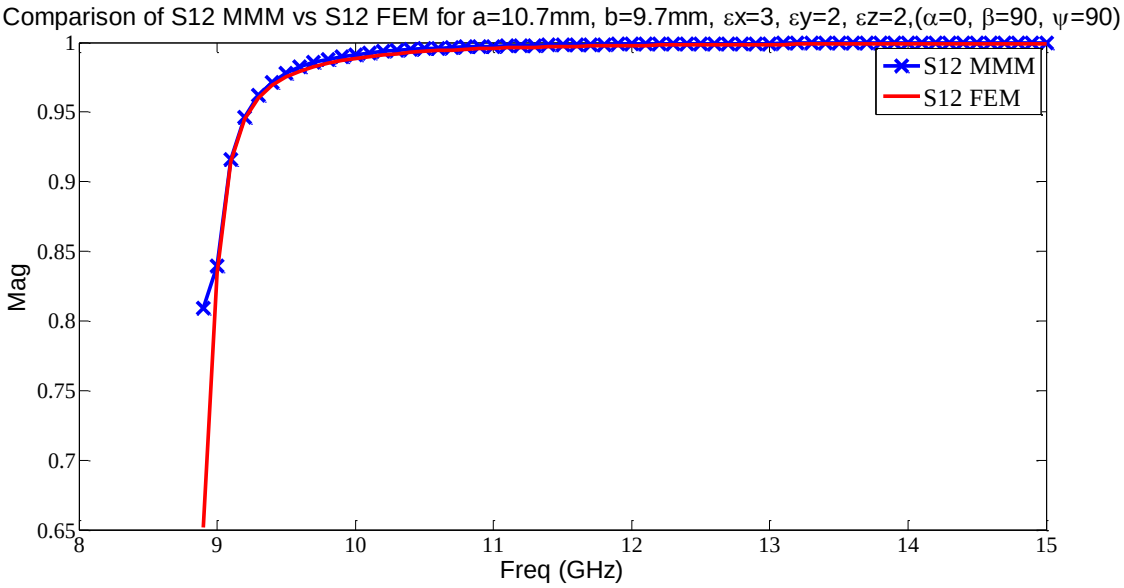

Figure 4.32 Magnitude of MMM vs. FEM S_{12} coefficients of rotated medium with α=0, β=90, ψ=90 ($\boldsymbol{\epsilon_{11} = 3, \epsilon_{22} = 2, \epsilon_{33} = 2}$)

4.4 Analysis of Centered Step Discontinuities in Waveguides Filled with Rotated Anisotropic Uniaxial Media

Again, it is still assumed that only TE_{m0} modes are present. Using the method of this section, and Section 2, numerical results for a centered step discontinuity in a waveguide filled with a

rotated medium are calculated. All analysis in the proceeding sections is based on the geometry of Figure 4.33. Axis alignment is the same as shown in Figure 4.6, Figure 4.15, and Figure 4.24, and the dielectric tensor is assumed to be the same as in Section 4.3.

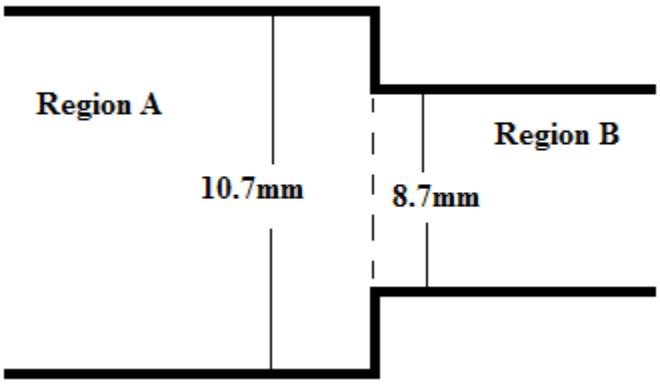

Figure 4.33 Geometry of a Centered Step Filled with Rotated Media

4.4.1 Comparison of MMM vs. FEM Results for Centered Step with $\alpha=0$, $\beta=0$, $\psi=0$

From Figure 4.34-Figure 4.37 one can see excellent agreement of MMM results compared to FEM results.

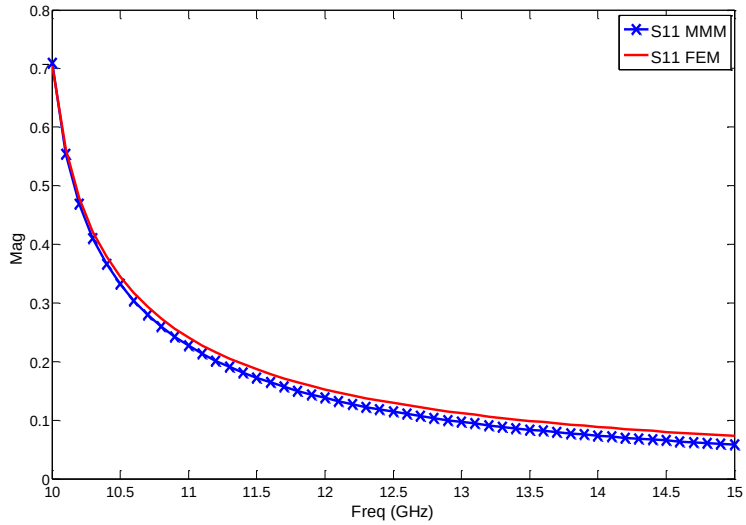

Figure 4.34 Magnitude of MMM vs. FEM S_{11} coefficients of rotated medium with α=0, β=0, ψ=0 ($\boldsymbol{\epsilon_{11} = 2, \epsilon_{22} = 2, \epsilon_{33} = 3}$)

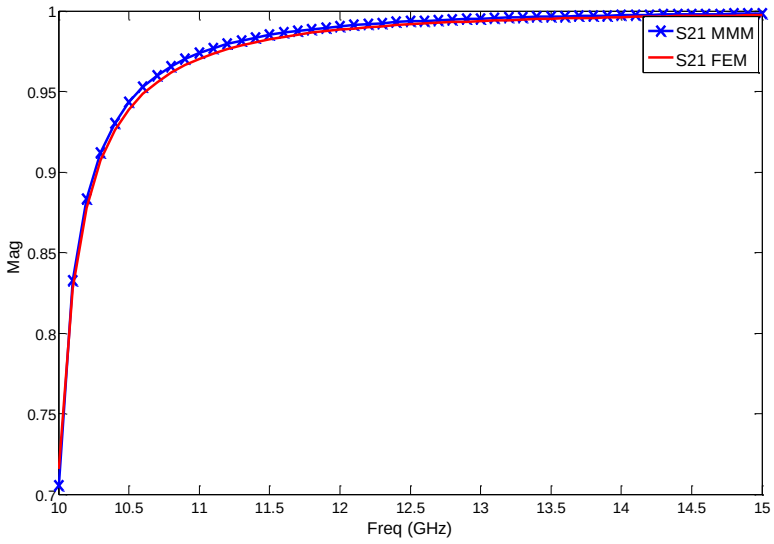

Figure 4.35 Magnitude of MMM vs. FEM S_{21} coefficients of rotated medium with α=0, β=0, ψ=0 ($\boldsymbol{\epsilon_{11} = 2, \epsilon_{22} = 2, \epsilon_{33} = 3}$)

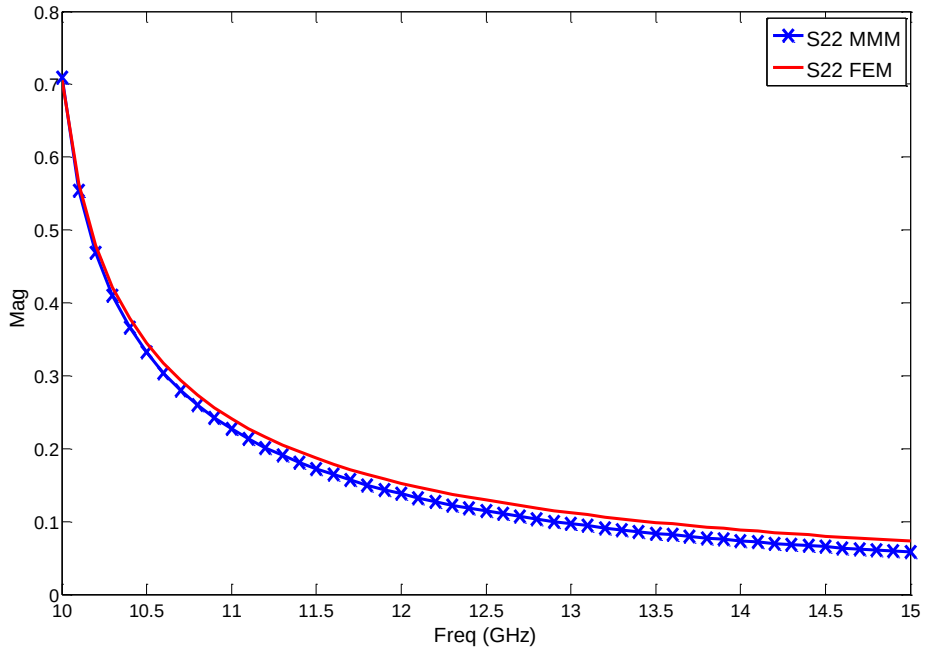

Figure 4.36 Magnitude of MMM vs. FEM S_{22} coefficients of rotated medium with α=0, β=0, ψ=0 ($\boldsymbol{\epsilon_{11} = 2, \epsilon_{22} = 2, \epsilon_{33} = 3}$)

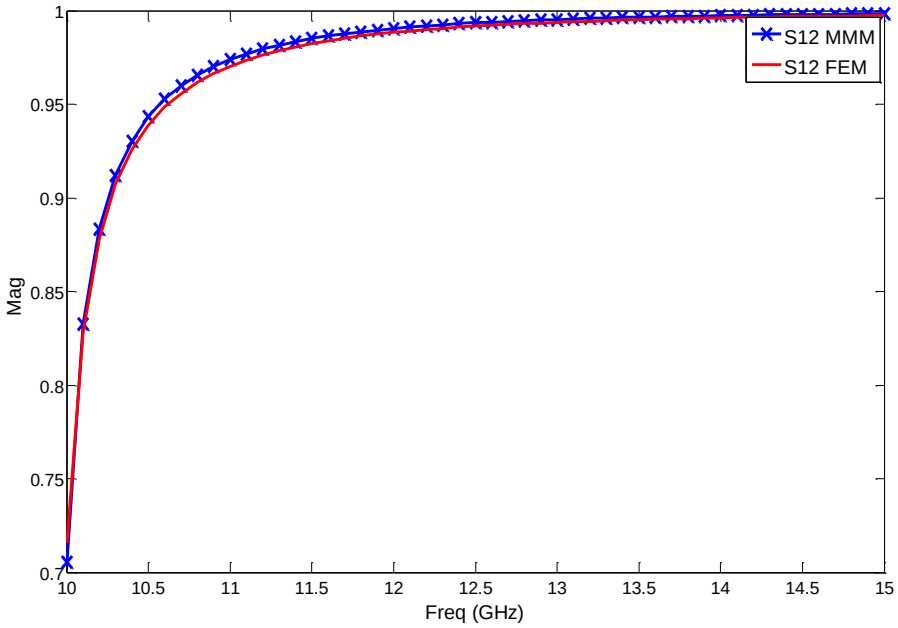

Figure 4.37 Magnitude of MMM vs. FEM S_{12} coefficients of rotated medium with α=0, β=0, ψ=0 ($\boldsymbol{\epsilon_{11} = 2, \epsilon_{22} = 2, \epsilon_{33} = 3}$)

4.4.2 Comparison of MMM vs. FEM Results for Centered Step with α=0, β=90, ψ=0

From Figure 4.38 through Figure 4.41 one can see excellent agreement of MMM results compared to FEM results for a rotated medium with α=0, β=90, ψ=0.

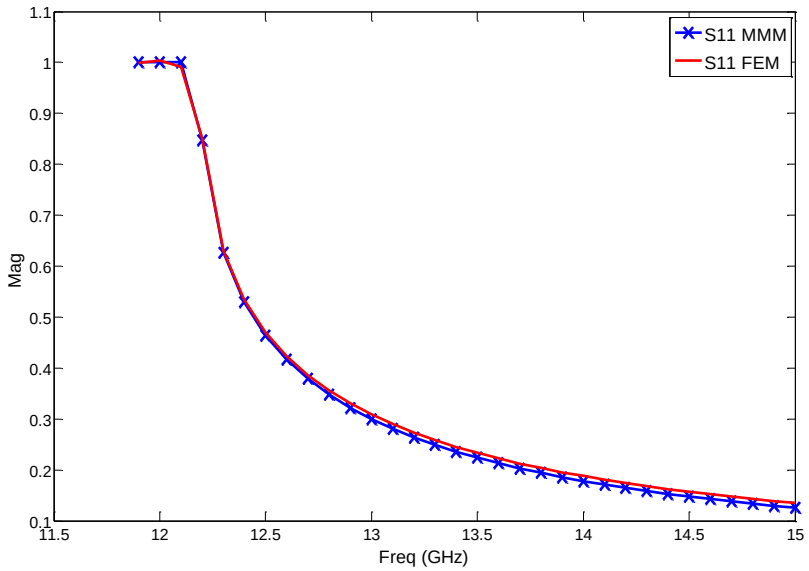

Figure 4.38 Magnitude of MMM vs. FEM S_{11} coefficients of rotated medium with α=0, β=90, ψ=0 ($\boldsymbol{\epsilon_{11} = 2, \epsilon_{22} = 3, \epsilon_{33} = 2}$)

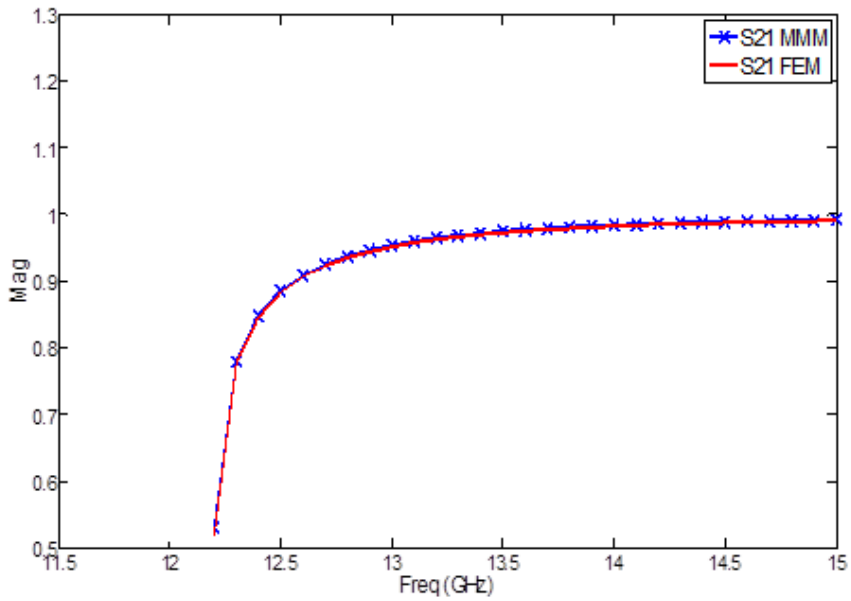

Figure 4.39 Magnitude of MMM vs. FEM S_{21} coefficients of rotated medium with α=0, β=90, ψ=0 ($\boldsymbol{\epsilon_{11} = 2, \epsilon_{22} = 3, \epsilon_{33} = 2}$)

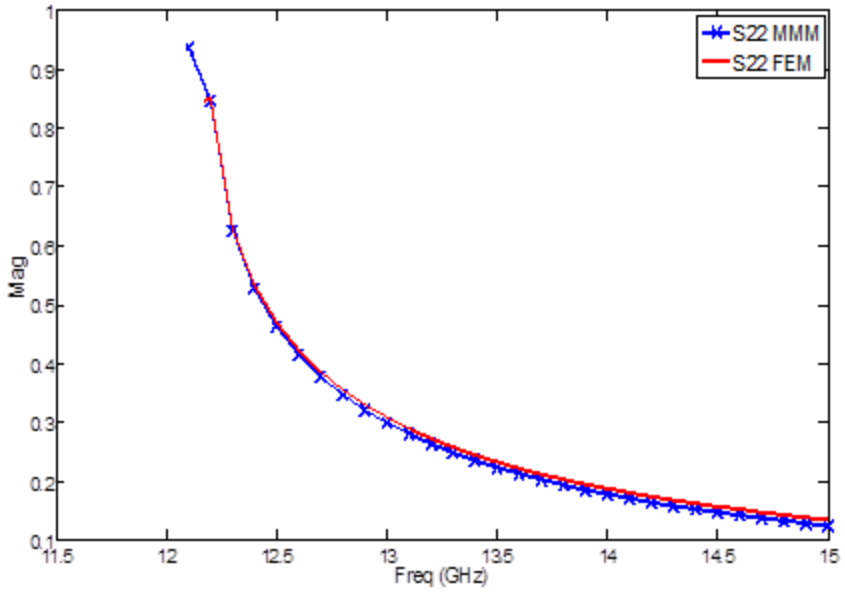

Figure 4.40 Magnitude of MMM vs. FEM S_{22} coefficients of rotated medium with α=0, β=90, ψ=0 ($\boldsymbol{\epsilon_{11} = 2, \epsilon_{22} = 3, \epsilon_{33} = 2}$)

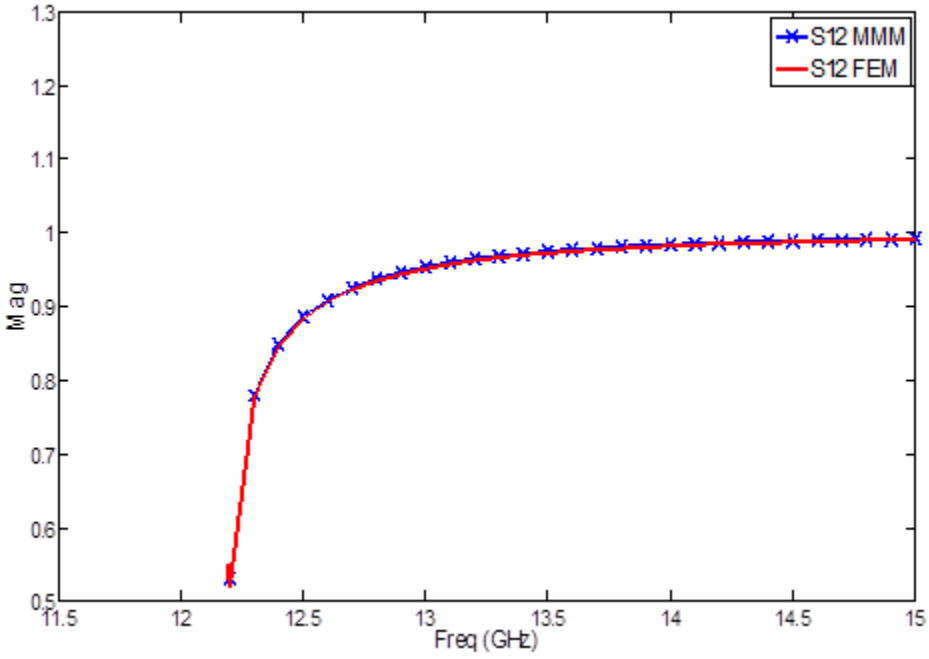

Figure 4.41 Magnitude of MMM vs. FEM S_{12} coefficients of rotated medium with α=0, β=90, ψ=0 ($\boldsymbol{\epsilon_{11} = 2, \epsilon_{22} = 3, \epsilon_{33} = 2}$)

4.4.3 Comparison of MMM vs. FEM Results for Centered Step with α=0, β=90, ψ=90

From Figure 4.42 through Figure 4.45 one can see excellent agreement of MMM results compared to FEM results for a rotated medium with α=0, β=90, ψ=90.

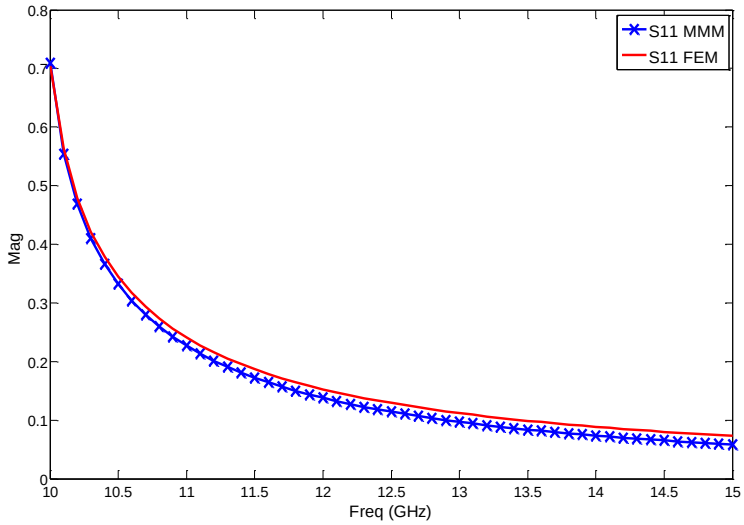

Figure 4.42 Magnitude of MMM vs. FEM S_{11} coefficients of rotated medium with α=0, β=90, ψ=90 ($\boldsymbol{\epsilon_{11} = 3, \epsilon_{22} = 2, \epsilon_{33} = 2}$)

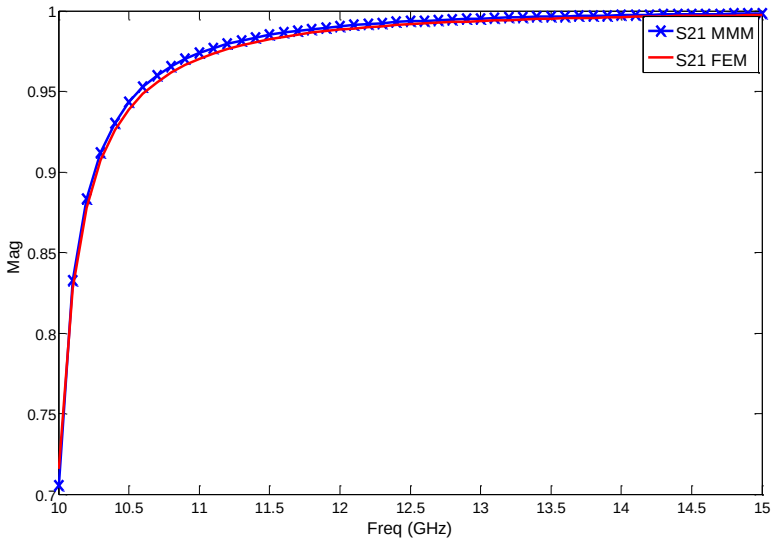

Figure 4.43 Magnitude of MMM vs. FEM S_{21} coefficients of rotated medium with α=0, β=90, ψ=90 ($\boldsymbol{\epsilon_{11} = 3, \epsilon_{22} = 2, \epsilon_{33} = 2}$)

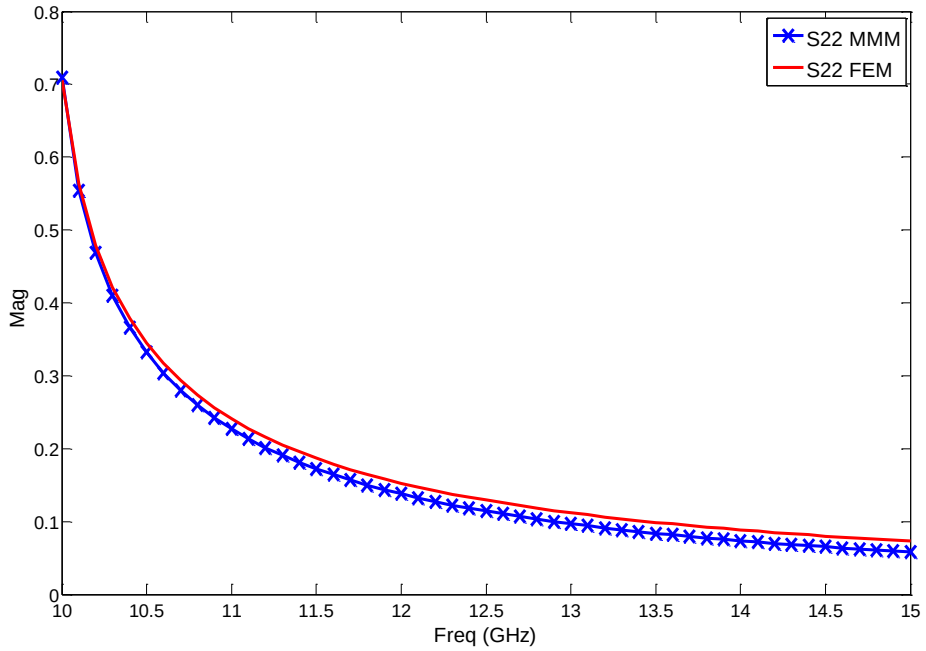

Figure 4.44 Magnitude of MMM vs. FEM S_{22} coefficients of rotated medium with α=0, β=90, ψ=90 ($\boldsymbol{\epsilon_{11} = 3, \epsilon_{22} = 2, \epsilon_{33} = 2}$)

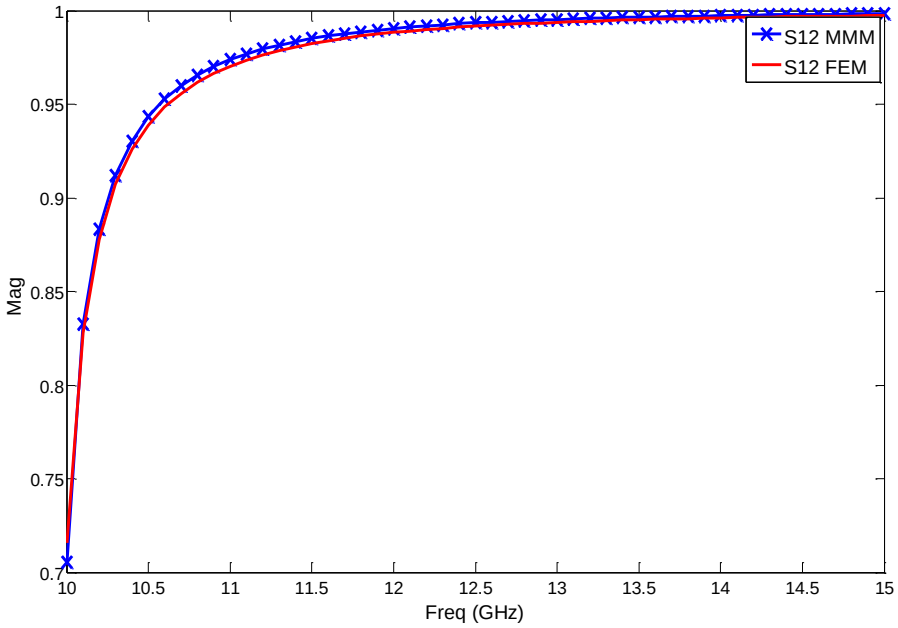

Figure 4.45 Magnitude of MMM vs. FEM S_{12} coefficients of rotated medium with α=0, β=90, ψ=90 ($\boldsymbol{\epsilon_{11} = 3, \epsilon_{22} = 2, \epsilon_{33} = 2}$)

4.5 Dispersion Relations for Lossy Dielectrics

In practice all dielectrics will exhibit some loss. Accounting for dielectric loss is necessary to give an accurate prediction of microwave device performance. In an isotropic medium Kong [39] defines the relative permittivity of a lossy isotropic medium by

$$\varepsilon_{cd} = \varepsilon + \frac{\sigma_d}{j\omega\,\varepsilon_0}, \tag{4.61}$$

where ε is the relative permittivity of the medium, σ_d is the conductivity of the dielectric, and ε_0 is the permittivity of free space. The conductivity of the dielectric is expressed as

$$\sigma_d = \omega\tau\varepsilon\varepsilon_0, \tag{4.62}$$

where in this thesis τ is the loss tangent of the medium. Now assume the permittivity of the lossy medium in an experimental coordinate system is of the form of (4.1). Equation (4.61) is now written as

$$\overline{\overline{\varepsilon_{cd}}} = \overline{\overline{\varepsilon_r}} - j\tau\overline{\overline{\varepsilon_r}} \tag{4.63}$$

for anisotropic medium or expanded as

$$\overline{\overline{\varepsilon_{cd}}} = \begin{bmatrix} \varepsilon_x - j\tau\varepsilon_x & 0 & 0 \\ 0 & \varepsilon_y - j\tau\varepsilon_y & 0 \\ 0 & 0 & \varepsilon_z - j\tau\varepsilon_z \end{bmatrix}. \tag{4.64}$$

If (4.64) is assumed to be diagonal in the experimental coordinate system, then the same methodology in (4.1)–(4.34) is used to represent this diagonal tensor in the laboratory coordinate system. In (4.29)–(4.34) ε_x is replaced with $\varepsilon_x - j\tau\varepsilon_x$, ε_y is replaced with $\varepsilon_y - j\tau\varepsilon_y$, and ε_z is replaced with $\varepsilon_z - j\tau\varepsilon_z$. Maxwell's Equations are now

$$\nabla \times H = j\omega\varepsilon_0\overline{\overline{\varepsilon_{cd}}}'E \tag{4.65}$$

$$\nabla \times E = -j\omega\mu_0 H \tag{4.66}$$

where $\overline{\overline{\varepsilon_{cd}}}'$ is the diagonal permittivity tensor of a lossy anisotropic medium after transformation from the experimental coordinate system to the laboratory coordinate system. Assuming uniaxial media with $\varepsilon_x = \varepsilon_y = \varepsilon$ and $\varepsilon_z = \varepsilon_z$ the same procedures used in (4.42)—(4.56) give us three dispersion relations for the most common alignments of the optic axis for media in the laboratory system.

4.5.1 Case 1 α=β=ψ=0

This case corresponds to the optic axis being parallel to the z-axis, and solving for k_z with H_z given by the previously assumed form we obtain, similar to (4.57),

$$k_z = -j\sqrt{k_x^2 - (\varepsilon_{22} - j\tau\varepsilon_{22})k_o^2}, \quad \varepsilon_{22} = \varepsilon \tag{4.67}$$

4.5.2 Case 2 α=0, β=π/2, ψ=0

This case corresponds to the optic axis being parallel to the y-axis, and solving for k_z with H_z given by the previously assumed form we obtain, similar to (4.58),

$$k_z = -j\sqrt{k_x^2 - (\varepsilon_{22} - j\tau\varepsilon_{22})k_0^2}, \quad \varepsilon_{22} = \varepsilon_z \tag{4.68}$$

4.5.3 Case 3 α=0, β=π/2, ψ= π/2

This case corresponds to the optic axis being parallel to the x-axis. Again solving for k_z with H_z given by the previously assumed form we obtain, similar to (4.59),

$$k_z = -j\sqrt{k_x^2 - (\varepsilon_{22} - j\tau\varepsilon_{22})k_o^2}, \quad \varepsilon_{22} = \varepsilon \tag{4.69}$$

5 Waveguide Step Discontinuities in Waveguides Filled with Embedded Metamaterials in Uniaxial Media

5.1 Metamaterial Background

Metamaterials are man-made materials that produce a negative ε and/or μ for a given frequency range. One area of research using metamaterials is in the area of cloaking devices. Another area applicable to waveguides is the use of metamaterials to form passbands below cutoff, form transmission nulls within the passband, and shift cutoff frequency altogether [47]—[50]. One way to produce a negative μ is through the use of split ring resonators (SRR). These resonators are fabricated and periodically spaced on a thin dielectric and inserted in a waveguide perpendicular to the H-fields as shown in Figure 5.1. Hrabar and others [50]—[57] show that by using this method one can design a waveguide with a passband below cutoff or a transmission null within the passband depending on the characteristics of the SRR. A passband below cutoff corresponds to a SRR resonant frequency below cutoff, and a transmission null corresponds to a SRR resonant frequency above cutoff.

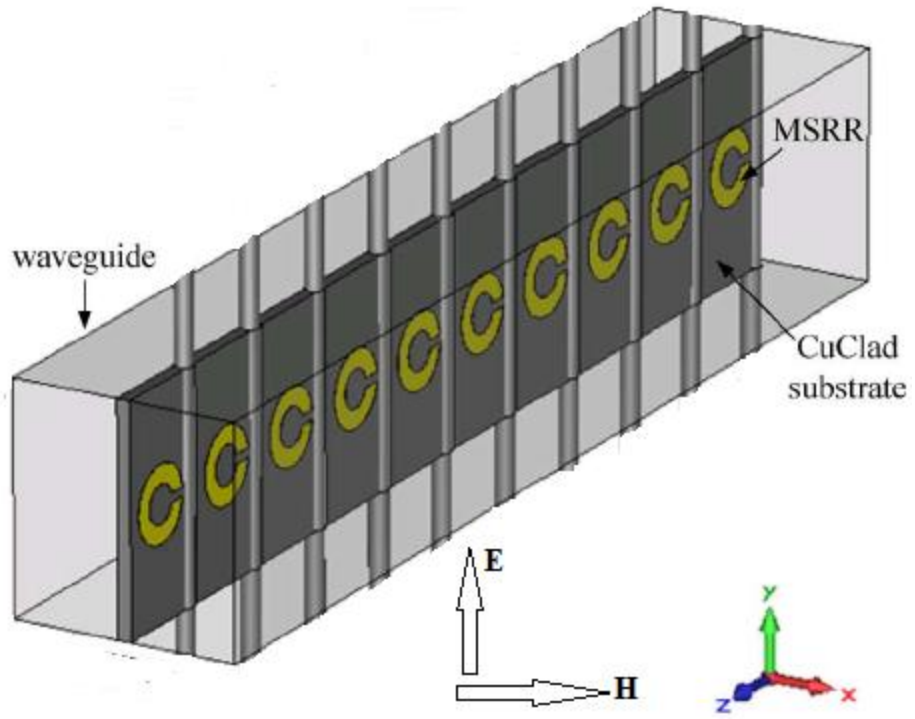

Figure 5.1 Split Ring Resonator Metamaterial. Graphic borrowed and modified from [51]

One commonly used method to produce a negative ε in a waveguide is to insert thin wires parallel to the E-field depicted in Figure 5.2. Each end of the wire is connected to the wall of the waveguide. It is shown that thin wires parallel to the E-field shift the cutoff frequency of the waveguide depending on wire diameter and spacing [55]−[56]. Hrabar [56]−[57] analyzes thin copper wire lattices in air filled waveguides and experimentally verifies the shift in cutoff frequency.

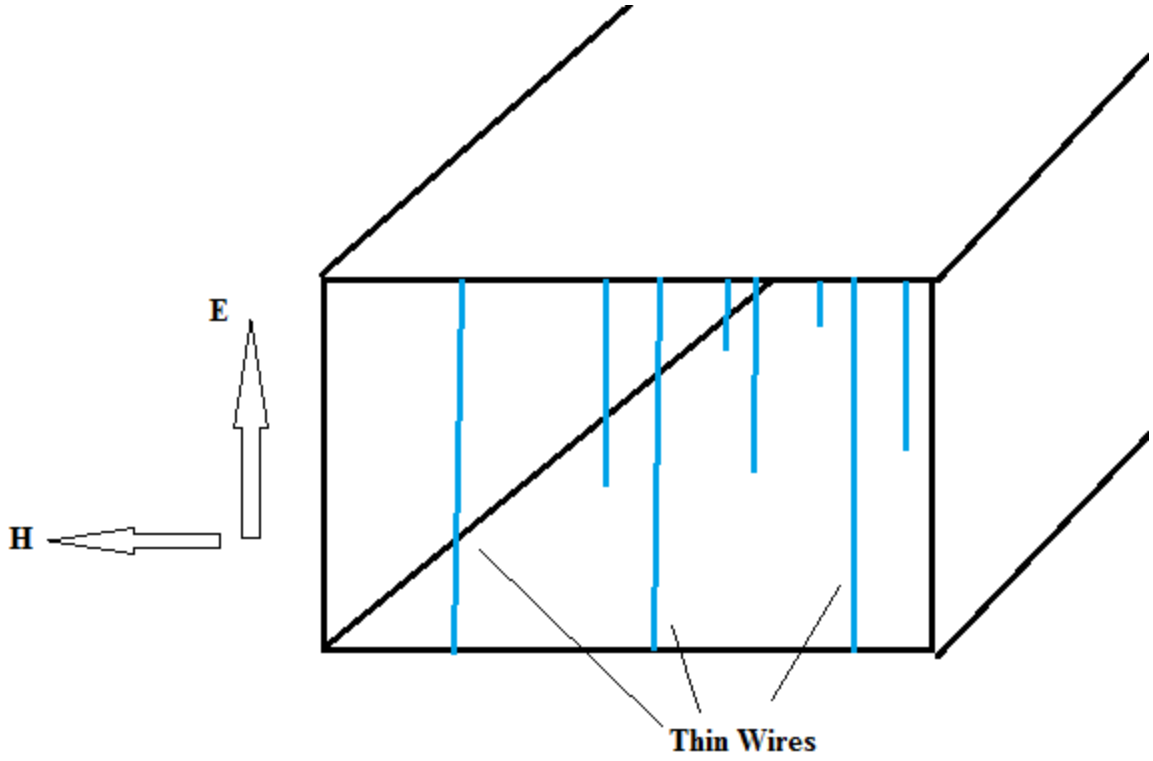

Figure 5.2: Thin Wire Metamaterial filled waveguide

5.1.1 Calculation of Metamaterial Properties

Hrabar [50] states that SRR produce a local magnetic field that is lower than the incident field. This leads to a negative magnetic polarization and negative effective permeability. He shows this effective permeability to be

$$\mu_{eff} = 1 - \frac{f_{mp}^2 - f_0^2}{f^2 - f_0^2 - j\gamma f} \quad 5.1$$

where f is the signal frequency, f_{mp} is the magnetic plasma frequency at which (in the lossless case) $\mu_{eff} = 0$, f_0 is the resonant frequency of the SRR, and Υ represents losses(1MHz based on Hrabar). Since parallel or longitudinal H-fields will not produce a current in the SRR the permeability tensor is defined as

$$\bar{\bar{\mu}} = \mu_0 \begin{bmatrix} \mu_{eff} & 0 & 0 \\ 0 & 1 & 0 \\ 0 & 0 & 1 \end{bmatrix} \quad 5.2$$

Using (5.2) and Maxwell's Equations Hrabar derives

$$k_z = \sqrt{\varepsilon_r \mu_{eff} \left(k_o^2 - \frac{k_x^2}{\varepsilon_r} \right)} \quad 5.3$$

where ε_r is the relative permittivity of an isotropic material, μ_{eff} is defined in (5.1), k_o^2 is the free space wavenumber, and $k_x = \frac{m\pi}{a}$. The sign of the right-hand side of (5.3) is chosen such that it has a negative imaginary part when μ_{eff} is assigned a negative imaginary part. Then, while retaining this chosen sign, the limit is taken as the imaginary part of μ_{eff} approaches zero. Assuming the fields have $e^{-j k_z z}$ dependence when k_z is real propagation will occur. Plots of the real part of k_z reveal the effects on propagation when SRR metamaterial is present. Figure 5.3 shows that when the resonance frequency of the SRR is designed below the cutoff frequency of the waveguide a real part of k_z exists. Normally, below cutoff k_z is purely imaginary corresponding to evanescent waves, but from Figure 5.3 we can see there is now a passband below the cutoff frequency of the waveguide. Similarly, in Figure 5.4 when the resonant frequency of the SRR is above the cutoff frequency of the waveguide, there is now a transmission null where k_z becomes purely imaginary.

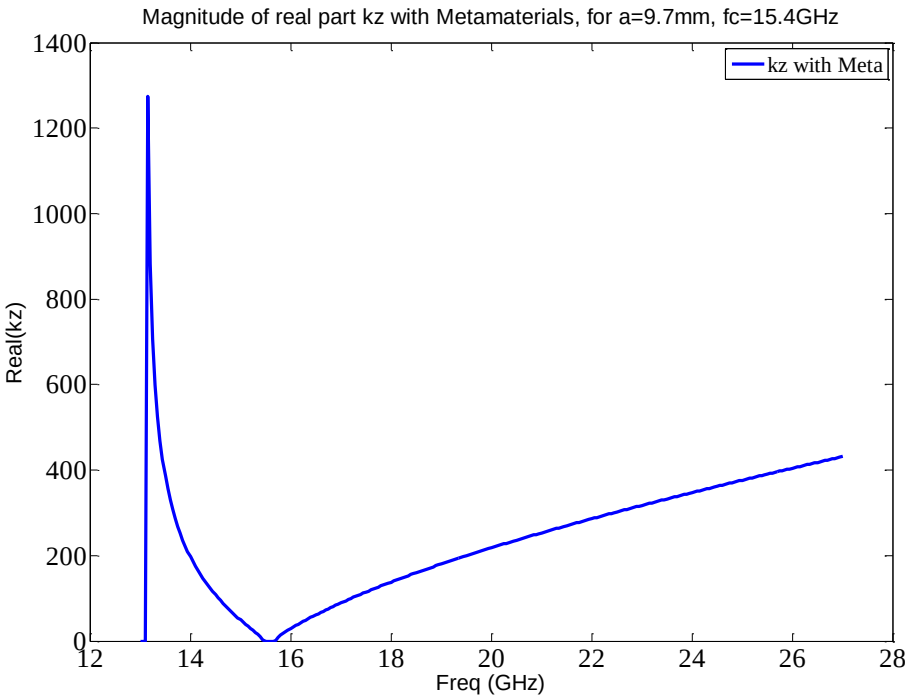

Figure 5.3 Real part of k_z when f_o of SRR is 13.1GHz

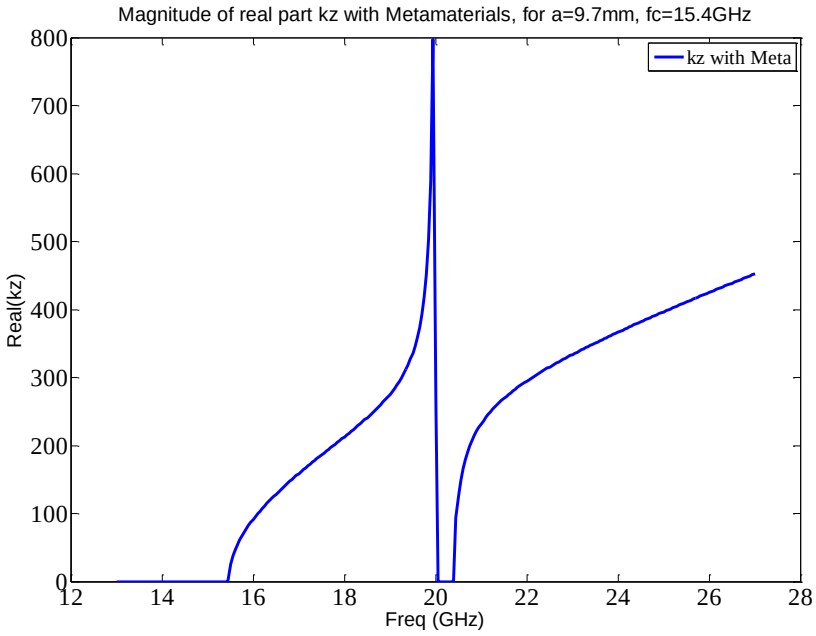

Figure 5.4 Real part of k_z when f_o of SRR is 20GHz

Inserting thin periodically spaced wires in a waveguide creates a uniaxial medium [58], and the permittivity tensor is given by

$$\bar{\bar{\varepsilon}}_{r\,meta} = \begin{bmatrix} \varepsilon' & 0 & 0 \\ 0 & \varepsilon' & 0 \\ 0 & 0 & \varepsilon_{meta} \end{bmatrix}, \tag{5.4}$$

and Nefedov's [58] definition for the permittivity of thin wires in a host medium is that of plasma medium. However, Nefedov fails to account for a loss term in plasma medium defined by Kong [39]. Assuming a loss term the permittivity of thin wire metamaterial is now

$$\varepsilon_{wire} = \varepsilon' \left(1 - \frac{\omega_p^2}{\varepsilon'(\omega^2 - j\omega\rho)}\right), \tag{5.5}$$

where

$$\rho = \frac{Nq^2}{\sigma_d m}, \tag{5.6}$$

where N is the total electron density in the wire material, q is electron charge of —1.6 x 10^{-19}C, m is the electron mass of 9.1 x 10^{-31}kg, and σ_d is defined from (4.62). In (5.5) ω_p^2 is defined by Pendry's method [55]

$$\omega_p^2 = \frac{2\pi c^2}{a^2 \ln(a/r)}\ , \tag{5.7}$$

and *c* is the speed of light, *a* is the distance between wires, and *r* is the wire radius. If we assume the host medium itself is uniaxial the permittivity tensor of a uniaxial media embedded with thin wire metamaterial is

$$\bar{\bar{\varepsilon}}_r = \begin{bmatrix} \varepsilon & 0 & 0 \\ 0 & \varepsilon & 0 \\ 0 & 0 & \varepsilon_z \left(1 - \frac{\omega_p^2}{\varepsilon_z(\omega^2 - j\omega\rho)}\right) \end{bmatrix} \tag{5.8}$$

Using the same methodology from Section 4 one can rotate the optic axis to align with an arbitrary unit vector in the laboratory coordinate system, and derive dispersion relations. From

[47] it is known that thin wire metamaterial must be parallel to the E-field to be effective. Assuming TE_{10} mode propagation in the z-direction with Case 2 ensures the E-field condition on the metamaterials is satisfied. The dispersion relation for embedded metamaterials gives k_z as

$$k_z = -j\sqrt{k_x^2 - \varepsilon_z\left(1 - \frac{\omega_p^2}{\varepsilon_z(\omega^2 - j\omega\rho)}\right)k_o^2} \quad 5.9$$

If the fields are assumed to have $e^{-jk_z z}$ dependence, wave propagation will occur when k_z is real. Illustrated in Figure 5.5, propagation in an air filled waveguide starts to occur at cutoff (~22.3GHz), but when thin wire metamaterial is inserted into the waveguide the negative permittivity causes the cutoff frequency to shift higher in frequency, as shown by the red curve. This is fundamentally different than simply shifting the cutoff frequency, because as ω goes to infinity ε_{wire} converges to ε of the media. It will be shown this allows for a shift in cutoff frequency without effecting performance characteristics of the waveguide at higher frequencies.

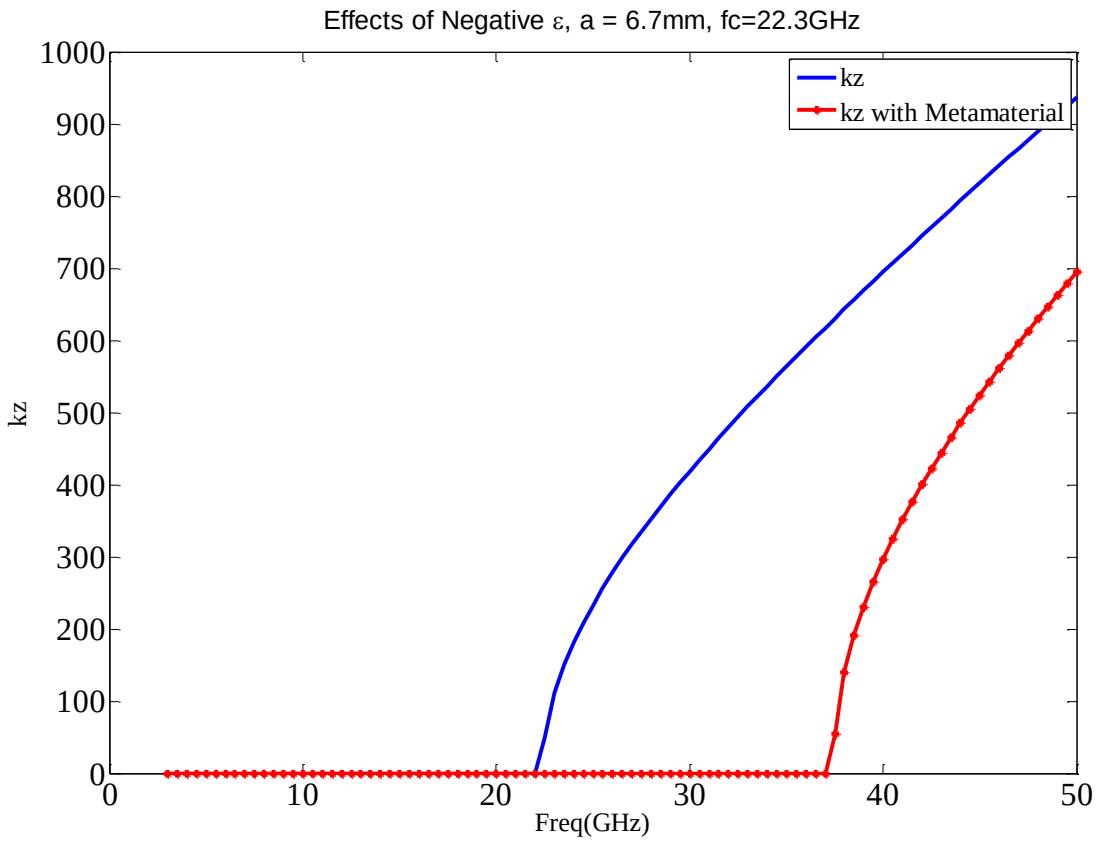

Figure 5.5 k_z of air filled waveguide vs. k_z of waveguide containing thin wire metamaterial. ε_r = 1, a=2.18mm, r=0.08mm

5.2 Metamaterials and Mode Matching Method

Mode matching using thin wire metamaterials will be discussed in this section because they allow for easy manufacturing and testing. Although SRR metamaterial is not discussed in this section its analysis with the MMM is carried out in the same manner as thin wire metamaterial. Mode matching using thin wires is done in the exact same manner as in an air filled waveguide or uniaxial media filled waveguide, but using (5.9) for k_z. In Figure 5.6 the dimensions of the step discontinuity, wire radius, and wire spacing are given. Figure 5.7 and Figure 5.8 contain the MMM results. One can see that in a waveguide step discontinuity filled with a uniaxial

media the waveguide's cutoff is around 9GHz. However, if thin wires of diameter 0.127mm and spacing distance of 5.46mm are embedded in the uniaxial media, the waveguide's cutoff shifts to around 14GHz. A box with length *2d* and a wire in the center is referred to as a unit cell of metamaterial.

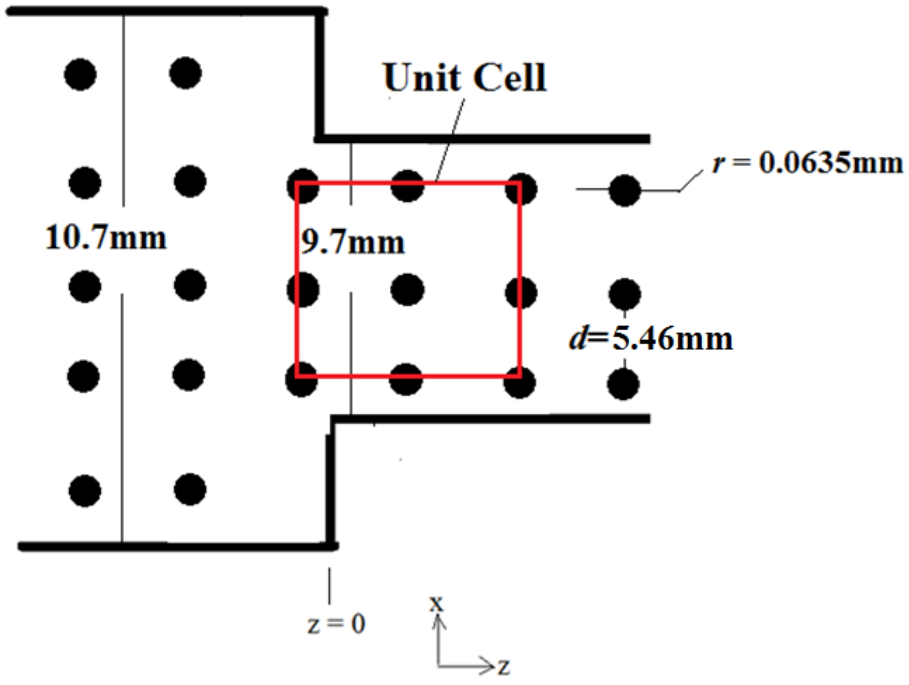

Figure 5.6 Dimensions of step discontinuity filled with uniaxial media with embedded metamaterial with a=10.7mm, c=9.7mm, $\varepsilon_{11}=\varepsilon_{22}=2$, $\varepsilon_{33}=3$, r=0.0635mm, and d=5.46mm.

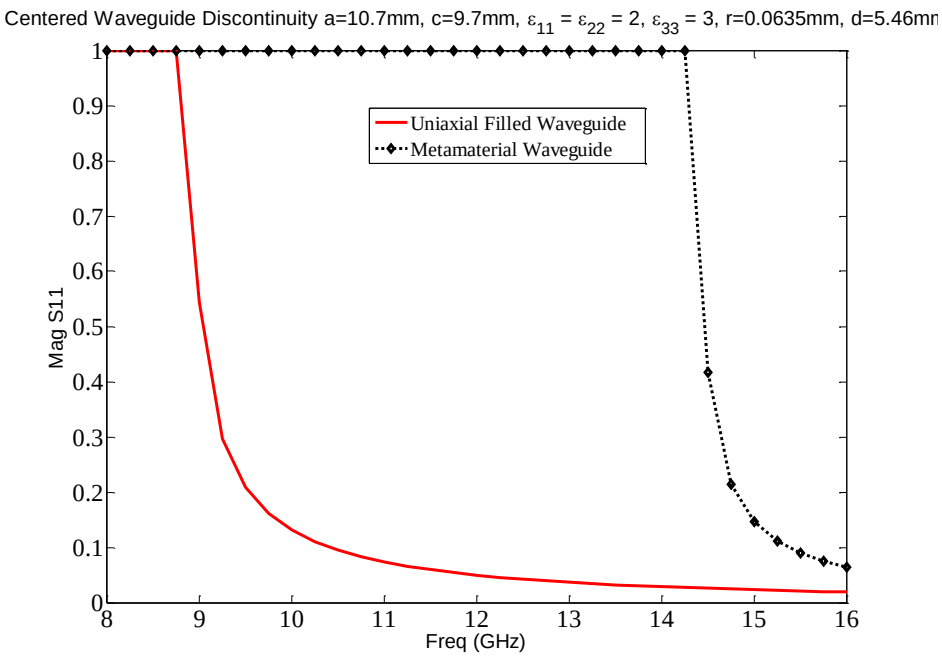

Figure 5.7 Waveguide reflection coefficients (S11) for uniaxial media with embedded metamaterial with a=10.7mm, c=9.7mm, $\varepsilon_{11}=\varepsilon_{22}=2$, $\varepsilon_{33}=3$, r=0.0635mm, and d=5.46mm.

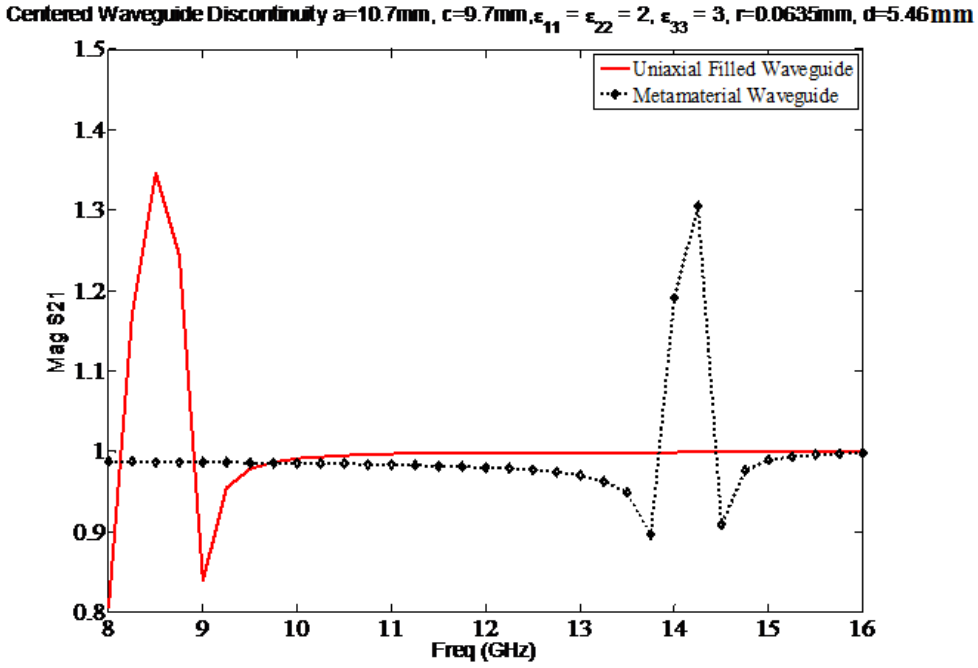

Figure 5.8 Waveguide transmission coefficients (S21) for uniaxial media with embedded metamaterial with a=10.7mm, c=9.7mm, $\varepsilon_{11}=\varepsilon_{22}=2$, $\varepsilon_{33}=3$, r=0.0635mm, and d=5.46mm.

6 Filter Theory, Design and Fabrication

This section will discuss the design of two waveguide filters. One waveguide is a filter fabricated on Dielectric laboratories CG material, and a second identical filter is embedded with thin wire metamaterial. Analysis is carried out with MMM, and results are compared with commercial full wave solvers and measured results.

6.1 Initial Filter Design

Hong and Lancaster [59] derive the theory for band-pass filter design based on ideal coupling coefficients. The coupling coefficients are calculated from filter *g* values. For a desired filter order Hong and Lancaster list the *g* values as

$$g_o = 1 \tag{6.1}$$

$$g_1 = \frac{2}{\gamma}\sin\frac{\pi}{2n} \tag{6.2}$$

$$g_i = \frac{1}{g_{i-1}}\frac{4\sin\left(\frac{(2i-1)\pi}{2n}\right)\sin\left(\frac{(2i-3)\pi}{2n}\right)}{\gamma^2+sin^2\left(\frac{(i-1)\pi}{n}\right)} \text{ for } i = 2,3,\ldots, n, \tag{6.3}$$

and

$$g_{n+1} = \begin{cases} 1 \; for \; n \; odd \\ \coth^2\frac{\beta}{4} \; for \; n \; even \end{cases} \tag{6.4}$$

where

$$\gamma = \sinh\frac{\beta}{2n} \tag{6.5}$$

and

$$\beta = \ln\left(\coth\frac{L_{AR}}{17.37}\right) \tag{6.6}$$

and

$$L_{AR} = -10\log(1 - 10^{0.1RL}). \quad 6.7$$

In (6.7) *RL* is the desired passband return loss level in dB. Once the g values are calculated using (6.1)—(6.5) the ideal coupling coefficients are calculated and filter design can begin.

$$M_{i,i+1} = \frac{FBW}{\sqrt{g_i g_{i+1}}} \textit{ for i= 1 to n-1} \quad 6.8$$

where $M_{i,i+1}$ are the coupling coefficients between adjacent resonators.

In (6.8) *FBW* is the fractional bandwidth of the filter. Using the MMM a castellation of step discontinuities is analyzed. By adjusting the dimensions *c* and *d* in Figure 6.1 coupling coefficients are calculated.

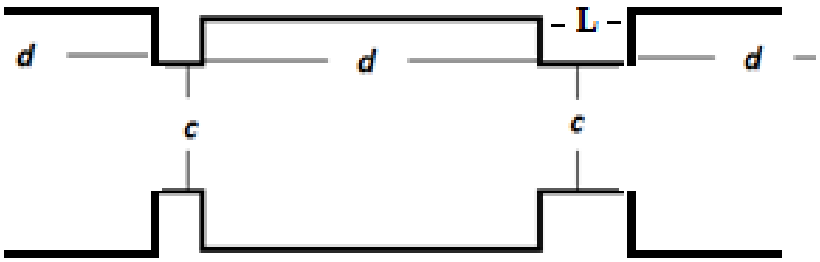

Figure 6.1 Castellation of waveguide step discontinuities.

Mode matching analysis of the junction in Figure 6.1 will provide two distinct resonances in frequency knowing that the coupling coefficients are also calculated using

$$k = \frac{f_2^2 - f_1^2}{f_2^2 + f_1^2} \quad 6.9$$

where f_2 is the higher resonance peak and f_1 is the lower resonance peak. Comparing the k value results of the MMM with the ideal coupling coefficients provides a starting point for filter design.

6.2 Filter Design and Results

A three pole, n=3, filter with a center frequency of 32.5GHz, bandwidth of 6%, and return loss of -35dB will be used for the filter design. The dielectric used is a CG material donated by Dielectric Laboratories. It has $\varepsilon_{11}=\varepsilon_{22}=67.1$ and a different ε_{33} of 63. Using (6.1)—(6.8) provides coupling coefficients of $M_{12}=M_{23}=0.1047$. In this case, the optic axis alignment is that of Case 2 from Section 4, and with the MMM, a structure similar to Figure 6.1 is analyzed with the larger waveguide having a width of 0.9144mm and L is set at 0.127mm to accommodate manufacturing processes. By varying *c* and *d* coupling coefficients are calculated and plotted in Figure 6.2 for Case 1 through Case 3 and isotropic case. One can see from the coupling coefficients that if uniaxial media is unaccounted for the filter's f_c and bandwidth will be drastically affected.

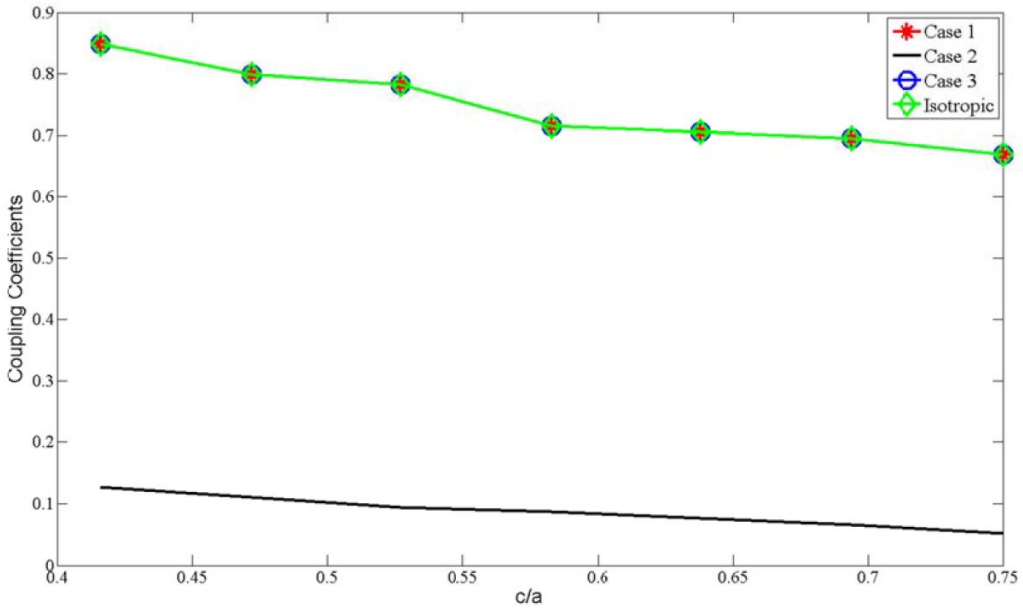

Figure 6.2 Coupling coefficients for varying *c* distances for d=1.2mm.

Using the coupling coefficients, proper distances and gaps are selected for an initial filter starting point. A distance of d=1.213mm and c=0.482mm were used to give a k of (6.9) value close to 0.1047. After some tuning the final dimensions of the filter had d=1.245mm and c=0.432mm. The first and last sections' lengths were optimized to improve return loss. Figure 6.3 lists the dimensions of the final filter, and Figure 6.4 compares the MMM results with commercial FEM results.

Figure 6.3 Dimensions of final filter.

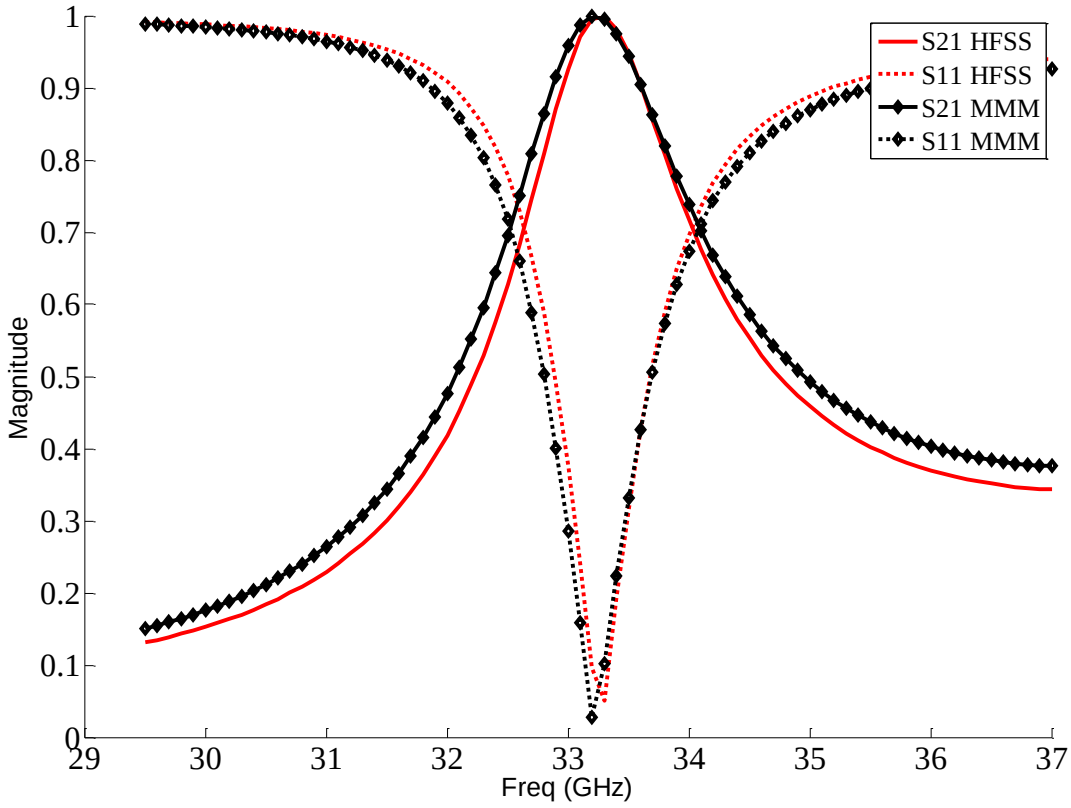

Figure 6.4 MMM filter results (black dotted) vs. FEM filter results.

6.2.1 Filter Excitation

Exciting the waveguide filter with a TE_{10} wave is important because all analytical results are based on this assumption. Excitation methods are also important because it is how the filter connects to an external circuit. One of the more popular excitation techniques is using a tapered microstrip line to excite the filter [60]—[65]. The filter's dimensions are finalized, after the optimization of the taper is carried out with the MoM solver from Sonnet software [66].

6.2.2 Filter Results

Figure 6.5 shows the finalized filter after optimization of the excitation lines. The measured results are compared with the simulated MMM results in Figure 6.6. The filter has a VSWR of 2:1 or better from 31.6-33.8GHz, with a center frequency of 32.68GHz. The insertion loss is 6dB or better in this band. Figure 6.7 shows the manufactured filter above the word liberty on a USA penny for a size comparison.

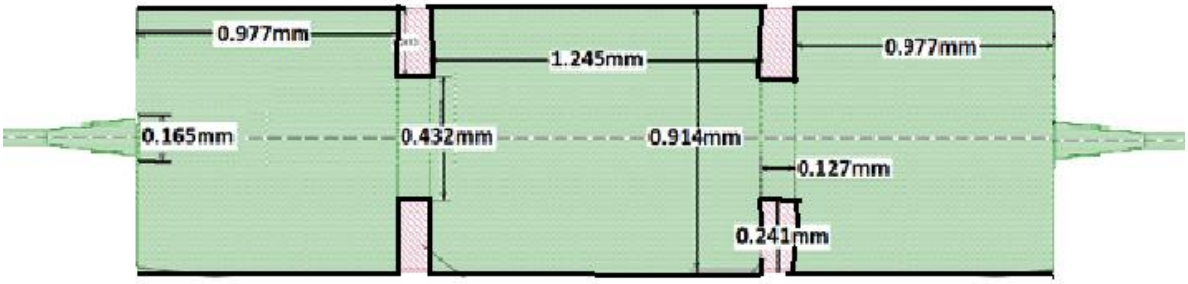

Figure 6.5 Dimensions of final filter with taper optimization.

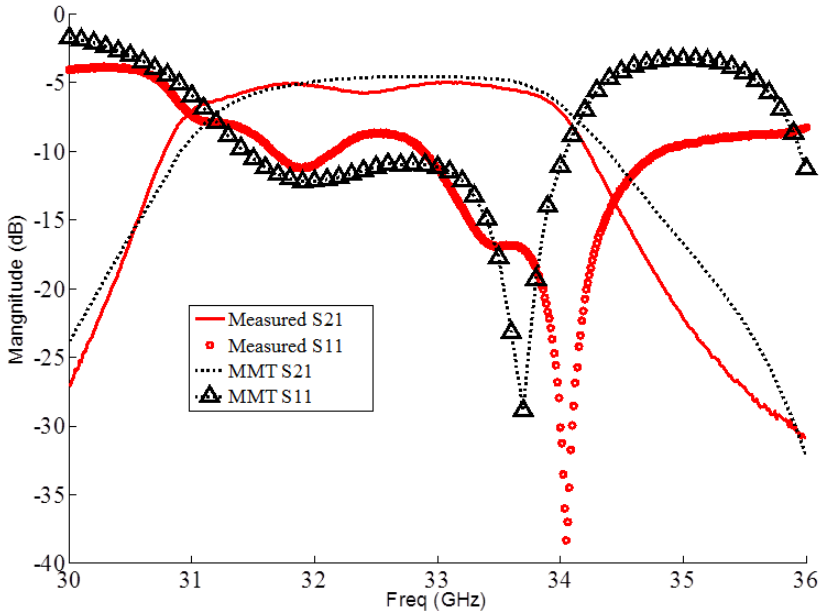

Figure 6.6 Measured filter results vs. MMM results.

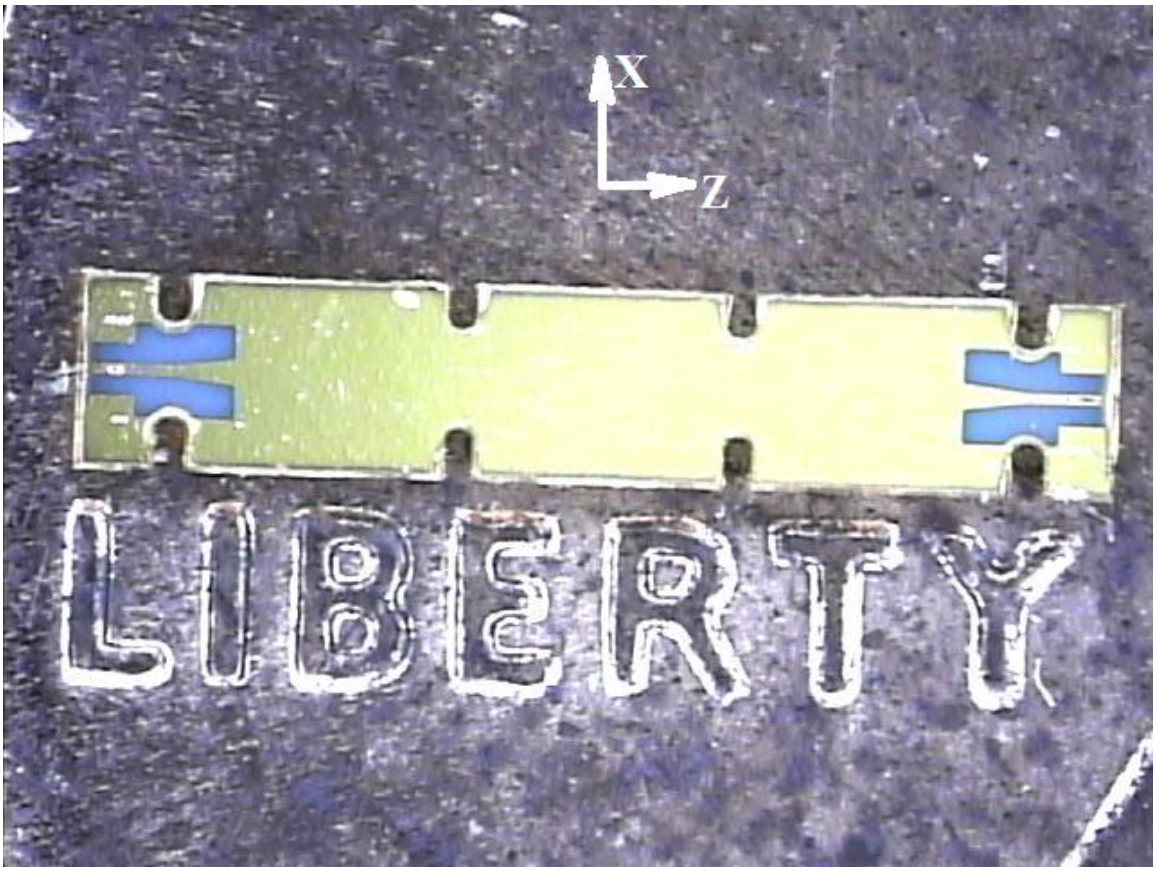

Figure 6.7 Manufactured filter next to the word liberty on a USA penny for size comparison

6.3 Filter Design with Metamaterial

Using the filter of Section 6.2 we wish to shift the cutoff frequency into the stopband of the filter using thin wire metamaterial. This has the benefit of increasing the stop band region on the lower side of the filter. Manufacturing processes limit the diameter of the wire to around $\lambda/9$. Using this diameter limits the smallest spacing of wire to around 2.1mm before cutoff is shifted into passband. Starting with the simplest case of one unit cell overlap with the filter corresponds to a spacing of 2.48mm as shown in Figure 6.8. Theory predicts that the start of transmission shifts from 20 GHz to 25.3GHz when there is metamaterial embedded into the filter. Looking at Figure 6.9, one sees that the original transmission peak is now suppressed in

value because it is shifted into the start of the filters lower rejection band. It will be shown later these MMT results agree well with measured results. The embedded metamaterial filter results using the MMM are in Figure 6.9. The use of ε_{wire} in the dispersion relation is based on theory and does not account for parasitic couplings; this explains the difference in bandwidth.

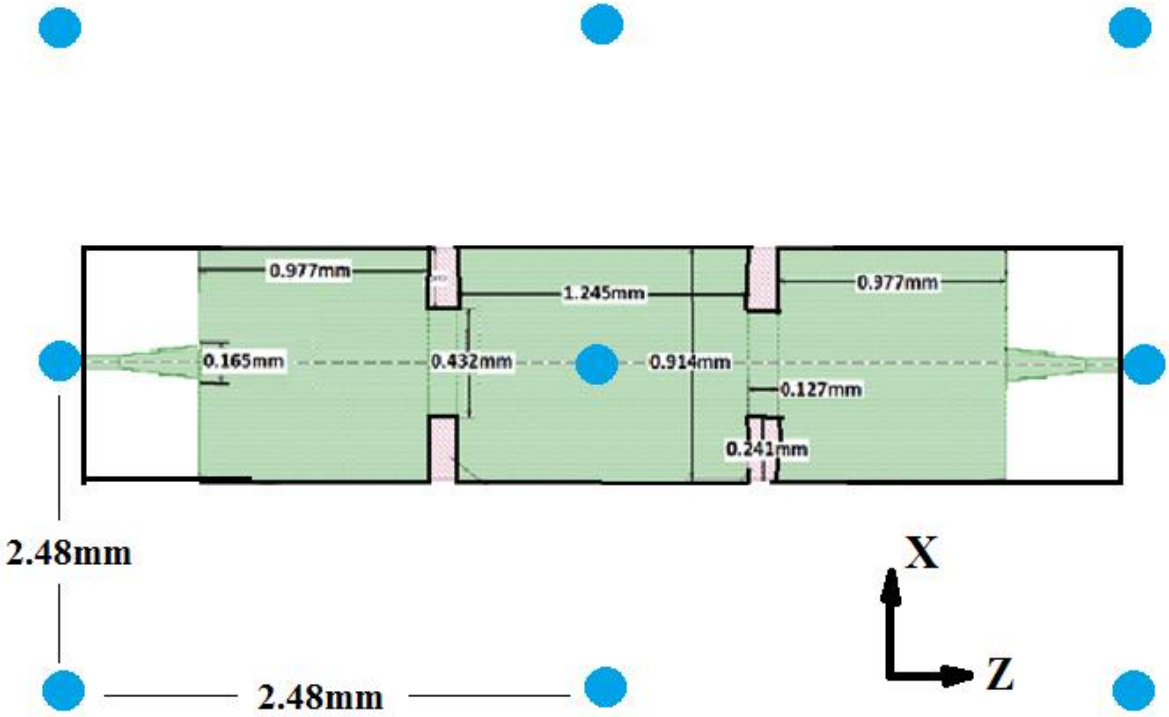

Figure 6.8. Filter with embedded thin wire metamaterial.

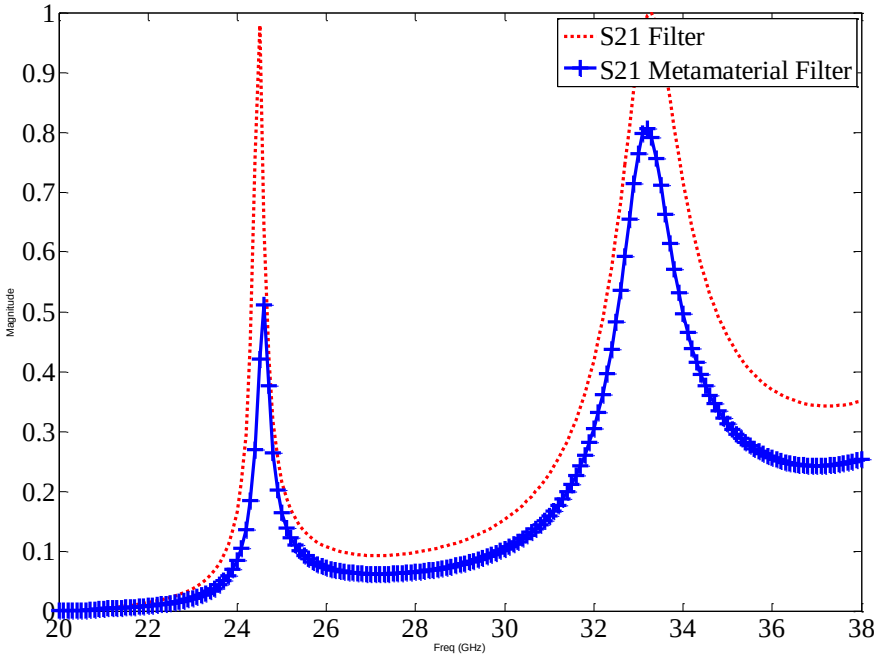

Figure 6.9. Response of filter with and without embedded metamaterial, using the MMM.

6.3.1 Metamaterial Filter Results

Figure 6.10 shows the manufactured filter with the embedded thin wire metamaterial. In Figure 6.11 one can clearly see that the cutoff frequency has shifted, and is no longer around 20GHz. Measured results also verify that the MMM verified a reduction of bandwidth due to embedded metamaterials, which supports the reduction of bandwidth in Figure 6.9. Again, the filter has a VSWR of 2:1 or better from 31.6-33.8GHz, with a center frequency of 32.68GHz, and insertion loss of 6dB or better in this band.

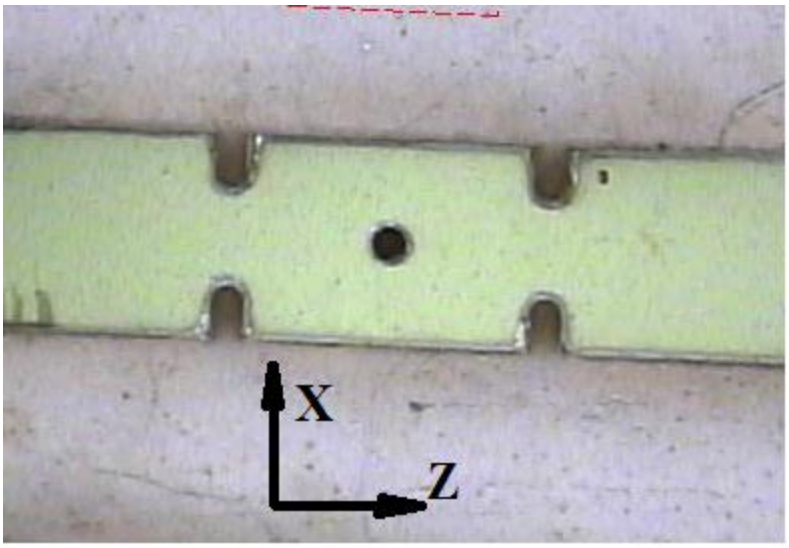

Figure 6.10. Manufactured filter with embedded metamaterial.

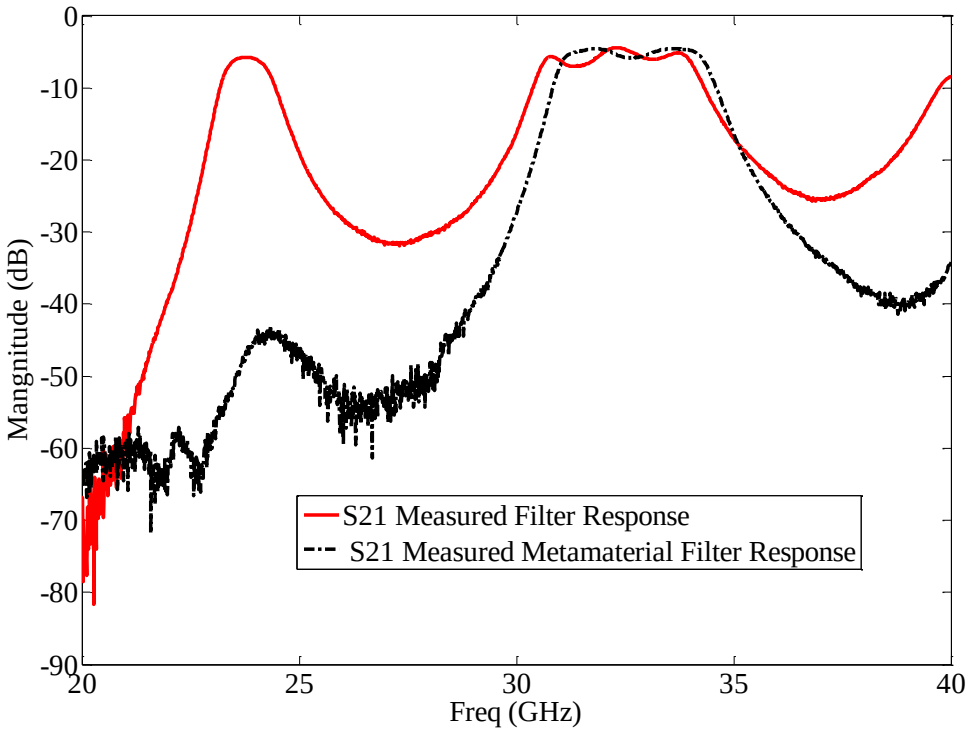

Figure 6.11. Measured results of filter vs. filter with embedded metamaterial.

7 Conclusion

Much work covers the analysis of waveguide discontinuities and waveguide filters. There are numerous numerical techniques to analyze the performance of waveguide filters. As previously stated the mode matching method (MMM) provides advantages over other methods for analyzing waveguide type problems. Although the MMM has been around since the 1960s lossy uniaxial media with a rotated optic axis has never been accounted for in its analysis. Most dielectrics exhibit some sort of uniaxial nature, and at higher frequencies even some isotropic dielectrics behave uniaxial by accounting for this anisotropic behavior in dielectrics, specifically uniaxial media, is extremely important in the design phase of filters, because the coordinate system of the uniaxial media and coordinate system of the waveguide system under analysis are not always necessarily the same. If the uniaxiality is not factored into analysis, the center frequency and bandwidth of the manufactured filter can vary drastically from the theoretical or simulated performance as shown by the difference in coupling coefficient values.

Although analysis of a completely arbitrarily rotated optic axis is complex, this work demonstrates for 3 special cases analysis provides a closed form expression for the dispersion relation, which is fundamental in the MMM analysis. These 3 cases are of interest because most bulk dielectrics used to fill waveguides or manufacture substrate integrated waveguides (SIW) exhibit a uniaxial behavior at microwave frequencies common to the 3 aforementioned cases.

The work also demonstrates that MMM when compared with commercially available EM full-wave solvers provides accurate results. This work also takes advantage of port extension theory to reduce the number of computational steps needed to provide results of the filter.

Although computational power and memory are very powerful in this day and age any reduction in computational time is still an advantage and reduces analysis time.

Metamaterials recently became a hot topic of research, as well as, their analysis when incorporated into microwave devices. The results show that the MMM provides accurate analysis of waveguide filters with uniaxial media that contain embedded metamaterials. Much literature analyzes the theoretical and measured results of metamaterials, but the MMM has never been used to analyze embedded metamaterials. Analysis of metamaterials embedded in uniaxial media to the best of the author's knowledge has never been analyzed with the MMM. To the best of the authors knowledge again, the MMM is the only method, aside from creating a full 3D model in an EM solver, that provides accurate analysis results of waveguide filters made with embedded thin wire metamaterial in a uniaxial media. Using the presented idea of a metamaterial unit cell the MMM can easily analyze embedded thin wire metamaterials. The MMM when applied to metamaterials provides a huge reduction in analysis time when compared to the setup time needed to analyze metamaterials in a full wave EM solver environment.

The MMM results are then compared to results of manufactured dielectric filled waveguide filters manufactured with a high ε uniaxial High Temperature Co-fired Ceramic (HTCC). The MMM provides results that agree well with measured results. A manufactured filter was also constructed with embedded thin wire metamaterial. The MMM results again provided results that agreed with measurements.

The MMM is a robust analytical method that allows for the analysis of waveguide filters or waveguide filters filled with uniaxial media. It also can accurately predict performance of filters containing embedded metamaterials. Future work will continue to expand the method to more complex structures, degenerate excitation, and newly emerging metamaterials.

References

[1] A. Wexler, “Solution of Waveguide Discontinuities by Modal Analysis,” *IEEE Trans. Microwave Theory Tech.,* Vol. 15, No. 9, pp. 508–517, Sept. 1967.

[2] T. Itoh, *Numerical techniques for microwave and millimeter-wave passive structures*. John Wiley & Sons, USA. 1989.

[3] R. Mittra and S. W. Lee, *Analytical techniques in the theory of guided waves*. The Macmillan Company, New York, NY, 1971, pp. 30-61.

[4] R. Safavi-Naini and R. H. MacPhie, “On Solving Waveguide Junction Scattering Problems by the Conservation of Complex Power Technique,” *IEEE Trans. On MTT.,*Vol. 29, No. 4, pp. 337–343, April 1981.

[5] P. Jarry and J. Beneat, *Advanced DesignTechniques and Realizations of Microwave and RF Filters*. John Wiley & Sons. USA. 2008, pp. 328–337.

[6] T. S. Chu, et al., “Comparative Study of Mode-Matching Formulations for Microstrip Discontinuity Problems,” *IEEE Trans. On MTT.,*Vol. 33, No. 10, pp. 1018–1023, Oct. 1985.

[7] H. Patzelt and F. Arndt, “Double-Plane Steps in Rectangular Waveguides and their Application for Transformers, Irises, and Filters,” *IEEE Trans. On MTT.,*Vol. 30, No. 5, pp. 771–776, May 1982.

[8] U. Papziner and F. Arndt, “Field Theoretical Computer-Aided Design of Rectangular and Circular Iris Coupled Rectangular or Circular waveguide Cavity Filters,” *IEEE Trans. On MTT.,*Vol. 41, No. 3, pp. 462–471, March 1993.

[9] D.J. Hoppe, “Modal Analysis Applied to Circular, Rectangular, and Coaxial Waveguides,” *TDA Progress Report, 42-95*, pp. 89–96, July 1988.

[10] J. D. Wade and R. H. MacPhie, “Scattering at Circular-to-Rectangular Waveguide Junctions,” *IEEE Trans. On MTT.,*Vol. 34, No. 11, pp. 1085–1091, Nov. 1986.

[11] R. Ihmels and F. Arndt, "Rigorous Modal S-Matrix Analysis of the Cross-Iris in Rectangular Waveguides," *IEEE Microwave and Guided Wave Letters,* Vol. 2, No. 10, pp. 400–402, Oct. 1992.

[12] S. H. Hajimowlana, et al., "Determination of Cut-off Wavelengths of Ridged Waveguides by Modal Analysis," *Proc. of the 40th Midwest Symp. on Circuits and Systems,* Vol. 1, pp. 642–645, Aug. 1997.

[13] F. Giese, *et al.*, "Modal Analysis of Arbitrarily Shaped Irises in Waveguides by Hybrid contour-integral mode-matching method," *IEEE MTT Symp. dig.,* pp. 1359–1362, 1995.

[14] J. Gil, et al., "Full-Wave Analysis and Design of Dielectric-Loaded Waveguide Filters Using a State-Space Integral-Equation Method," *IEEE Trans. On Microwave Theory and Tech.,*Vol. 57, No. 1, pp. 109–120, Jan. 2009.

[15] M. Yahia, et al., "Analysis of Complex Rectangular Waveguide Discontinuities Using Hybrid MVM-FEM," in *Asia Pacific Microwave Conf.*, pp. 111–114*,* Dec. 2009.

[16] P. Grassi, et al., "Analysis of Inhomogeneously Filled Waveguide Devices by a Hybrid Mode Matching-Finite Element Technique," *IEEE AP-S Int. Symp.,* Vol. 2, pp. 161–164, June 2003.

[17] M. Yahia, et al., "Complex 2D Discontinuities Analysis Using Hybrid Finite Element Method and a Modified Multimodal Variational Formulation-Application to Filter Design," *Proc. of the 40th European Microwave Confer*, pp. 1301–1304*,* 28 Sept. 2010.

[18] T. E. Rozzi, "The Variational Treatment of Thick Interacting Inductive Irises," *IEEE Trans. On Microwave Theory and Tech.,* Vol. 21, No. 2, pp. 82–88, Feb. 1973.

[19] A. Weisshaar, et al*.*, "CAD-Oriented Fullwave Equivalent Circuit Models for Waveguide Components and Circuits," *IEEE Trans. On Microwave Theory Tech.,* Vol. 44, No. 12, pp. 2564–2570, Dec. 1996.

[20] M. S. Navarro, et al., "Propagation in a Rectangular Waveguide Periodically Loaded with Resonant Irises," *IEEE Trans. On Microwave Theory Tech.,* Vol. 28, No. 8, pp. 857–865, Aug. 1980.

[21] J-W. Tao and H. Baudrand, "Multimodal Variational Analysis of Uniaxial Waveguide Discontinuities," *IEEE Trans. On Microwave Theory Tech.,*Vol. 39, No. 3, pp. 506–516, March 1991.

[22] M. H. Engineer and B. R. Nag, “Propagation of Electromagnetic Waves in Rectangular Guides Filled with a Semiconductor in the Presence of a Transverse Magnetic Field,” *IEEE Trans. On Microwave Theory Tech,* Vol. 13, No. 5, pp. 641–646, Sept. 1965.

[23] J. B. Davies, “Propagation in Rectangular Waveguide Filled with Skew Uniaxial Dielectric,” *IEEE Trans. On Microwave Theory Tech.,* Vol. 15, No. 6, pp. 372–376, June 1967.

[24] S. Liu, *et al.*, “Rectangular Conducting Waveguide Filled with Uniaxial Anisotropic Media: A Modal Analysis and Dyadic Green’s Function,” *PIER,* Vol. 25, pp. 111–129, 2000.

[25] C. L. D. S. S. Sobrinho and A. J. Giarolas, “Analysis of the Optical Axis Misalignment Effect on Propagation Characteristics of Anisotropic Dielectric Waveguides Using FD-FD Method,” *AP-S Inter. Symp.,* Vol. 2, pp. 980–983, July 1996.

[26] N. J. Damaskos, *et al.*, “The Inverse Problem for Biaxial Materials,” *IEEE Trans. Microwave Theory Tech.,* Vol. 32, No. 4, pp. 400–405, April 1984.

[27] J. Sheen, “Time Harmonic Electromagnetic Fields in an Biaxial Anisotropic Medium,” *Journ. Of Electro. Waves and Appl.,* Vol. 19, No. 6, pp. 753–767, 2005.

[28] H. C. Chen, *Theory of Electromagnetic Waves: A Coordinate-free Approach*, McGraw-Hill Inc., 1983, pp. 181–218.

[29] D. M. Pozar, “Radiation and Scattering from a Microstrip Patch on a Uniaxial Substrate,” *IEEE Trans. Antennas Propag.,* Vol. 35, No. 6, pp. 613–621, June 1987.

[30] C. Krowne, “Spectral-domain determination of the propagation constant in biaxial planar media,” *Inter. Jour. of Elec.,* Vol. 59. No. 3, pp. 315–332, Feb. 1985.

[31] A. B. Yakovlev and G. W. Hanson, “Fundamental Modal Phenomena on Isotropic and Anisotropic Planar Slab Dielectric Waveguides,” *IEEE Trans. On Antenna and Prop.,* Vol. 51, No. 4, pp. 888–897, April 2003.

[32] A.M. Jalaleddine, “Guided Waves Propagating in Isotropic and Uniaxial Anisotropic Slab Waveguides,” Masters Thesis, College of Eng. And Tech., Ohio University, Athens, Ohio, 1982.

[33] Y-C Shih, “Design of Waveguide E-Plane Filters with All-Metal Inserts,” *IEEE Trans. On Microwave Theory Tech.,* Vol. 32, No. 7, pp. 695–704, July 1984.

[34] Z. Shen and R. H. MacPhie, “An Improved Modal Expansion Method for Two Cascaded Junctions and Its Application to Waveguide Filters,” *IEEE Trans. On Microwave Theory Tech.,*Vol. 43, No. 12, pp. 2719–2722, Dec. 1995.

[35] F. Arndt, et al., “Modal S-matrix Method for the Optimum Design of Inductively Direct-Coupled Cavity Filters,” *IEE Proceedings,* H, Vol. 133, No. 5, pp. 341–350, Oct. 1986.

[36] R. Thabet and M. L. Riabi, “Full-Wave Analysis of Filters in Metallic Waveguides using the Mode-Matching Method and the Genetic Algorithm,” *IEEE Interna. Conf. on Comp. Cybernetics,* pp. 215–219, Oct. 2007, Gammarth, Tunisia.

[37] D. M. Pozar, *Microwave Engineering 3rd ed.*, John Wiley and Sons, Inc., 2005. pp. 92–115.

[38] R. E. Collin, *Foundations for Microwave Engineering 2rd ed.*, John Wiley and Sons, Inc., 2001.

[39] J. A. Kong, *Electromagnetic Wave Theory*, EMW Publishing, 2008.

[40]R. F. Harrington, *Time-Harmonic Electromagnetic Fields*, John Wiley and Sons, Inc., 2001.

[41] P. M. Morse and H. Feshbach, *Methods of Theoretical Physics*, New York: McGraw-Hill, 1953, pp. 718-727.

[42] Y.C. Shih and K.G. Gray, “Convergence of Numerical Solutions of Step-Type Waveguide Discontinuity Problems by Modal Analysis ,” *IEEE MTT-S Inter. Micro. Symp. Digest*, pp. 233–235*,* May 1983.

[43] N. Marcuvitz, *Waveguide handbook*, MIT Rad. Lab. Series, vol. 10, New York: McGraw-Hill. 1951.

[44] High Frequency Structure Simulator (HFSS), *Ansys Inc.*, Canonsburg, PA 15317.

[45] A. Eroglu, et al., “Dyadic Green’s Functions for Multi-layered Uniaxially Anisotropic Media with Arbitrarily Oriented Optic Axes,” *IET Microw. Antennas Propag.,* Vol. 5, No. 15, pp. 1779–1788, May 2011.

[46]R. Brannon, *ROTATION: A review of useful theorems involving proper orthogonal matrices referenced to three dimensional physical space*, Textbook Draft, Sandia National Laboratories, Albuquerque, NM, 2002, pp. 14–18.

[47]T.J. Cui, D. R. Smith, and R. Liu, *Metamaterials: Theory, Design, and Applications*, New York: Springer, 2010.

[48]N. Engheta and R. W. Ziolkowski, *Metamaterials: Physics and engineering and Explorations*, New Jersey: IEEE Press, 2006.

[49] Y. Dong and T. Itoh, “Promising Future of Metamaterials,” *IEEE Microwave Magazine,* Vol. 13, No. 2, pp. 39–56, March 2012.

[50] S. Hrabar, et al., “Waveguide Miniaturization Using Uniaxial Negative Permeability Metamaterial,” *IEEE Trans. On Anten. And Prop.,* Vol. 53, No. 1, pp. 110–119, Jan. 2005.

[51] F-Y. Meng, et al., “Controllable Metamaterial-Loaded Waveguides Supporting Backward and Forward Waves,” *IEEE Trans. On Anten. And Prop.,* Vol. 59, No. 9, pp. 3400–3411, Sept. 2011.

[52] F-Y. Meng, et al., “Backward and Forward Waves in a Uniaxial Anisotropic Metamaterial Waveguide,” in *Inter. Conf. on Microw. And Milli. Wave Tech.,* Vol. 1, pp. 54–57, April 2008.

[53] R. Marques, et al., “Left-Handed-Media Simulation and Transmission of EM Waves in Subwavelength Split-Ring-Resonator-Loaded Metallic Waveguides,” Physical Review Letters, Vol. 89, No. 18, pp. 1–4, Oct. 2002.

[54] R.A. Shelby, et al., “Microwave Transmission Through a Two-dimensional, isotropic, left-handed metamaterial,” *Appl. Phys. Lett.,* Vol. 78, No. 4, pp. 489–491, Jan. 2001.

[55] J.B. Pendry, et al., "Low Frequency Plasmons in Thin Wire Structures," *J. Phys.: Condens. Matter,* Vol. 10, No. 22, June 1998, pp. 14785–4809.

[56] S. Hrabar, et al., "Shrinking Dimensions of the Unit Cell of Thin-wire-based ENG Metamaterial by Inductive Loading," *IEEE Inter. Sym. Ant. and Prop.*, pp. 479–482*,* July 2006.

[57] S. Hrabar and G. Pavlakovic, "Numerical and Experimental Investigation of Inductively Loaded Thin-Wire-Based Metamaterial," *2nd Eurp. Conf. on Ant. and Prop.*, pp. 1–4*,* Nov. 2007.

[58] I. S. Nefedov and S. A. Tretyakov, "Electrically Controllable Metamaterials Based on Two-Dimensional Wire Media," *Eurp. Micro. Conf.,* Vol. 1, pp. 433–436, Oct. 2005.

[59] J-S Hong and M.J. Lancaster, *Microstrip Filters for RF/Microwave Applications*. 1st ed., New York, New York: John Wiley & Sons, Inc., pp. 40−130, 2001.

[60] X-C Zhang, et al., "Novel Band-Pass Substrate Integrated Waveguide (SIW) Filter based on Complementary Split Ring Resonators (CSRRS)," *PIER,* vol. 72, pp. 39−46, 2007.

[61] C. Liu and K. Huang. "A Compact Substrate Integrated Waveguide Band-pass Filter," *PIER Symp. Procee.,* Cambridge USA, pp. 1135−1138, July 2010.

[62] D. Zelenchuk and V. Fusco. "Low Insertion Loss Substrate Integrated Waveguide Quasi-Elliptic Filters for V-band Wireless Personal Area Network Applications," *IET Microw. Anten. & Prop.*, vol 5, no. 8, pp. 921−927, 2011.

[63] M. Bozzi, *et al.*, "Review of Substrate Integrated Waveguide Circuits and Antennas," *IET Micro. Anten. & Prop.* vol. 5, no. 8, pp. 909−920, 2011.

[64] W-Y. Park and S. Lim, "Miniaturized Substrate Integrated Waveguide (SIW) Bandpass Filter Loaded with Double-Sided-Complementary Split Ring Resonators (DS-CSRRs)," *Procee. of 41st European Microw. Confer.*, pp. 740−743, Oct. 2011.

[65] Z. Sotoodeh, et al., "A Novel Bandpass Waveguide Filter Structure on SIW Technology." *PIER,* vol. 2, pp. 141−148, 2008.

[66] Sonnet Software.

Appendix A

It will be shown that the wave admittance for all three cases of uniaxial media in Section 4.2 is $\beta/\omega\mu$ which is the wave admittance for isotropic media. Equation (4.56) is

$$-\alpha_{22}\frac{\partial^2}{\partial z^2}H_z - \alpha_{22}\frac{\partial^2}{\partial x^2}H_z = k_0^2 H_z \qquad \text{A.1}$$

where $k_0^2 = \omega^2\mu_0\varepsilon_0$. Assuming that H_z has $e^{-j\beta z}$ dependence, $\frac{\partial}{\partial z^2}H_z = -\beta^2 H_z$ and (A.1) becomes

$$-\frac{\partial^2}{\partial x^2}H_z = \left(\frac{k_0^2}{\alpha_{22}} - \beta^2\right)H_z. \qquad \text{A.2}$$

Taking α, β, and ψ for each of Case 1 in 4.2.1, Case 2 in 4.2.2, and Case 3 in 4.2.3 and substituting them into (4.35)–(4.40), we obtain

$$\bar{\bar{\varepsilon_r}} = \begin{bmatrix} \varepsilon_{11} = \varepsilon & 0 & 0 \\ 0 & \varepsilon_{22} = \varepsilon & 0 \\ 0 & 0 & \varepsilon_{33} = \varepsilon_z \end{bmatrix} \text{ for Case 1} \qquad \text{A.3}$$

$$\bar{\bar{\varepsilon_r}} = \begin{bmatrix} \varepsilon_{11} = \varepsilon & 0 & 0 \\ 0 & \varepsilon_{22} = \varepsilon_z & 0 \\ 0 & 0 & \varepsilon_{33} = \varepsilon \end{bmatrix} \text{ for Case 2} \qquad \text{A.4}$$

$$\bar{\bar{\varepsilon_r}} = \begin{bmatrix} \varepsilon_{11} = \varepsilon_z & 0 & 0 \\ 0 & \varepsilon_{22} = \varepsilon & 0 \\ 0 & 0 & \varepsilon_{33} = \varepsilon \end{bmatrix} \text{ for Case 3} \qquad \text{A.5}$$

Substituting (A.3)–(A.5) for $\bar{\bar{\varepsilon_r}}$ in

$$\bar{\bar{\alpha_r}} = (\bar{\bar{\varepsilon_r}})^{-1}, \qquad \text{A.6}$$

we obtain

$$\bar{\bar{\alpha_r}} = \begin{bmatrix} \alpha_{11} = 1/\varepsilon & 0 & 0 \\ 0 & \alpha_{22} = 1/\varepsilon & 0 \\ 0 & 0 & \alpha_{33} = 1/\varepsilon_z \end{bmatrix} \text{ for Case 1} \qquad \text{A.7}$$

$$\bar{\bar{\alpha_r}} = \begin{bmatrix} \alpha_{11} = 1/\varepsilon & 0 & 0 \\ 0 & \alpha_{22} = 1/\varepsilon_z & 0 \\ 0 & 0 & \alpha_{33} = 1/\varepsilon \end{bmatrix} \text{ for Case 2} \qquad \text{A.8}$$

$$\overline{\overline{\alpha_r}} = \begin{bmatrix} \alpha_{11} = 1/\varepsilon_z & 0 & 0 \\ 0 & \alpha_{22} = 1/\varepsilon & 0 \\ 0 & 0 & \alpha_{33} = 1/\varepsilon \end{bmatrix} \text{ for Case 3} \quad \text{A.9}$$

Extracting the values of α_{22} from (A.7)–(A.9), we have

$$\alpha_{22} = \frac{1}{\varepsilon_{22}} \quad \text{A.10}$$

where

$$\varepsilon_{22} = \begin{cases} \varepsilon, \text{Case 1} \\ \varepsilon_z, \text{Case 2} \\ \varepsilon, \text{Case 3} \end{cases} \quad \text{A.11}$$

Substitution of (A.10) into (A.2) gives

$$-\frac{\partial^2}{\partial x^2} H_z = (k_0^2 \varepsilon_{22} - \beta^2) H_z. \quad \text{A.12}$$

If $k_0^2 \varepsilon_{22} > \beta^2$, then the general solution of (A.12) for H_z is

$$H_z = A \cos(k_x x) + B \sin(k_x x) \quad \text{A.13}$$

where A and B are arbitrary complex constants and $k_x^2 = k_0^2 \varepsilon_{22} - \beta_0^2$.

Next, we will assume that $E_z = 0$ and proceed to express E_x, E_y, H_x, and H_y in terms of H_z.

The source-free Maxwell's equations subject to the constitutive relations are

$$\nabla \times \vec{E} = -j\omega\mu_0 \vec{H} \quad \text{A.14}$$

$$\nabla \times \vec{H} = -j\omega\varepsilon_0 \overline{\overline{\varepsilon_r}} \vec{E} \quad \text{A.15}$$

With $E_z = 0$ and with all field components having $e^{-j\beta z}$ dependence, (A.14) expands to

$$j\beta E_y = -j\omega\mu_0 H_x \quad \text{A.16}$$

$$-j\beta E_x = -j\omega\mu_0 H_y \quad \text{A.17}$$

$$\frac{\partial E_y}{\partial x} = -j\omega\mu_0 H_z \quad \text{A.18}$$

and (A.15) expands to

$$j\beta H_y = j\omega\varepsilon_o\varepsilon_{11}E_x \quad \text{A.19}$$

$$-j\beta H_x - \frac{\partial H_z}{\partial x} = j\omega\varepsilon_o\varepsilon_{22}E_y \quad \text{A.20}$$

$$\frac{\partial H_y}{\partial x} = j\omega\varepsilon_o\varepsilon_{33}E_z \quad \text{A.21}$$

Use of (A.16) and (A.20) gives

$$E_y = \frac{j\omega\,\mu_0\frac{\partial H_z}{\partial x}}{k_0^2\varepsilon_{22}-\beta^2} \quad \text{A.22}$$

$$H_x = \frac{-j\beta\frac{\partial H_z}{\partial x}}{k_0^2\varepsilon_{22}-\beta^2} \quad \text{A.23}$$

Use of (A.17) and (A.19) gives

$E_x = E_y = 0$. A.24

The characteristic admittance is Y_{in} defined by

$$Y_{in} = -\frac{H_x}{E_y}. \quad \text{A.25}$$

Substitution of (A.22) and (A.23) into (A.25) gives

$$Y_{in} = \frac{\beta}{\omega\mu}. \quad \text{A.26}$$

The boundary condition is

$E_y = 0$ at $x = 0$ and $x = a$. A.27

In view of (A.22), (A.27) requires that

$\frac{\partial H_z}{\partial x} = 0$ at $x = 0$ and at $x = a$. A.28

Equation (A.28) reduces (A.13) to

$$H_z = A\cos(k_x x) \quad \text{A.29}$$

where

$k_x = m\pi/a$, m = 1,2,… A.30

Luke E. Murphy_____
Email Lemurphy@syr.edu

Education:

Doctor of Philosophy Electrical Engineering, December 2013
Syracuse University

Masters of Science Electrical Engineering, May 2009
Syracuse University

Certificate of Advanced Study in Microwave Engineering, May 2009
Syracuse University

Bachelor of Science Electrical Engineering, May 2007, Dean's List
Rensselaer Polytechnic Institute

United States Military Academy, West Point, 2003-2004

Fellowships and Awards:

Young Engineering Award, ARMMS Conference 2012
Awarded to top 2 student papers; covers conference fees
Gerst-Hair Graduate Fellowship (2007-2009)
Awarded to Syracuse University ECS graduate student; provides tuition and monthly stipend

Work Experience:

Dielectric Laboratories Inc, (Spring 210 – Present)
Work directly with customers in the design of custom microstrip filters and dielectric waveguide filters; Research and Development in new products and technology for the advancement of the company and product lines; Project Manager for companywide yield improvement and analysis.

Anaren Inc, (Summer 2008 – Spring 2010)
Work 20 hours per week; design and test engineer for 900MHz and 1900MHz LNA;
lead design engineer for 900MHz 2:1 Balun; design Engineer for Xinger 5dB and 30dB line couplers;
process daily data vital for project completion.

Anaren Inc, (Summer 2007)
Preformed various S-parameter measurements and tests on Epsilon project; temperature tested S-parameters; tuned failing devices

General Electric, Global Research Center (Summer 2006)
Configured and tested RF modules and gain antennas; developed models in Matlab and Simulink; configured and interfaced various electronic measurement devices. Internship culminated with a trip to Kansas City, MO for field testing.

Publications:

M. Yazdani, L. Murphy, A. Mallahzadeh, E. Arvas, and J. Mautz. "The design of double ridge waveguide filter using conventional stepped impedance low-pass filter method." *Microwave and Optical Technology Letters*. Vol. 56, No. 1, Jan. 2014, pp. 120-124.
L. Murphy, M. Yazdani, J. Mautz, E. Arvas, and S. Tozin. "Design of a Dielectric Waveguide Filter with Embedded Metamaterial using Mode Matching Technique." *Microwave and Optical Technology Letters*. Accepted October 2012

L. Murphy, M. Yazdani, and E. Arvas. "Compact Low Pass Filter with Ultra-Wide Pass and Stopbands using Stepped Impedance Resonators and Novel Techniques." *ARMMS Conference*, Bedfordshire UK, November 2012.
L. Murphy, M. Yazdani, and E. Arvas. "Ultra-wide stopband in a Compact Low Pass Filter using Stepped Imedance Resonators and Novel Techniques." *IEEE Confr. on UWB*, Syracuse NY, pp. 92-94, 2012.
L. Murphy, H. Partal, C-M. H, G. Alton, E. Arvas, and S. Arvas. "Project based microwave filter design course," Proceedings of the 26th Annual Review of Progress in Applied Computational Electromagnetics (ACES 2010), Tampere, Finland, April 25-29, 2012
L. Murphy, C-M. H, G. Alton, S. H. Partal. "Low loss suspended substrate 8GHz bandpass filter with high selectivity," (Abstract) IEEE Workshop on Mircrowave Passive Circuits and Filters," Syracuse, NY, April 20, 2010.
C-M. H, L. Murphy, T. Chin, and E. Arvas. "Vivaldi Antenna for GPR," ACES Conference, Monterey CA, 2009.

Graduate Projects and Research:

Designed microstrip Vivaldi antenna for use in breast cancer detection with coplanar input feed for improved input return loss
Designed planar antipodal Vivaldi antenna for ground penetrating radar (GPR) applications
Using wavelet analysis and matched filter approach designed detection algorithm to identify desired signal
Designed low-noise microwave amplifier for wireless internet application

Undergraduate Research:

(2006-2007) Under Professor George Nagy
Participated in Table Analysis for Generating Ontologies or TANGO. This is an information-gathering engine that will assimilate and organize information, more specifically, identical information found in differently formatted tables on the internet. My role in the project was to develop a program in Matlab. Upon completion of this program it was interfaced with a Wang notation generating program created by a graduate student; and finally the two programs were tested on random test subjects. The Matlab program created a log file which recorded the time a user enters various inputs in the program. It also recorded what time command prompts were presented to the user and how long it
took the user to respond. The log file information was then used to determine efficiency and bottleneck areas in the generation of Wang notation and standardized tables.

(2005-2006) Under Professor Kenneth Connor and Paul Schoch
Worked with the Plasma Group at RPI. My role in this project, which had two major areas, was to help control high energy ion beams. The first goal was to design a function generator used as an arbitrary function to drive high voltage op-amps. The op-amps, working at up to 20kV were used to electrostatically steer the ion beams. This function was necessary because of the slow slew rate of high voltage op-amps and the small time scale of the experiment in which the ion beam will be used. The second part of the project was to develop an interface to control voltages on two separate ion beam focusing elements via an RF signal. This method was necessary to prevent the controlling computer from being attached to the 150kV gun. Both of these sub projects will be implemented using the Silicon Laboratories C8051 microcontroller board and appropriate external components.

Software and Skills:

Matlab, Ansoft, HFSS, Sonnet, AWR, and Genesys
Use of network analyzer, spectrum analyzer, and various analysis instrumentation

Mastery of computer aided design
Computer programming ability in C++, C, and Java
Understanding of HTML web design
Moderate Spanish speaking and conversational knowledge

Activities:

Captain, Varsity Lacrosse Team, Rensselaer Polytechnic Institute
Captain, Club Lacrosse Team, Syracuse University
Certified Section III Lacrosse Referee
Volunteered for local soup kitchen, St. Josephs Church, Syracuse
Volunteered for church nursery, St. Josephs Church, Syracuse NY
Hobbies include fly-fishing, cooking, half marathons and golf